Fluid Structure Interaction Modeling of Pulsatile Blood Flow in Serial Pulmonary Artery Stenoses

Say Yenh Hong, McGill University, Montreal

August, 2007

Department of Mechanical Engineering

A thesis submitted to McGill University in partial fulfillment of the requirements of the degree of Masters of Engineering

Your file Votre référence
ISBN: 978-0-494-51461-0
Our file Notre référence
ISBN: 978-0-494-51461-0

To my parents

Abstract

Motivated by the physiological phenomena of collapse and flow limitation for a serial pulmonary artery stenosis, we investigated the three-dimensional influence of spatial configuration on the wall motion and hemodynamic. Our numerical study focused on the effect of two geometrical parameters: the relative distance and the angular orientation between the two stenoses. The collapse of a compliant arterial stenosis may cause flow choking, which would limit the flow reserve to major vital vascular beds such as the lungs, potentially leading to a lethal ventilation-perfusion mismatch. Flow through a stenotic vessel is known to produce flow separation downstream of the throat. The eccentricity of a stenosis leads to asymmetric flow where the high velocity jets impinge on the sidewall, thereby inducing significant dissipation. The additional viscous dissipation causes a higher pressure drop for a flow through a stenotic vessel, than in a straight compliant vessel. It is likely that some particular morphology would have a higher vulnerability to the fluid induced instability of buckling (divergence), under physiological pulsatile flow. It was found that fluid pressure distribution have substantial implication for the downstream wall motion, under conditions of strong coupling between nonlinear vessel geometries, and their corresponding asymmetric flow. The three-dimensional fluid structure interaction problem is solved numerically by a finite element method based on the Arbitrary Lagrangian Eulerian formulation, a natural approach to deal with the moving interface between the flow and vessel. The findings of this investigation reveal that the closeness between stenoses is a substantial indication of wall collapse at the downstream end. Moreover, the results suggest a close link between the initial angular orientation of the distal stenosis (i.e. the constriction direction) and the subsequent wall motion at the downstream end. For cases showing evidence of preferential direction of wall motion, it was found that the constricted side underwent greater cumulative displacement than the straight side, suggestive of significant wall collapse.

Résumé

Motivé par les phénomènes physiologiques de collabage des vaisseaux sanguins et de l'arrêt de l'écoulement sanguin pour des sténoses artérielles pulmonaire en série, nous en étudions l'influence de la configuration spatiale tridimensionnelle sur les mouvements des parois du vaisseau sanguin et l'hémodynamique. Notre étude se concentre sur l'effet de deux paramètres géométriques: la distance et l'orientation angulaire relative entre les deux sténoses. L'effondrement d'une sténose artérielle pulmonaire peut provoquer l'arrêt de l'écoulement, menant à une limitation du flux de réserve aux lits vasculaires vitaux tels que les poumons, causant ainsi un problème de ventilation et de perfusion, ceci étant potentiellement mortel. Il est connu que l'écoulement à travers un vaisseau atteint par une sténose produit une séparation d'écoulement en aval du rétrécissement. L'excentricité d'une sténose cause un écoulement de nature asymétrique, où des jets de haute vélocité peuvent impacter sur la paroi du vaisseau sanguin, provocant ainsi des dissipations importantes. Ces dissipations visqueuses supplémentaires provoquent une chute de pression plus élevé pour un écoulement à travers une sténose artérielle pulmonaire, comparé à un vaisseau droit. Il est probable que certaines morphologies possèderaient un potentiel plus élevé à l'effondrement des vaisseaux sanguins, sous un écoulement pulsatile physiologique. Il a été constaté que les distributions de pressions du fluide ont une influence particulière sur les mouvements des parois du vaisseau sanguin situés en aval, spécialement lorsque le couplage entre les géométries non linéaires des vaisseaux et leurs écoulements de nature asymétrique correspondant est considéré. Le problème d'interaction entre le fluide et la structure tridimensionnelle est numériquement résolu par une méthode d'éléments finis basée sur la formulation "*Arbitrary Lagrangian Eulerian*", une approche naturelle pour traiter le mouvement de l'interface entre l'écoulement et le vaisseau. Les conclusions de cette étude révèlent que la proximité entre les sténoses est une cause importante d'effondrement des parois du vaisseau sanguin situé en aval. Les résultats suggèrent aussi un rapport entre l'orientation angulaire initiale de la sténose en aval (c'est-à-dire dans la direction du rétrécissement) et les mouvements des parois du vaisseau sanguin.

Contents

List of Figures

List of Symbols

Latin Symbols

E	Internal energy per initial volume
G	Elastic shear modulus
K	Bulk modulus
M	Mass matrix
S_{ij}	Deviatoric Cauchy stress tensor
V	Relative volume
b_i	Body force per unit mass
c_e	Current wave speed in element e
c_i	Convective velocity
d	Nodal displacement
e	Internal energy per unit mass
f^{int}	Internal nodal force
f^{ext}	External nodal force
l_e	Characteristic length of element e
p	Pressure
v_i	Velocity of a material particle

Greek Symbols

Ω_F	Spatial domain where the fluid motion is described
Ω_S	Lagrangian description of the domain where the structural motion is described
Γ_{FS}	Moving interface between Ω_F and Ω_S
Γ_1	Inlet surface boundary
Γ_2	Outlet surface boundary
a	Courant number
δ_{ij}	Kronecker delta
μ	Dynamic viscosity
ρ	Fluid density
σ_{ij}	Cauchy stress tensor

Chapter 1.

Clinical Perspective

In this chapter, we introduce the clinical backdrop where the fluid structure interaction involving a pulsatile blood flow with its surrounding vessel takes place for each heart beat. The journey begins by portraying the physiological and anatomical features of the pulmonary circulation, followed by stressing the role played by the pulmonary vessel in the cardiac cycle. In the next section, we describe the pathology of pulmonary artery stenosis and several related inborn defects. We proceed with a discourse on the clinical success and peril associated with percutaneous stenting as a possible surgical intervention. A non-exhaustive literature review on fluid structure interaction of arterial stenosis and collapsible tubes ensues. This course naturally steers us to the formalization of the thesis objectives.

1.1 Physiology of the Pulmonary Artery

1.1.1 The Pulmonary Circulation

The pulmonary artery is an essential component of the pulmonary circulation. In this low pressure system (*8 -25 mm Hg*), the pulmonary circulation system carries blood from the right ventricle to the left atrium of the heart. Blood flows from the right ventricle to the pulmonary arterial trunk which is divided into the main right and left pulmonary artery, entering the lungs, with further ramifications into smaller branches akin to a tree, the lung finally terminating in the capillary sheets [1] (*Figure 1.1*). In these reside air sacs called pulmonary alveoli, where blood acquires oxygen and releases carbon dioxide. Then the blood flows from the capillary sheets into a venous tree, terminating in the left atrium of the heart. It is worthwhile to mention that the pulmonary circulation is able to convey an equivalent amount of flow with respect to its systemic arterial counterpart (*80-120 mm Hg*), at substantially lower levels of pressure (i.e. mean arterial pressure is about one-sixth of systemic) [2, 3]. The pulsatile nature of ventricular ejection and the homeostatic

requirement for an equivalent amount of blood ejected per beat from each ventricle, place unique constraints upon the right ventricle and the opposition to forward flow in the pulmonary artery [2]. Namely, the steady resistive term of its opposition to flow is significantly lower than the systemic vascular resistance, at about one-sixth of the latter [3]. In addition, vascular distensibility is greater in the pulmonary circulation. Thus, the flow wave in the main pulmonary artery is usually of lower amplitude with a longer duration of forward flow when compared to the ascending aorta flow wave. Furthermore, both pressure and flow wave are more rounded due to the minimal effect of wave reflection. The pressure-flow relations of the pulmonary circulation are important for the understanding of lung and heart diseases, such as pulmonary hypertension, cardiac hypertension, tissue hypertrophy, edema, and various respiratory disorders and diabetes [1]. However, the study of the pressure-flow relations is complicated by the location of the right main pulmonary artery, extending beyond the hilum of the lung. This causes difficulties for conducting in vivo measurements or surgical corrections [4]. In order to circumvent these hurdles, one may rely on the principles of continuum mechanics. The continuum approach is especially suitable to the study of pulmonary blood flow, given that the basic laws of conservation of mass, momentum and energy will shed a new light on the pressure-flow relationships in the context of a pulmonary artery stenosis.

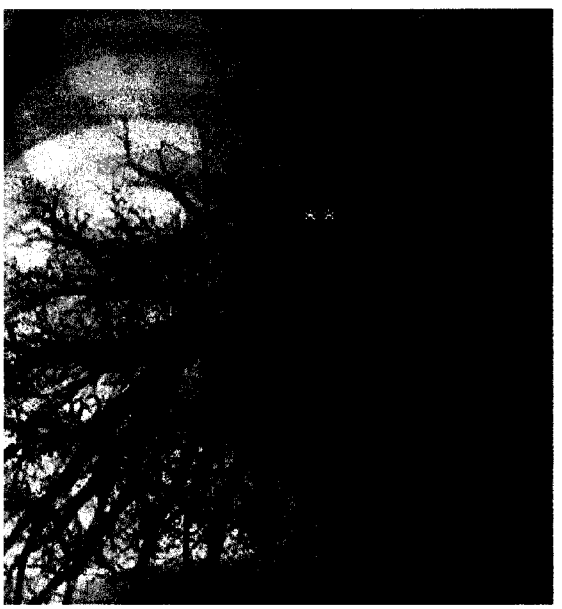

Figure 1.1 Right pulmonary artery angiogram, from [5].

1.1.2 Distensibility of Pulmonary Blood Vessel

Vascular elasticity, or distensibility, is a mechanical property of blood vessel which determines the changes in the diameter of blood vessel as a result of changes in blood pressure [1]. The distensibility of pulmonary blood vessel directly influences the distribution of pulmonary blood pressure, regional distribution of pulmonary blood volume, transit time distribution of blood in the lung, and pulse wave attenuation through the lung. A distinctive characteristic of the pulmonary artery is the degree of extensions induced by blood pressure. It averages *8%* in the pulmonary artery, whereas in the other artery it is typically on the order of *1-2%*. Changes in diameter during the cardiac cycle usually reach *10-15%* in the pulmonary artery, *6-10%* in the carotids, and *2-5%* in the aorta [6]. The inherent distensibility of the pulmonary artery versus other artery manifests itself in the following clinical observations: pulmonary hypertension is considered severe for a 400 percent increase in mean pressure, whereas for systemic hypertension, the threshold is 25 percent increase in mean pressure [3]. Thus, prudence is required for the interpretation of data obtained from the pulmonary circulation, especially for the purpose of clinical intervention decision.

Larger vessels located close to the heart, such as the pulmonary artery, are classified as elastic artery. It is worthwhile to mention that the pulmonary artery is the only artery in the circulatory system conveying deoxygenated blood. The remarkable distensibility of the pulmonary artery is dependent on its composition, structure and microstructure. The elastic pulmonary artery show a specific concentric pattern of elastic fiber and smooth muscle cell that predominate in the media, which may account for 10 percent of the external diameter of the vessel in a healthy person [7]. The adventitia makes up approximately 10 percent of the wall thickness in an elastic artery [8]. The collagen fibers in the adventitia are longitudinally oriented. These two layers provide the arterial wall the structural support to prevent over dilatation under physiologic loads. The compliance or elasticity of an artery is central to its functionality as a local blood pressure reservoir. It is vital since the heart ejects blood for one-third of the cardiac cycle, while the artery supply

blood for the remaining two-thirds of the cycle via energy stored in their stretched walls [9].

1.2 Pulmonary Artery Stenosis

Pulmonary Artery Stenosis is a congenital heart defect, generally occurring in conjunction with other inborn defects such as:

- Tetralogy of Fallot – a congenital heart anomaly which consists of pulmonary stenosis, ventricular septal defect (i.e. abnormal opening in the ventricular septum, whereby high pressure blood from the left ventricle flows through the defect into the right ventricle), dextroposition of the aorta (i.e. aorta on the right side instead of the left) and hypertrophy (i.e. enlargement or overgrowth) of the right ventricle. This condition results in a blue baby at birth due to inadequate oxygenation. Surgical correction is emergent [10].
- Pulmonary Atresia – a congenital absence of the normal valvular orifice into the pulmonary artery. This condition is characterized by cardiomegaly (i.e. enlargement of the heart), reduced pulmonary vascularity, and right ventricular atrophy (i.e. a size diminution) [10].
- Truncus Arteriosus – the formation of only one combined artery instead of the normal two outlets (i.e. aorta and main pulmonary artery) from the heart [11].
- Patent Ductus Arteriosus – a condition where the normal channel between the pulmonary artery and the aorta fails to close at birth. In normal fetal circulation, the blood bypasses the pulmonary circuit since oxygen and nutriments are acquired through the placenta. After birth, this channel normally closes in response to ventilation of the lungs. Those who are affected may demonstrate poor growth, shortness of breath and rapid respiratory rate [10].

Pulmonary Artery Stenosis may occasionally arise after placement of systemic to pulmonary shunts (i.e. a surgically created bypass) [12] or after the arterial switch operation (i.e. a complete transposition of the aorta and pulmonary artery) [13, 14]. For patients with congenital or post-operative pulmonary artery stenoses, the elevated right ventricular pressure is associated with right ventricle failure, arrhythmias (i.e. abnormal heart rhythms) and sudden death [15-17]. Within the venous system, significant stenoses, including cavopulmonary anastomoses (i.e. a surgically created shunt between the right pulmonary artery and the superior vena cava, which is the major venous channel draining the thorax and head, ending in the right atrium [10]), can contribute to superior vena cava syndrome (i.e. a narrowing or obstruction of this channel), poor passive flow with poor cardiac output and atrial arrhythmias. Elevated central venous pressures in these patients are a risk factor associated with higher mortality [17, 18].

1.2.1 Percutaneous Stenting of a Pulmonary Artery Stenosis

The term stent, considered as having been defined in dental reconstruction practice at the start of the 20th century, now commonly denotes a short metal or plastic filamentous tube that is inserted into the lumen of a vessel, especially to keep a formerly blocked passage open [19, 20]. More specifically, its main function is to provide radial support to the vascular wall to maintain luminal patency under various conditions [20]. In addition to mechanical support, novel delivery systems are built around the stent technology, which serves as a platform for local drug or gene therapy delivery. Stents can be delivered to distal branches not accessible surgically or within previously scarred areas of stenosis "from the inside", obviating the need for repeat operations and their associated complications [17]. The technique for stent delivery and implantation has been extensively described previously and can be found in [21-25]. Briefly, balloon-expandable metal stents are mounted on low pressure angioplasty balloons sized not to exceed the diameter of the vessel adjacent to the stenosis [20]. A thin flexible guide wire is used as a rail to direct a balloon-tipped catheter to the vessel target site with the aid of fluoroscopic imaging (e.g. via the femoral route for a pulmonary artery stenosis [26]). Once straddled over the obstruction site, inflation of the balloon results in the expansion

of the stent, usually in a single deployment maneuver. The expanded stent dimensions depend on the balloon characteristics and applied pressure, usually inflated to *8-12 atm* depending on the waist of the stent, although occasionally pressures as high as *17 atm* may be required to achieve full stent expansion [20, 27]. The balloon is then deflated and withdrawn so that blood can once again flow freely through the expanded and stented vessel. Self-expanding metal stents employ shape memory alloy, which allows expansion upon mild temperature change (i.e. cold and hot saline techniques) or release from a compressing sheath. Whether balloon-expandable or self-expandable shape memory alloy, bare metal or polymer coated, stents are available in a variety of designs (e.g. slotted tubular, helical coil, staggered backbone), lengths and diameters to accommodate differing applications and anatomies.

The first documented use of balloon-expandable intra-vascular stents in pulmonary artery and systemic vein in the late 1980s is attributed to Mullins et al [22]. The results from the FDA clinical trial data during the early 1990s indicate that intra-vascular stents are an effective and safe therapy for the treatment of vascular stenosis in patients with congenital heart disease [23-25, 28-30]. Medium and longer term follow-up studies have reinforced the findings from previous clinical studies [17, 21, 31-33]. As a result, endovascular stents are now commonly implanted in the pulmonary circulation to treat pulmonary arterial stenoses with generally excellent results. However, there are a number of potential complications associated with their use, namely restenosis (i.e. decreased vessel patency from reduction in lumen size), thrombosis, neointimal proliferation, vascular injury inflicted during deployment, patient size (age and weight) limitation, and mortality risks.

1.2.2 Complications Associated with Percutaneous Stenting

Restenosis after stent implantation is a potential clinical problem for some patients. In-stent restenosis has histological properties that may relate to a local tissue reaction on the presence of foreign material [20]. Uncoated metal stents are known to initiate an inflammatory process and a neointimal proliferation. The initial biological response is thrombus formation on the stent surface which peaks within the first week post-implantation [34]. The thrombus is then gradually replaced with a fibrous structure. The inflammatory response begins within a few days post-implantation and may last more than a month. This stage is characterized by large leukocyte and platelet deposition to the luminal aspect of the stent. Growth and proliferation of vascular smooth muscle cell into the media and neointima occur in conjunction with the inflammatory response, possibly lasting more than a month. Both the inflammation and proliferation phases peak near the first week as the neointima becomes well established with abundant macrophage and spindle cell [35]. In a follow-up study of 4500 patients whose coronary stent implantations were initially successful, binary restenosis (i.e. more than 50 percent reduction in diameter at 6 months as determined by angiography) was shown to vary from 20 percent in some stents to over 40 percent in others [36]. One to two millimeters of neointimal growth is a very significant problem in stented coronary artery given their small size (*Figure 1.2*), but it is not usually considered an important factor for the much larger pulmonary artery. A study of 200 patients reveals only three cases (1.5%) with significant stenosis due to neointimal proliferation caused by pulmonary artery stenting [17].

Irrespective of anatomical location, the induced perturbations in intra-stent flows are known to consist of low shear rate in the recirculation zones [37]. Regions of local intra vascular (arterial or venous) or intra cardiac flow separation and stasis are pro-thrombotic [38-45]. Early thrombus may serve as a scaffold for subsequent cell proliferation and intimal hyperplasia [46-48]. In the low wall shear stress regions exposed to flow reversal, endothelial cell modulate gene expressions, resulting in random cell structures, a decrease of nitric oxide (NO) production, an increase of monocyte adhesion and migration, and an

increase of permeability to macromolecules [49-56]. The prolonged residence time in the recirculation area allows for an increase of interaction between the cellular components and the vessel wall, specifically at the end of the diastole cycle [53]. Low wall shear stress regions have been shown to correlate with the built-up of endothelial cell mediated neointimal proliferation on the inner wall of the vascular system [57-62].

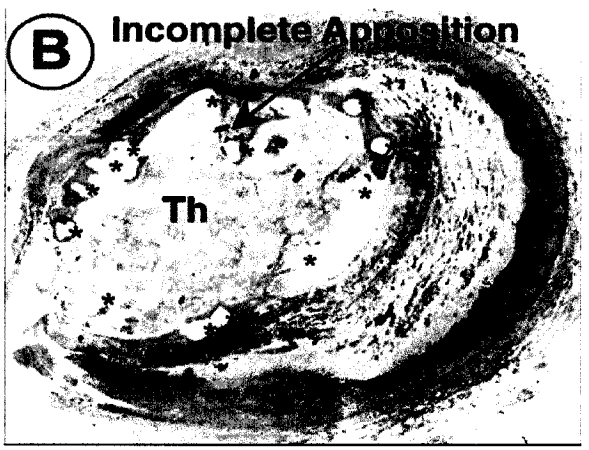

Figure 1.2 Total lumen occlusion by platelet-rich thrombus (Th), from [63].

From a structural standpoint, the vascular injury inflicted during the deployment phase of stent placement is a critical determinant of the biological events that ensue. Stent deployment causes partial denudation of the endothelium in a pattern unique to each stent configuration, suggesting balloon related injury [64]. In addition to the deep vascular trauma imposed by stent struts [65, 66], inter strut injury occurs during stent expansion from balloon artery interaction. While denudation of endothelial cell alone produces mild neointimal thickening [67], more substantial neointimal hyperplasia requires direct injury to medial smooth muscle cell underlying the endothelial cell [68, 69]. In stented artery, a correlation exists between the depth of arterial injury and the extent of intimal thickening [65, 66, 70]. Current clinical stent deployment techniques include balloon pre-dilatation, stent expansion at moderate balloon pressures, and post-dilatation at significantly higher balloon pressure to ensure that all stent struts are fully expanded and abutting the arterial wall [71]. The associated post-dilatation high pressures may be correlated with greater restenosis [72]. Higher inflation pressures and larger balloon sizes may also cause greater neointimal hyperplasia [72-75]. Hence, choosing the most suitable stent and treatment

procedure for a given stenosis is always a trade-off between lumen gain and locally induced arterial injury [76].

Furthermore, a relative patient size (age and weight) limitation exists for pediatric deployments, because the sizes of pulmonary artery and systemic vein increase as the patient grows. The use of stents may hinder further developments of the pulmonary artery [77]. Thus, a smaller stent, limited to 8-10 *mm* maximal diameter, is usually avoided in proximal or central vessels in infants or small children, since it would create a fixed non-dilatable stenosis that would require surgical opening or removal as the patient grows [17].

Lastly, stent implantation as an alternative to balloon angioplasty does not eliminate the possibility of mortality. The risk of death directly attributed to the stent procedure has been documented. In one patient with unusual familial congenital pulmonary artery branch stenosis and supra-systemic (i.e. higher than usual) pulmonary pressure, dilatation and stent implantation into two small distal pulmonary segments were successful. After the procedure, the increase in flow to the stented lung segments became so great that severe segmental pulmonary edema (i.e. abnormal accumulation of excessive fluid in the intercellular tissue spaces [10]) developed with a progressive and lethal ventilation-perfusion mismatch [17]. The second death was in a small child seven weeks post-Tetralogy of Fallot repair with severe residual bilateral branch pulmonary artery stenosis. He had intractable right heart failure and was not considered a candidate for re-operation. During stent dilatation, there was a main pulmonary artery tear resulting in a massive hemothorax (i.e. an effusion of blood into the cavity of the pleura, the serous membranes covering the lungs [10]), resulting in death [17]. Mortality related to rupture of the pulmonary artery proximal to the stent site was reported in [24, 25, 27]. It is plausible that such a rupture is caused by the elevation in pulmonary artery pressure due to relief of the stenosis, which was further elevated by coughing.

Currently, surgical intervention decisions for the stenting procedure are based on several ratios used in the clinical setting to assess stenosis severity:

Percent Area Occlusion

$$(1 - A_s / A_0) \times 100\% \tag{1.1}$$

where A_0 and A_s denote the lumen areas in the straight and at the throat section respectively.

Nominal Eccentricity of the Stenosis

$$Ecc = \frac{e}{(D - D_s)/2} \times 100\% \tag{1.2}$$

where D and D_s denote the lumen diameters in the straight and at the throat section respectively, and e is the distance between the centroid of the two areas. Real stenoses are normally eccentric.

Flow Reserve, *FR*, is defined as the ratio of flow during maximal vasodilatation to flow during control; this ratio is lowered with a stenosis present than in the normal bed.

$$FR = Q_{\max} / Q_c \tag{1.3}$$

Fractional Flow Reserve, *FFR*, is the ratio of the maximal flow with the stenosis present to the maximal flow in the unaffected bed.

$$FFR = Q_{\max, s} / Q_{\max, n} \tag{1.4}$$

In addition to the above-mentioned ratios, several clinical indications for stent implantation include right ventricular pressure above 60 percent of systemic level; angiographic appearance of significant narrowing in one or both branches, usually

associated with reduced pulmonary blood flow to the involved lung on nuclear lung perfusion scan; or a combination of the above [27]. For the purpose of follow-up, success of the procedure may be judged by one of the following criteria established by Rothman et al. [78]:

- >50% increase in stented vessel diameter
- >20% increase in flow to the lung by lung perfusion scan
- >20% reduction in the ratio of right ventricular to systemic pressure
- >50% reduction in the systolic gradient across the stented vessel

Fulfillment of any of the above criteria is usually adequate for the procedure to be judged successful (*Figure 1.3*).

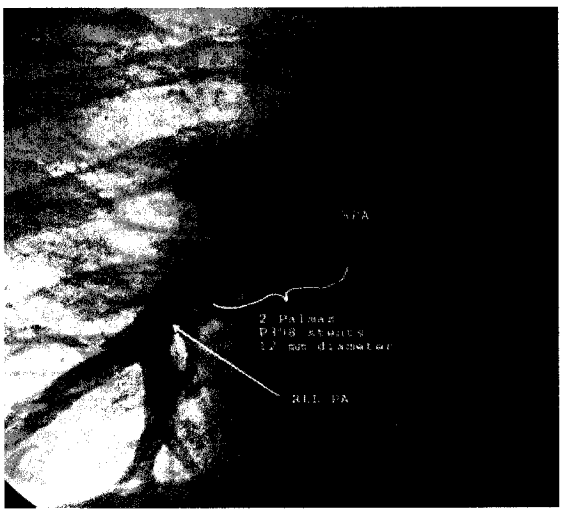

Figure 1.3 Percutaneous stenting of right pulmonary artery stenosis, from [4].

1.3 Fluid Structure Interaction of Arterial Stenosis

Stenosis is derived from the Greek term for 'narrowing'. In medical terminology, arterial stenosis refers to a localized narrowing or constriction in the arterial lumen [79] (*Figure 1.4*). A stenosis may be initiated by an event such as vessel damage, or by a dysfunctional endothelium. Its development consists of three stages: the intimal thickening, the growth stage, and the final stage when the severity affects blood supply [80]. Late phase flow limitation is characterized by losses produced by flow separation and turbulence downstream of the stenosis [81], which provide a favorable environment for platelet aggregation, thrombus formation, cell adhesion, and for prolonging cell residence time [82-84]. There has been increasing evidence that hemodynamic is closely related to intimal thickening [85], thrombus development [82, 86], and the adhesion, elongation and adaptation of cell [87, 88]. Blood pressure and wall shear stress have considerable effects on artery remodeling [89-92]. High wall shear stress may damage normal endothelium [93], and it may also activate platelet and cause platelet aggregation and thrombus formation [94]. The combination of a stenosis with flow pulsatility can result in periodic generation of turbulence, despite the relatively low Reynolds numbers of such flows [95]. Turbulence is normally observed when stenosis severity by area exceeds 80 percent [96], but has been noticed for a 40 percent stenosis with irregular geometry [97].

The fact that the vessels possess compliant wall affects flow stability and the generation of turbulence. Almost all vessels carrying fluids within the body are flexible, and interaction between an internal flow and the wall deformation often underlie a vessel's biological function or dysfunction [98]. The cardiovascular system provides abundant examples of sites where the fluid structure interaction are of major biological importance. Most obviously, pulse propagation in artery is fundamental for transporting blood from heart to tissues and organs throughout the body. Artery in the pulmonary circulation operate under lower transmural (i.e. internal minus external) pressure so that hydrostatic pressure variations can be sufficient to induce collapse (i.e. a significant reduction in cross-sectional area, but without complete occlusion), which can limit the flow of blood returning to the heart or passing through major organs such as the lungs.

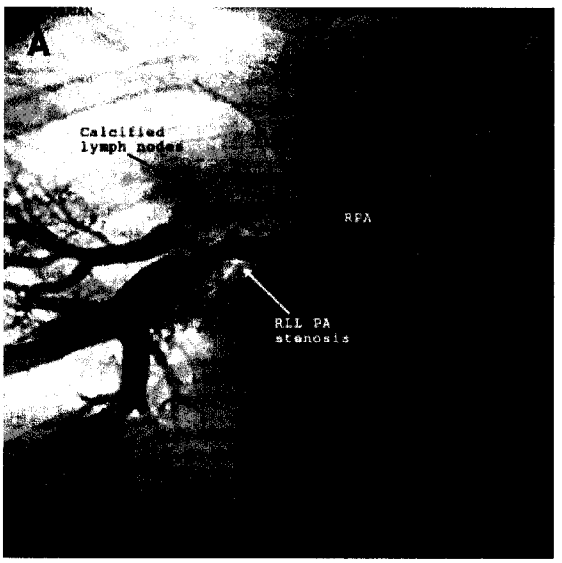

Figure 1.4 Pulmonary artery stenosis angiography, from [4].

Various experimental, mathematical and numerical models have been developed to study flow in elastic tubes. The interaction between an internal flow and the wall deformation involve a rich range of fluid mechanical phenomena. Flow limitation, flow choking, pressure drop limitation, nonlinear pressure drop or flow rate relations, wave propagation and reflection, flow induced instabilities (i.e. wall collapse or buckling, self-excited oscillations or flutter) have been identified and analyzed [98-108]. One may distinguish between self-excited oscillations (i.e. relatively low-frequency oscillations for which membrane inertia is not a critical factor) and flutter (i.e. high-frequency oscillations for which membrane inertia is generally significant) [98], although this distinction is sometimes blurred. Furthermore, experimental studies show that flow limitation is a necessary but not sufficient condition for the onset of self-excited oscillations or flutter [109, 110]. Flow limitation refers to a flow rate which has become independent of the pressure drop along the tube, possibly decreasing as the pressure drop increases [111]. Collapsible conduits set up on the laboratory bench reveal that self-excited oscillations often accompany the flow limitation behavior, as long as the threshold Reynolds number is exceeded (i.e. at about 300) [112], which is well within the physiological range for several large artery such as the carotid, and the pulmonary artery. Simplified one- or two-dimensional theoretical models have established that a source of energy dissipation is necessary for oscillations [112]. The phase lag between the events in the tube that initiate

collapse and the retardation of the downstream flow seems to be an essential part of the process whereby the oscillations extract energy from the steady component of the flow through the tube. The oscillatory part of a pulsatile flow may be thought of as an 'added expense' that reduces the efficiency of the flow, since any power expenditure on it does not produce net forward flow [113].

Flow through a collapsible tube has been extensively studied in the laboratory for well over half a century [114]. Experimental investigation on the collapse of vein and other thin-walled tubes using Starling's resistor chambers may be found in [102, 107, 115-117]. The typical experimental setup involves a length of flexible, collapsible tubing mounted at either end on a rigid support [118] (*Figure 1.5*). Upstream and downstream fluid reservoirs are provided to drive flow through the tube and to regulate the upstream and downstream pressures [119]. The flexible tube is immersed in air or water in such a manner that the external pressure can be monitored and controlled. In the presence of an external pressure gradient, the tube collapse process consists of three phases: the initial transient phase, the quasi-steady phase, and the viscous drainage phase [102]. The initial transient is identified as a period of flow acceleration giving the initial peak observed in the output flow [119]. The quasi-steady emptying is the period where the output flow drops from its initial peak and where there is the establishment of a quasi-steady throat in the region of minimum cross-sectional area. Viscous drainage occurs as the region of collapse increases and the remaining fluid in the tube is forced out as a new equilibrium configuration is approached. If a flow is driven through a Starling Resistor, then as p_{ext} is increased, a constriction typically forms first toward the collapsible tube's downstream end where internal pressure is lowest [98]. Various experimental protocols can then be followed. Increasing the pressure drop along the tube, p_{up}-p_{down}, while keeping the upstream transmural pressure, p_{up}-p_{ext}, fixed leads to flow limitation. Increasing the flow rate while keeping the downstream transmural pressure, p_{down}-p_{ext}, fixed leads to pressure drop limitation, i.e. a restriction on the largest value of p_{up}-p_{down}. As the transmural pressure is lowered below a critical value, the circular cross-section buckles, becoming at first elliptical and then more significantly deformed [120]. During this

phase, the thin-walled tube is very compliant (i.e. large area change for small pressure change) because only wall bending is required for a change of shape, and hence area. At this stage, the small pressure changes associated with flow through the tube (viscous or inertial) may be sufficient to cause collapse. Post-buckling behavior of elastic tubes was numerically investigated by [121]. It was found that an elastic tube of circular cross-section can buckle in a mode with n-fold symmetry (n≥2) for a transmural pressure below the critical buckling pressure of that mode (*Figure 1.6*).

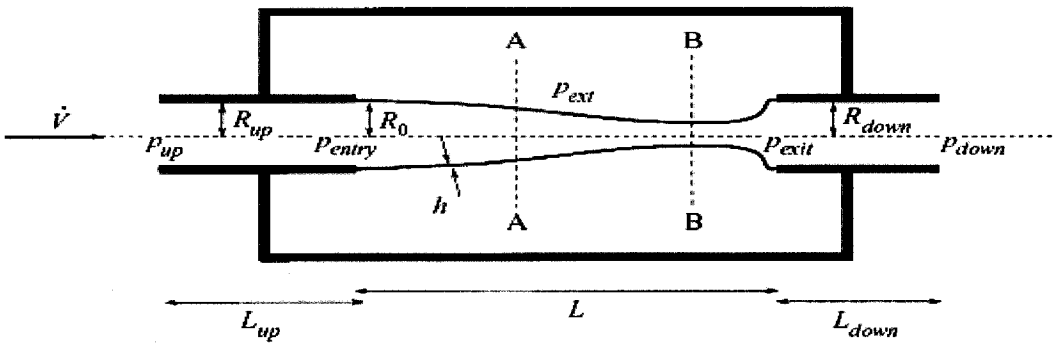

Figure 1.5 Typical Starling resistor chamber setup, from [122].

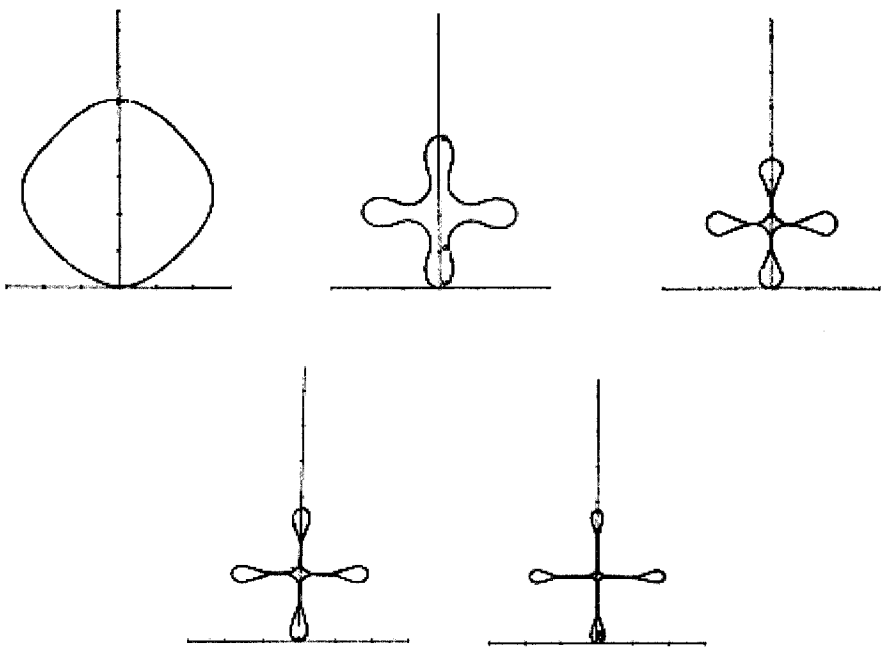

Figure 1.6 The shape of a buckled tube in the mode n=4, from [121].

Primarily interested in the flutter instability of cylindrical shells, Païdoussis and Denise [123] used Flügge's linear shell equations coupled to an inviscid potential flow to determine the growth rate of traveling-wave disturbance to the shell. They found that clamped-clamped shells lose their stability by divergence (buckling), followed by flutter (via Hopf bifurcation) at a slightly higher flow rate. For cylindrical shells with both ends clamped, the increasing flow initially neither damps nor destabilizes the system, but merely reduces the natural frequencies of its modes; at sufficiently high flow velocity, each frequency vanishes, which signifies the onset of buckling (divergence) in that mode. For a particular circumferential wave number, however, two axial modes may coalesce, at a flow velocity just above that for which the second one loses stability by buckling, giving rise to coupled-mode flutter. This led to the proposition that the large displacement self-excited oscillations observed in the experiments could be flutter instabilities or periodic divergence with the antinodes snapping through alternatively between the positive and negative extremes of the modal form involved [124].

Three-dimensional fluid structure interaction models of flow in stenotic collapsible tubes under physiological conditions are still lacking in the literature for the following reasons:

(i) The mechanical properties of the artery under compressions are not readily available [125]. Most existing linear or nonlinear arterial wall model only apply to normal positive pressure conditions. As such, they are no longer valid for instances where the artery is under compression, i.e. for negative transmural pressures. [89, 126].

(ii) The dynamic stenotic artery wall behavior under pulsatile pressure involves large strain and deformation, cyclic tube collapse and expansion. The fluid structure interaction model is best described as a free moving boundary problem where a small change in one field causes a large response in the other [125]. Free moving boundary problems are numerically difficult to handle.

(iii) The geometrical nonlinearities of a severe stenosis and the associated critical flow conditions (i.e. high velocities and large pressure gradients across the throat) are numerically difficult to handle [125].

Experimental evidence suggests that artery with high-grade stenoses may collapse and be subjected to cyclic bending and compression under unsteady pressure conditions [103, 127-133]. The high flow velocities at the throat of a severe stenosis may be sufficient to cause negative transmural pressures (i.e. below the critical value) in the tube [134], possibly inducing tube compression or even collapse. Many investigators (see e.g. [121, 132, 135-142]) have examined the effects of pressure conditions, longitudinal tension, wall compliance, stenosis severity, stenosis eccentricity, and stiffness on the wall deformation and flow characteristics.

In study [143], the focus was on the effects of stenosis severity on the wall deformation, and on the effect of eccentricity of the stenosis on the velocity field. For instance, it was found that stenosis severity greatly affects wall compression, with the highest compression for the steep front side of the stenosis facing the flow. It was reported that in addition to the large flow separation just distal to an eccentric stenosis, the flow was observed to be asymmetric. It was reasoned that the viscous draw from the flow attracts the jet flow to one side of the tube, which gives an asymmetric flow. Furthermore, it was found that the flow asymmetry is accompanied by non-axisymmetric tube deformation. It was argued that the higher flow resistance of an eccentric stenosis leads to reduced flow in comparison to the symmetric case.

A numerical study, based on the finite difference scheme, of unsteady viscous flow in stenotic collapsible tubes may be found in [134]. The tube wall was treated as a free moving boundary whose elastic properties are determined experimentally using a Polyvinyl Alcohol hydrogel artery stenosis model. Tube compression was observed about one diameter distal to the stenosis, consistent with experimental observations. Minimum pressure occurred at the throat, and maximum wall compression was identified at a distal location. It was argued that the increased stiffness of the tube at the stenosis makes

buckling less likely to materialize at this location. Agreement for the pre-buckling stage was found for the experimental and numerical flow rates under steady flow conditions. The disagreement for the post-buckling stage was believed to be linked to the limitation of the axisymmetric model which becomes invalid when the tube collapses. Furthermore, the observed phase shift between the computational and experimental data for the flow rate may be an indication of viscoelasticity of the tube. Although wall collapse could not be directly simulated owing to the limitation of the axisymmetric model, the observed cyclic tube compression was treated as a clear indication of wall collapse.

A refinement of the previous study may be found in [125], where a thin shell model is used for the tube wall. It is claimed by Tang et al., that the thin shell theory provides a better interpretation of the tube law under both expansion and collapsed conditions. As such, the thin shell model would provide more accurate information about wall deformation, wall collapse, and the flow velocity or pressure field, yielding more accurate predictions about collapse conditions. However, it was not possible to gather detailed stress distribution in the tube wall, owing to the thin-wall assumptions. Thus, the extent of compressive stress was inferred from wall compression and collapse. The findings also reinforce the validity of the observations from earlier investigations [138, 143], namely, cyclic tube compression and collapse, negative transmural pressure and high shear stress at the throat of the stenosis, flow recirculation and low shear stress just distal to the stenoses were observed under physiological conditions. These critical flow and mechanical conditions are believed to be related to platelet aggregation, thrombus formation, and excessive artery fatigue. Maximum axial velocity was noticed at the throat of the stenosis. It was concluded that tube geometry is one of the most important factors affecting flow and wall behavior. Stenosis severity and pressure conditions were found to be the dominant factors affecting wall compression and collapse. Post-buckling behavior was speculated on as follows: if the upstream pressure was high enough and downstream pressure low enough, the tube would collapse and might remain in this configuration, even for a further drop in upstream pressure. Once the flow choked, fluttering would ensue, with noticeable clinical symptoms for the patient.

Collapse in high-grade stenosis during pulsatile flow experiments was investigated in [81]. In this study, an improved model of arterial stenosis (i.e. thick-wall in the stenotic region) was created using an elastomer with an incremental modulus of elasticity matched to a bovine carotid artery in the relevant range of collapse. Pulsatile flow experiments with this model characterized the range of conditions under which flow choking occurs. The dynamic stenosis severity through the pulse cycle was found to be significantly greater than the nominal value. The results indicated that flow choking and stenotic compression may be significant in thick-walled stenoses subjected to pulsatile flow conditions. The upstream and downstream phase difference of flow rate and pressure was attributed to the compliance of the straight tube portion and to the resistance of the stenosis model. It was noted that the throat of the stenosis does not collapse easily, because of the structural stiffening from the thicker wall and smaller diameter at this location, than elsewhere in the tube. In agreement with previous work [144, 145], this experiment showed that the collapse phenomenon does not depend strongly on upstream pulsatility. The average downstream pressure during collapse is similar to steady flow conditions. The steady flow observation that stenosis severity is the most dominant factor for flow choking [146, 147] still applies for pulsatile flow conditions. However, the flow rate reduction by the high stenosis severity is compounded by the frequency effect.

1.4 Thesis Objectives

The focus of this thesis is to numerically investigate the three-dimensional effects of spatial configuration on the wall motion and hemodynamic of the pulmonary artery, taking into account fluid structure interaction. ***The hypothesis of this study is that some configurations of serial pulmonary artery stenoses are more susceptible to collapse under physiological conditions.*** The collapse of a compliant arterial stenosis may cause flow choking, which would limit the flow reserve to major vital vascular beds such as the lungs, potentially leading to a lethal ventilation-perfusion mismatch. It is probable that some particular morphology would have a higher vulnerability to compromise the blood transportation biological function of a healthy artery, by producing identifiable regions of retrograde flow. In addition to energy losses, these are believed to affect the progression of arterial dysfunction by providing an auspicious environment for platelet aggregation, thrombus formation, cell adhesion, and for prolonging the cell residence time. Thus, the primary aim of this study is to characterize the macroscopic behavior of wall motion distal to the second stenosis. The secondary intent is to examine the details of the three-dimensional velocity field. The broader goal is to generate relevant morphological and functional information on which surgical intervention decisions may be based.

Chapter 2.

Computational Perspective

This chapter will present the Arbitrary Lagrangian Eulerian (*ALE*) formulation in the following manner: basic concepts, key mapping relationships, governing partial differential equations, smoothing algorithms, advection schemes, and the conditional stability of explicit time integration. The aim is to reveal the underlying concepts, theory and intrinsic limitations behind the *ALE* formulation. This will naturally lead to a more substantial discussion about the implementation phase.

2.1 Arbitrary Lagrangian Eulerian Formulation

2.1.1 Basic Concepts

An early version of the *ALE* method was formulated by Hirt et al. [148]. The general kinematical theory supporting the *ALE* framework was later added by Hugues et al. [149]. As the name suggests, *ALE* description are arbitrary combination of the Lagrangian and Eulerian methods. The term arbitrary refers to the fact that the combination is specified by the user through the selection of mesh motion [150]. The Lagrangian and Eulerian viewpoints have complementary virtues, and the aim of the *ALE* formulation is to capture the best of both [151]. The Lagrangian finite element calculations are characterized by a coordinate system that moves with the material, i.e. nodal trajectories and element quadrature points remain coincident with material point trajectories [152]. Accordingly, each computational element always contains the same material elements. This facilitates the treatment of complicated boundaries: (i) material interfaces can be specifically delineated and precisely followed, (ii) free-surface boundary conditions are easily applied, and (iii) curved rigid boundaries of arbitrary shape can be present. Thus, history-dependent materials can be treated accurately because of the ability to follow material points. However, when the material is severely deformed, Lagrangian elements become similarly distorted since they deform with the material

[150]. The approximation accuracy of the elements then deteriorates, particularly for higher-order elements. Furthermore, the Jacobian determinants may become negative at quadrature points, aborting the calculations or causing severe local inaccuracies. In addition, the conditioning of the linearized Newton equations deteriorates and explicit stable time steps decrease markedly. Remeshing severely distorted Lagrangian meshes is burdensome and introduces errors due to projections.

For the Eulerian finite elements method, the elements are fixed in space and material convects through the elements, i.e. the nodes are coincident with spatial points, and the material point at a given quadrature point changes with time [150]. The convection of material through the elements complicates the treatment of boundary conditions, constitutive equations and updates. It may also introduce accounting details associated with advecting mixed elements so that an element does not donate more of a material than it originally contained [151]. However, the advantage of Eulerian finite elements is that they undergo no distortion due to material motion (i.e. element lengths remain constant in time. Therefore, no degradation in accuracy occurs because of material deformation). Thus, Eulerian meshes are most appealing for modeling problems with very large deformation.

As a mixed viewpoint, the *ALE* approach is most suited to the problem of concern in this thesis. It provides a framework to effectively deal with the moving interface between the fluid and the structure (i.e. between the pulsatile blood flow and the compliant vascular wall). To summarize, the salient feature of the *ALE* formulation is the capability to control mesh geometry independently from material geometry. Moving vertices can: (i) flow with the material as in Lagrangian computing, (ii) remain fixed as in Eulerian computing, or (iii) move in an arbitrarily prescribed way yielding a continuous rezoning capability. The *ALE* formulation is a natural approach in dealing with moving boundaries, free surfaces, large deformation and interface contact problems [153].

2.1.2 Key Mapping Relations of the ALE Domains

The *ALE* approach is based on the arbitrary movement of a referential domain, introduced in addition to the material and spatial domains (*Figure 2.1*). The fluid mechanics problem is posed on the spatial domain, which is generally in motion because of the moving interface to the adjoining structures [154]. The material domain (also generally in motion) is thought of as the domain occupied at time t = 0 by the material particles which occupy the spatial domain at time t. The referential domain is fixed throughout, and its image at time t under a prescribed mapping is the spatial domain (i.e. the spatial domain is a moving mesh and the referential domain is a reference state of the moving mesh). The Eulerian description is regarded as a special case in which the spatial domain is fixed throughout (i.e. it always coincides with the referential domain). The Lagrangian description is another special case of the *ALE* concept in which the material domain coincides with the spatial domain (i.e. nodes move with material particles).

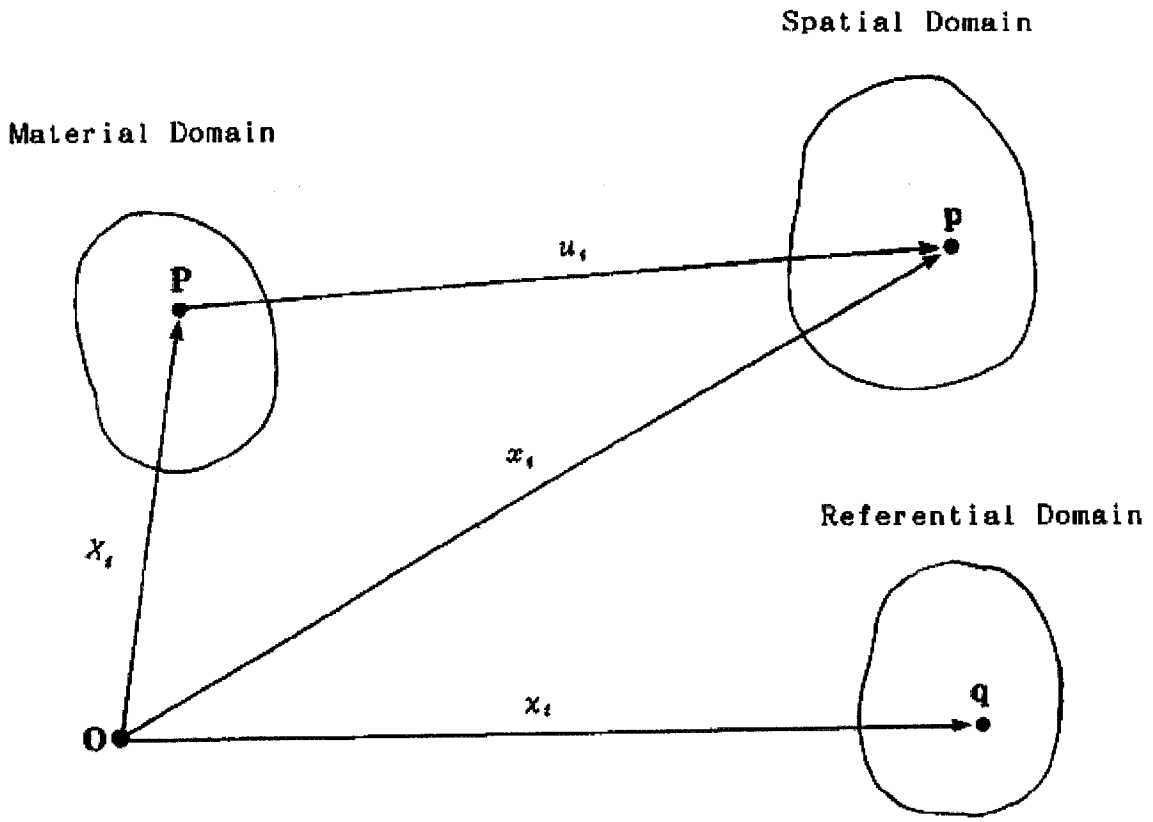

Figure 2.1 Arbitrary Lagrangian Eulerian coordinate systems, from [152].

The material points of a continuous medium at time $t = 0$ occupy the initial region lying in the material domain. The position vector of a material point P in this region is given by:

$$X = (X_1, X_2, X_3) \tag{2.1}$$

The coordinates X_i are called material coordinates [152]. In the deformed configuration the particle originally at P is located at the point p and has the position vector:

$$x = (x_1, x_2, x_3) \tag{2.2}$$

The coordinates x_i which give the current position of the particle, are called spatial coordinates [152]. In the Lagrangian description the motion of the body carries various material particles through various spatial positions, which is mathematically expressed by the relation:

$$x_i = x_i(X_j, t) \tag{2.3}$$

This relation may be interpreted as a mapping of the initial configuration into the current configuration [152]. Furthermore, this mapping should be continuous, single-valued and possess a unique inverse for the Eulerian description as:

$$X_i = X_i(x_j, t) \tag{2.4}$$

The necessary and sufficient condition for the inverse function (2.4) to exist is that the Jacobian determinant should not vanish [152].

$$J = \det\left|\frac{\partial x_i}{\partial X_j}\right| \tag{2.5}$$

In addition, a referential coordinate system is defined [152], which is independently prescribed as a function of space and time by:

$$\chi_i = \chi_i(x_j, t) \tag{2.6}$$

By analogy to (2.5), one may define the Jacobian for the transformation between the referential and spatial coordinates [152]:

$$\overline{J} = \det\left|\frac{\partial x_i}{\partial \chi_j}\right| \tag{2.7}$$

With the above concepts in mind, we now introduce the tensor material derivatives of velocity and acceleration. In fluid mechanics, the rate of change of various kinematical quantities is generally more important than the quantities themselves. Let f be any physical quantity which is a continuous function of the spatial variables x_i and time t. Then, in the case of the Lagrangian description, the material derivative is defined by [152]:

$$f,t_{[X]} = \left.\frac{\partial f}{\partial t}\right|_{X_i} \tag{2.8}$$

where the particle time derivative $\partial f/\partial t$ is taken with X_i held constant.

Similarly, the spatial derivative is given by [152]:

$$f,t_{[x]} = \left.\frac{\partial f}{\partial t}\right|_{x_i} \tag{2.9}$$

where the particle time derivative $\partial f/\partial t$ is taken with x_i held constant.

The referential derivative is [152]:

$$f,t_{[\chi]} = \left.\frac{\partial f}{\partial t}\right|_{\chi_i} \tag{2.10}$$

where the particle time derivative $\partial f/\partial t$ is taken with χ_i held constant.

The velocity of a material particle is given by [152]:

$$v_i = \left.\frac{\partial x_i}{\partial t}\right|_{X_i} \tag{2.11}$$

and the mesh velocity is defined as [152]:

$$w_i = \left.\frac{\partial x_i}{\partial t}\right|_{\chi_i} \tag{2.12}$$

The difference between these two velocities is called the convective velocity [152], as denoted by c_i:

$$c_i = v_i - w_i \tag{2.13}$$

In the case of the *ALE* representation, the material derivative is defined by [152]:

$$\frac{Df}{Dt} = \left.\frac{\partial f}{\partial t}\right|_{\chi_i} + \frac{\partial f}{\partial \chi_i}\frac{\partial \chi_i}{\partial t} \tag{2.14}$$

with the velocity of a material particle given by [152]:

$$v_i = \frac{\partial x_i(\chi_j, t)}{\partial t} = \left.\frac{\partial x_i}{\partial t}\right|_{\chi_i} + \frac{\partial x_i}{\partial \chi_j}\frac{\partial \chi_j}{\partial t} \tag{2.15}$$

or

$$v_i = w_i + \frac{\partial x_i}{\partial \chi_j}\frac{\partial \chi_j}{\partial t} \tag{2.16}$$

From (2.16), the following equation can be obtained:

$$\frac{\partial \chi_j}{\partial t} = (v_i - w_i)\frac{\partial \chi_j}{\partial x_i} \tag{2.17}$$

Introducing (2.17) into (2.14) yields:

$$\frac{Df}{Dt} = \left.\frac{\partial f}{\partial t}\right|_{\chi_i} + \frac{\partial f}{\partial \chi_i}(v_i - w_i) \tag{2.18}$$

The acceleration components a_i in the case of the *ALE* description are given by [152]:

$$a_i = \left.\frac{\partial v_i}{\partial t}\right|_{\chi_i} + c_j v_{i,j} \tag{2.19}$$

2.1.3 Governing Partial Differential Equations

The governing equations for an incompressible Newtonian fluid in the *ALE* formulation are the conservation of mass, momentum and energy equations. In this section, we shall make explicit and justify the applicable simplifications and assumptions. For the problem at hand, we define the following domains: $\Omega_F(t)$ shall represent the moving spatial domain upon which the fluid motion is described (i.e. the *ALE* description), $\Omega_S(t)$ will denote the domain occupied by the moving structural body (i.e. the Lagrangian description), and $\Gamma_{FS}(t)$ corresponds to the moving interface between $\Omega_F(t)$ and $\Omega_S(t)$, i.e. $\Gamma_{FS}(t) = \Omega_F(t) \cap \Omega_S(t)$. Lastly, Γ_1 describes the inlet surface boundary, while Γ_2 expresses the outlet surface boundary, where both are fixed in space (i.e. the Eulerian description). ρ denotes the fluid density, c_i symbolizes the convective velocity as defined in (2.13).

(i) The conservation of mass equations [150]

$$\rho,t_{[\chi]} + c_i \rho_{,i} + \rho v_{i,i} = 0, \text{ in } \Omega_F(t) \tag{2.20}$$

which may be reduced to:

$$\rho,t_{[\chi]} + c_i \rho_{,i} = 0, \text{ in } \Omega_F(t) \tag{2.21}$$

under the incompressibility condition:

$$v_{i,i} = 0, \text{ in } \Omega_F(t) \tag{2.22}$$

(ii) The momentum equations [150]

The classical form of the problem governing Newtonian fluid flow in a fixed domain consists of the governing equations (*ALE* description of the Navier-Stokes equations) and suitable initial and boundary conditions [150].

$$\rho \dot{v}_i = \rho(v_{i,t[\chi]} + v_{i,j} c_j) = \sigma_{ij,j} + \rho b_i, \text{ in } \Omega_F(t) \tag{2.23}$$

where σ_{ij} is the stress tensor (typically Cauchy), and b_i is the *ith* component of the body force per unit mass. The body force may arise from gravitational field. As argued by [113], in physiological flow problems and flow in tubes in general, the main driving force is usually pressure. Thus, the body force may be neglected as it does not affect the nature of a pulsatile flow.

Neglecting the body force, (2.23) may be reduced to:

$$\rho \dot{v}_i = \rho(v_{i,t[\chi]} + v_{i,j} c_j) = \sigma_{ij,j}, \text{ in } \Omega_F(t) \tag{2.24}$$

The stress tensor σ_{ij} can be written as:

$$\sigma_{ij} = -p\delta_{ij} + \mu(v_{i,j} + v_{j,i}) \tag{2.25}$$

where p is the pressure, μ is the dynamic viscosity and δ_{ij} is the Kronecker's delta [150].

The following boundary conditions and initial condition apply:

$$v_i = f_i(\chi, t), \text{ on } \Gamma_1 \tag{2.26}$$

where f_i is a prescribed function of space and time, and

$$\sigma_{ij} n_j = 0, \text{ on } \Gamma_2 \tag{2.27}$$

where n_j is the unit outward normal vector to Γ_2.

Since Γ_1 and Γ_2 are fixed in space, this leads to:

$$w_i = 0, \text{ on } \Gamma_1 U \Gamma_2 \tag{2.28}$$

The no-slip condition applies on $\Gamma_{FS(t)}$:

$$v_i = w_i, \text{ on } \Gamma_{FS(t)} \tag{2.29}$$

or

$$c_i = 0, \text{ on } \Gamma_{FS(t)} \tag{2.30}$$

In other words, we have the Lagrangian description on $\Gamma_{FS(t)}$.

The velocity field is assumed to be known at $t = 0$ in the whole domain Ω; only one initial condition is needed since the momentum equation is first-order in time:

$$v_i(\chi, 0) = 0 \tag{2.31}$$

(iii) The energy equations [150]

These must be included when coupling with heat transfer or other energy transfer.

$$\rho \dot{e} = (e_{,t[\chi]} + e_{,i} c_i) = \sigma_{ij} v_{i,j} + \rho b_i v_i, \text{ in } \Omega_F(t) \tag{2.32}$$

where e is the internal energy per unit mass [150].

Again, neglecting the body force:

$$\rho \dot{e} = (e_{,t[\chi]} + e_{,i} c_i) = \sigma_{ij} v_{i,j}, \text{ in } \Omega_F(t) \tag{2.33}$$

The term associated with the convective velocity is usually referred to as the "advective" or "convective" term, and accounts for the transport of material past the mesh [151]. It is the additional term in the above equations that makes solving the *ALE* equations much more difficult numerically than the Lagrangian equations. The cost of an advection step is typically two to five times the cost of the Lagrangian time step [155].

We conclude this segment by describing the key steps involved in the execution of an *ALE* time step [151]. There are actually two ways to implement the *ALE* equations. The first method solves the fully coupled equations for computational fluid mechanics. However, this approach can only handle a single material in an element. The alternative approach is referred to as an operator split in the literature, where the calculation is divided into two phases for each time steps. First a Lagrangian phase is performed, in which the mesh moves with the material. In this phase, the changes in velocity and internal energy due to the internal and external forces are calculated. Then, the advection

phase ensues. Transport of mass, internal energy and momentum across cell boundaries are computed. Put more formally, an operator split breaks one set of partial differential equations into two or more sets which are solved sequentially. An operator split decouples the various physical phenomena in the governing equations, and therefore the potential accuracy of the solution is somewhat reduced [156]. The advantage of the operator split over the fully coupled approach is that it breaks very complicated equations into simpler equations that are more easily solved. Algorithms that rely on this method are therefore usually more robust than fully coupled algorithms. For an *ALE* formulation, the use of an operator split is therefore natural because the Lagrangian step remains unchanged and only a separate, independent remap algorithm needs to be added for the Eulerian step. The decoupling of the Lagrangian and Eulerian steps allows for the use of a simple and efficient remap algorithm. However, it is conceded that the operator split places an intrinsic limit on accuracy, and that advection algorithms tend to smooth sharp solution gradients. For many practical problems, advection algorithms are perfectly adequate. The accuracy of second-order advection algorithms is superior to the manual rezoning which is only first-order accurate.

The breakdown of an Eulerian step consists of five smaller steps [151]. The first step is the choice of which mesh sections to remap. One key strategy is to selectively remap sections with highly distorted meshes that are likely to control the time step size. Remapping the entire mesh at every step is prohibitively expensive. Another key idea is that the Eulerian step need not be performed at every time step. In most cases, it is possible to perform the Eulerian step only every ten to twenty time steps. The overall cost of the Eulerian step may be reduced by a factor of ten to twenty while maintaining the benefit of large time steps. Furthermore, accuracy of the calculation is usually unaffected by the frequency of the Eulerian step. The second step involves the decision of where to move the nodes. This step is the most difficult from the standpoint of implementation, and is problem dependent. Smoothing algorithms or relaxation stencils are used for mesh generation in this step. The third step is mass advection. Calculated mass fluxes are used in the momentum advection, the fourth step. Momentum is advected instead of velocities to ensure the conservation of momentum. The final step is the advection of the stress

tensor and the history variables associated with the constitutive models. The next two sections will highlight the salient features that characterize a robust smoothing algorithm and advections scheme, while disclosing some innate drawbacks.

2.1.4 Smoothing Algorithms

One of the oldest relaxation stencils was proposed by Winslow [157, 158]. His equipotential stencil is still widely used because of its stability for a broad range of problems. Stability for mesh relaxation methods means that the method will not distort a mesh any more than its current distortion [151]. The Laplace's equation is inverted, and the stencil is devised such that the mesh forms lines of equal potential on a logically regular mesh. When a solution for Laplace's equation exists, the maximum principle guarantees that the resulting mesh does not overlap itself. The price to pay for this certainty is the following drawbacks. Equipotential relaxation stencils are known to invert elements that are near an indented boundary with a small radius of curvature. Laplace's equation attracts elements to indented boundaries. When the radius is small enough, the lines of equipotential pile up on top of each other, thus resulting in elements with zero volume. Another undesirable response is that the stencil can start to converge from the wrong side of the solution and put a few nodes on the wrong side of the boundary. In spite of these limitations, Winslow's stencil is part of a general class of algorithms called finite difference mesh relaxation stencils. This category is best described as any general algorithm inherently local in nature, given that only regions of a mesh will be moved during a time step, and that the regions flagged for remapping may change from time step to time step. Finite difference mesh relaxation stencils are created by trying to minimize a functional [159] or by inverting the solution to a partial differential equation [157]. The Laplace's equation can be restated as a minimization of the mesh density gradient by using variational calculus. The gradient is a measure of the smoothness of the mesh, and by minimizing it, the elements will tend to be of equal size away from the boundary. This smoothness property is desirable most of the time.

The derivation of the three-dimensional equipotential zoning equations is as follows:

In three dimensions, we define curvilinear coordinates ξ^i *(i=1, 2, 3)* which satisfy Laplace's equation [155]:

$$\nabla^2 \xi^i = 0 \tag{2.34}$$

For a scalar function *A(x, y, z)*, the transformation of its Laplacian from rectangular Cartesian to curvilinear coordinates is given by [155]:

$$\nabla^2 A = \sum_{i,j=1}^{3} g^{ij} A_{\xi^i \xi^j} + \sum_{k=1}^{3} \left(\nabla^2 \xi^k\right) A_{\xi^k} \tag{2.35}$$

where a variable subscript indicates differentiation with respect to that variable. Since the curvilinear coordinates are each assumed to satisfy Laplace's equation, the second summation vanishes [155] and we have:

$$\nabla^2 A = \sum_{i,j=1}^{3} g^{ij} A_{\xi^i \xi^j} \tag{2.36}$$

Letting $A = x, y, z$ successively, the left hand side of (2.36) vanishes in each case and we get three equations [155], which can be written in vector form:

$$\sum_{i,j=1}^{3} g^{ij} \vec{r}_{\xi^i \xi^j} = 0 \tag{2.37}$$

For the purpose of clarity and convenience, we introduce the rule of transformation distinguishing the contravariant (2.38) from the covariant (2.39) component of a vector (or equivalently called tensor of rank one, see e.g. [160]):

$$A'^{i} = \frac{\partial x'^{i}}{\partial x^{j}} A^{j} \tag{2.38}$$

$$A'_{i} = \frac{\partial x^{j}}{\partial x'^{i}} A_{j} \tag{2.39}$$

The components of the contravariant metric tensor g^{ij} in three dimensions are defined to be [155]:

$$g^{ij} \equiv \vec{a}^{i} \cdot \vec{a}^{j} \tag{2.40}$$

where the contravariant base vectors of the transformation from *(x,y,z)* to (ξ^1, ξ^2, ξ^3) are given by *(i, j, k cyclic)* [155]:

$$\vec{a}^{i} \equiv \nabla \xi^{i} = \frac{\vec{a}_{j} \times \vec{a}_{k}}{J} \tag{2.41}$$

where the Jacobian J must be positive to ensure a nonsingular transformation [155]:

$$J = \sqrt{g} = \left| \begin{pmatrix} x_{\xi^1} & y_{\xi^1} & z_{\xi^1} \\ x_{\xi^2} & y_{\xi^2} & z_{\xi^2} \\ x_{\xi^3} & y_{\xi^3} & z_{\xi^3} \end{pmatrix} \right| > 0 \tag{2.42}$$

The covariant base vectors are given by [155]:

$$\vec{a}_i \equiv \vec{r}_{\xi^i} \tag{2.43}$$

where:

$$\vec{r} \equiv x\hat{i} + y\hat{j} + z\hat{k} \tag{2.44}$$

The covariant metric tensor g_{ij} is given by [155]:

$$g_{ij} \equiv \vec{a}_i \cdot \vec{a}_j \tag{2.45}$$

Substituting (2.41) into (2.40), and making use of the vector identity [155]:

$$\left(\vec{a}\times\vec{b}\right)\cdot\left(\vec{c}\times\vec{d}\right) \equiv \left(\vec{a}\cdot\vec{c}\right)\left(\vec{b}\cdot\vec{d}\right) - \left(\vec{a}\cdot\vec{d}\right)\left(\vec{b}\cdot\vec{c}\right) \tag{2.46}$$

we obtain:

$$gg^{ii} = \vec{a}_j{}^2\vec{a}_k{}^2 - \left(\vec{a}_j\cdot\vec{a}_k\right)^2 = g_{jj}g_{kk} - \left(g_{jk}\right)^2 \tag{2.47}$$

$$gg^{ij} = \left(\vec{a}_i\cdot\vec{a}_k\right)\left(\vec{a}_j\cdot\vec{a}_k\right) - \left(\vec{a}_i\cdot\vec{a}_j\right)\vec{a}_k{}^2 = g_{ik}g_{jk} - g_{ij}g_{kk} \tag{2.48}$$

Substituting (2.43) into (2.47) and (2.48) and simplifying the notation to [155]:

$$\xi \equiv \xi^1, \eta \equiv \xi^2, \zeta \equiv \xi^3 \tag{2.49}$$

We get the three diagonal components [155]:

$$\begin{aligned} gg^{11} &= \vec{r}_\eta^{\,2}\vec{r}_\zeta^{\,2} - \left(\vec{r}_\eta \cdot \vec{r}_\zeta\right)^2 \\ gg^{22} &= \vec{r}_\zeta^{\,2}\vec{r}_\xi^{\,2} - \left(\vec{r}_\zeta \cdot \vec{r}_\xi\right)^2 \\ gg^{33} &= \vec{r}_\xi^{\,2}\vec{r}_\eta^{\,2} - \left(\vec{r}_\xi \cdot \vec{r}_\eta\right)^2 \end{aligned} \tag{2.50}$$

and the three off diagonal components of this symmetric tensor [155]:

$$\begin{aligned} gg^{12} &= \left(\vec{r}_\xi \cdot \vec{r}_\zeta\right)\left(\vec{r}_\eta \cdot \vec{r}_\zeta\right) - \left(\vec{r}_\xi \cdot \vec{r}_\eta\right)\vec{r}_\zeta^{\,2} \\ gg^{23} &= \left(\vec{r}_\eta \cdot \vec{r}_\xi\right)\left(\vec{r}_\zeta \cdot \vec{r}_\xi\right) - \left(\vec{r}_\eta \cdot \vec{r}_\zeta\right)\vec{r}_\xi^{\,2} \\ gg^{31} &= \left(\vec{r}_\zeta \cdot \vec{r}_\eta\right)\left(\vec{r}_\xi \cdot \vec{r}_\eta\right) - \left(\vec{r}_\zeta \cdot \vec{r}_\xi\right)\vec{r}_\eta^{\,2} \end{aligned} \tag{2.51}$$

Hence, we may rewrite (2.37) in the form [155]:

$$g\left(g^{11}\vec{r}_{\xi\xi} + g^{22}\vec{r}_{\eta\eta} + g^{33}\vec{r}_{\zeta\zeta} + 2g^{12}\vec{r}_{\xi\eta} + 2g^{23}\vec{r}_{\eta\zeta} + 2g^{31}\vec{r}_{\zeta\xi}\right) = 0 \tag{2.52}$$

or in terms of the Cartesian coordinates [155]:

$$\alpha_1\vec{r}_{\xi\xi} + \alpha_2\vec{r}_{\eta\eta} + \alpha_3\vec{r}_{\zeta\zeta} + 2\beta_1\vec{r}_{\xi\eta} + 2\beta_2\vec{r}_{\eta\zeta} + 2\beta_3\vec{r}_{\zeta\xi} = 0 \tag{2.53}$$

where:

$$\alpha_1 = \left(x_\eta y_\zeta - x_\zeta y_\eta\right)^2 + \left(x_\eta z_\zeta - x_\zeta z_\eta\right)^2 + \left(y_\eta z_\zeta - y_\zeta z_\eta\right)^2$$

$$\alpha_2 = \left(x_\zeta y_\xi - x_\xi y_\zeta\right)^2 + \left(x_\zeta z_\xi - x_\xi z_\zeta\right)^2 + \left(y_\zeta z_\xi - y_\xi z_\zeta\right)^2$$

$$\alpha_3 = \left(x_\xi y_\eta - x_\eta y_\xi\right)^2 + \left(x_\xi z_\eta - x_\eta z_\xi\right)^2 + \left(y_\xi z_\eta - y_\eta z_\xi\right)^2$$

$$\beta_1 = \left(x_\xi x_\zeta + y_\xi y_\zeta + z_\xi z_\zeta\right)\left(x_\eta x_\zeta + y_\eta y_\zeta + z_\eta z_\zeta\right)$$
$$-\left(x_\xi x_\eta + y_\xi y_\eta + z_\xi z_\eta\right)\left(x_\zeta{}^2 + y_\zeta{}^2 + z_\zeta{}^2\right)$$

$$\beta_2 = \left(x_\eta x_\xi + y_\eta y_\xi + z_\eta z_\xi\right)\left(x_\xi x_\zeta + y_\xi y_\zeta + z_\xi z_\zeta\right)$$
$$-\left(x_\zeta x_\eta + y_\zeta y_\eta + z_\zeta z_\eta\right)\left(x_\xi{}^2 + y_\xi{}^2 + z_\xi{}^2\right)$$

$$\beta_3 = \left(x_\eta x_\zeta + y_\eta y_\zeta + z_\eta z_\zeta\right)\left(x_\xi x_\eta + y_\xi y_\eta + z_\xi z_\eta\right)$$
$$-\left(x_\xi x_\eta + y_\xi y_\eta + z_\xi z_\eta\right)\left(x_\eta{}^2 + y_\eta{}^2 + z_\eta{}^2\right) \qquad (2.54)$$

Finally, central differencing is then applied on (2.53) in a cube in the rectangular *(ξ, η, ζ)* space with unit spacing between the coordinate surfaces. The subscript *i* represents the ξ direction, *j* the η direction and *k* the ζ direction. The following finite difference approximations for the coordinate derivatives may be obtained [155]:

$$
\begin{aligned}
\vec{r}_{\xi} &= \left(\vec{r}_{i+1} - \vec{r}_{i-1}\right) \\
\vec{r}_{\eta} &= \left(\vec{r}_{j+1} - \vec{r}_{j-1}\right) \\
\vec{r}_{\zeta} &= \left(\vec{r}_{k+1} - \vec{r}_{k-1}\right) \\
\vec{r}_{\xi\xi} &= \left(\vec{r}_{i+1} - 2\vec{r} + \vec{r}_{i-1}\right) \\
\vec{r}_{\eta\eta} &= \left(\vec{r}_{j+1} - 2\vec{r} + \vec{r}_{j-1}\right) \\
\vec{r}_{\zeta\zeta} &= \left(\vec{r}_{k+1} - 2\vec{r} + \vec{r}_{k-1}\right) \\
\vec{r}_{\xi\eta} &= \frac{1}{4}\left[\left(\vec{r}_{i+1,j+1} + \vec{r}_{i-1,j-1}\right) - \left(\vec{r}_{i+1,j-1} + \vec{r}_{i-1,j+1}\right)\right] \\
\vec{r}_{\eta\zeta} &= \frac{1}{4}\left[\left(\vec{r}_{j+1,k+1} + \vec{r}_{j-1,k-1}\right) - \left(\vec{r}_{j+1,k-1} + \vec{r}_{j-1,k+1}\right)\right] \\
\vec{r}_{\zeta\xi} &= \frac{1}{4}\left[\left(\vec{r}_{i+1,k+1} + \vec{r}_{i-1,k-1}\right) - \left(\vec{r}_{i+1,k-1} + \vec{r}_{i-1,k+1}\right)\right]
\end{aligned}
\tag{2.55}
$$

where for brevity we have omitted subscripts *i, j, k (e.g., k+1 stands for i, j, k+1).*

2.1.5 Advection Schemes

For the purpose of clarity, it will be useful to introduce the following definitions [151]. A "remap" is the process of mapping the original mesh into another mesh, whether or not the new mesh is an arbitrary mesh or a small perturbation away from the old mesh. "Rezoning" maps one mesh to another arbitrary mesh by interpolating values for the new mesh from the old mesh. An "advective" or "Eulerian" remap calculates the transport of material between adjacent elements as a mesh is moved. For elements that are modeled with an equation of state, the total number of solution variables to be transported is six [155]. These are the density, internal energy, viscosity and the three components of velocity. The nodal velocities add an extra three solution variables that must be transported, and they must be advected separately from the other solution variables because they are centered at the nodes and not in the elements. In addition, momentum is used as an advection variable to guarantee the conservation of momentum, and it is a

product of the node-centered velocity and the element-centered density. Thus, the necessity of using very simple and efficient advection algorithms becomes apparent.

There are a number of fundamental properties that remap algorithms should have [151]. For obvious reasons, remap algorithms should be accurate. Traditional error analysis gives the order of the algorithm, indicating the degree of the polynomial that is advected without error. First-order accurate algorithms are too diffusive for most applications. Some algorithms are second-order when the solution is smooth, but degrade to first-order around discontinuities to preserve their stability. These generate good solutions when used with lower-order elements, such as four-node quadrilaterals. A useful test is the propagation of a single wave over long distances. This test demonstrates how well an advection algorithm will maintain steep gradients in the solution. The second requirement is that remap algorithms should be conservative, that is, the integral of any quantity over the material domain should remain unchanged by the remap. Variables before and after the remap at time t are superscripted with – and + respectively:

$$\Phi\left(t^{+}\right)=\Phi\left(t^{-}\right)=\int_{\Omega}\Phi\left(x\right)d\Omega \tag{2.56}$$

The third property is that a remap algorithm should be consistent in the sense that if the new mesh is identical to the original mesh, then all quantities should remain unchanged by the remap. Last but not least, we are naturally concerned with stability of the advection scheme. However, unconditional stability is not a necessity because the Lagrangian step is only conditionally stable. This will be made clear in the next section, which deals with the conditional stability of explicit time integration.

2.1.6 Explicit Time Integration and Conditional Stability

Explicit finite element programs are more efficient than implicit programs for solving transient, large deformation problems that require a high-resolution of the spatial domain [151]. The cost of an implicit time step is ten to a thousand times more expensive than an explicit one, owing to the need to solve the linear equations [161]. The central difference method is among the most popular of the explicit methods in computational mechanics and physics. The central difference method is developed from the central difference formulas for the velocity and acceleration [162]. The value of the derivative at the center of a time interval is obtained from the difference of the function values at the ends of the interval, hence the name central difference formulas. Most algorithms utilize a variable time step. This is essential for practical calculations since the stable time step size changes as the mesh deforms and the wave speed changes due to stress.

The time increments are defined by:

$$\Delta t^{n+1/2} = t^{n+1} - t^n, t^{n+1/2} = \frac{1}{2}\left(t^{n+1} + t^n\right), \Delta t^n = t^{n+1/2} - t^{n-1/2} \tag{2.57}$$

The velocities are approximated by:

$$v^{n+1/2} = \frac{d^{n+1} - d^n}{t^{n+1} - t^n} = \frac{1}{\Delta t^{n+1/2}}\left(d^{n+1} - d^n\right) \tag{2.58}$$

where d denotes the nodal displacement. As can be seen, the velocities are defined at the midpoints of the time intervals, also called half steps or midpoint steps.

Rearranging (2.58) gives:

$$d^{n+1} = d^n + \Delta t^{n+1/2} v^{n+1/2} \tag{2.59}$$

The acceleration is approximated by:

$$a^n = \frac{v^{n+1/2} - v^{n-1/2}}{t^{n+1/2} - t^{n-1/2}} \tag{2.60}$$

Rearranging (2.60) yields:

$$v^{n+1/2} = v^{n-1/2} + \Delta t^n a^n \tag{2.61}$$

By substituting (2.58) and its counterpart for the previous time step into (2.60), the acceleration can be expressed directly in terms of the displacement:

$$a^n = \frac{\Delta t^{n-1/2}\left(d^{n+1} - d^n\right) - \Delta t^{n+1/2}\left(d^n - d^{n-1}\right)}{\Delta t^{n+1/2}\Delta t^n \Delta t^{n-1/2}} \tag{2.62}$$

Consider the time integration of the following equation of motions, which arises from the discretization of the momentum equations for a Lagrangian mesh:

$$Ma^n = f^n = f^{ext}\left(d^n, t^n\right) - f^{\text{int}}\left(d^n, t^n\right) \tag{2.63}$$

where f^{int} are the internal nodal forces and f^{ext} are the external nodal forces. Nodal forces are always defined so that they are conjugate to the nodal displacements in the sense of work (i.e. the scalar product of an increment of nodal displacement with the nodal force gives an increment of work). (2.63) is also called the semi-discrete momentum equations because of the lack of discretization of time [162].

Substituting (2.63) into (2.61) gives:

$$v^{n+1/2} = v^{n-1/2} + \Delta t^n M^{-1} f^n \tag{2.64}$$

At any time step n, the displacement d^n are known. The nodal forces f^n can be determined by sequentially evaluating the strain-displacement equations, constitutive equations, and the nodal external forces [162]. Once the right hand side of (2.63) is evaluated, $v^{n+1/2}$ may

be used in (2.59) to obtain d^{n+1}. Thus, update of the nodal velocities and nodal displacements can be accomplished without solving any equations provided the mass matrix M is diagonal (i.e. in an explicit method, the time integration of the discrete momentum equations does not require the solution of any equations). One caveat is that the avoidance of solution of equations hinges critically on the use of a lumped mass matrix (i.e. diagonal). For a consistent mass matrix (i.e. non-diagonal), the update involves the solution of ordinary differential equations of second-order in time.

Despite the ease of implementation and robustness of the numerical algorithm, explicit time integration is only conditionally stable. The time step size of explicit programs is limited by the Courant stability criterion which says that the largest stable time step is the minimum time necessary for a sound wave to cross the smallest element in the mesh [151]. This is mathematically expressed as [162]:

$$\Delta t = \alpha \Delta t_{crit}, \Delta t_{crit} = \min \frac{l_e}{c_e} \tag{2.65}$$

where l_e is the characteristic length of element e, c_e is the current wave speed in element e, and α is a reduction factor that accounts for the destabilizing effects of nonlinearities.

The ratio of the time step to the critical time step, α, is called the Courant number. It was first proposed by Courant, Friedrichs and Lewy [162]. The implication is that the critical time step decreases with mesh refinement and increasing material stiffness. As the analysis proceeds, Lagrangian elements stretch in length and shrink in width, and the size of the time step decreases [151]. When the size of the time step becomes too small, continuing the analysis becomes prohibitively expensive. On the other extreme, if the time step exceeds the critical value, the solution will grow unboundedly [162]. To summarize, the cost of an explicit simulation is independent of the frequency range of interest and depends only on the size of the model and the number of time steps. This leads us to the next section where the numerical implementation is discussed.

2.2 Numerical Implementation

2.2.1 Geometry Model

The central objective of this thesis is to numerically investigate the three-dimensional effects of spatial configuration on the wall motion and hemodynamic of the pulmonary artery, taking into account fluid structure interaction. Motivated by the physiological phenomena of collapse and flow limitation for a serial pulmonary artery stenosis, we are interested in investigating the effect of two geometrical parameters: the relative distance and the angular orientation between the two stenoses. For clinical relevance, each stenosis is characterized by a *'mild'* nominal area occlusion of 50 percent and a nominal eccentricity of 100 percent (as per *section 1.2.2*, refer to *Figures 2.2-2.6* for the specific characteristics of each case). From a plaque rupture viewpoint, stiffer stenoses are less dangerous than softer ones, which is consistent with clinical observations [143]. In addition, an eccentric stenosis is more unstable than a concentric one. It has been experimentally demonstrated that the required buckling pressure to collapse artery with eccentric cross-sections is 30 percent lower than for an axisymmetric tube [127].

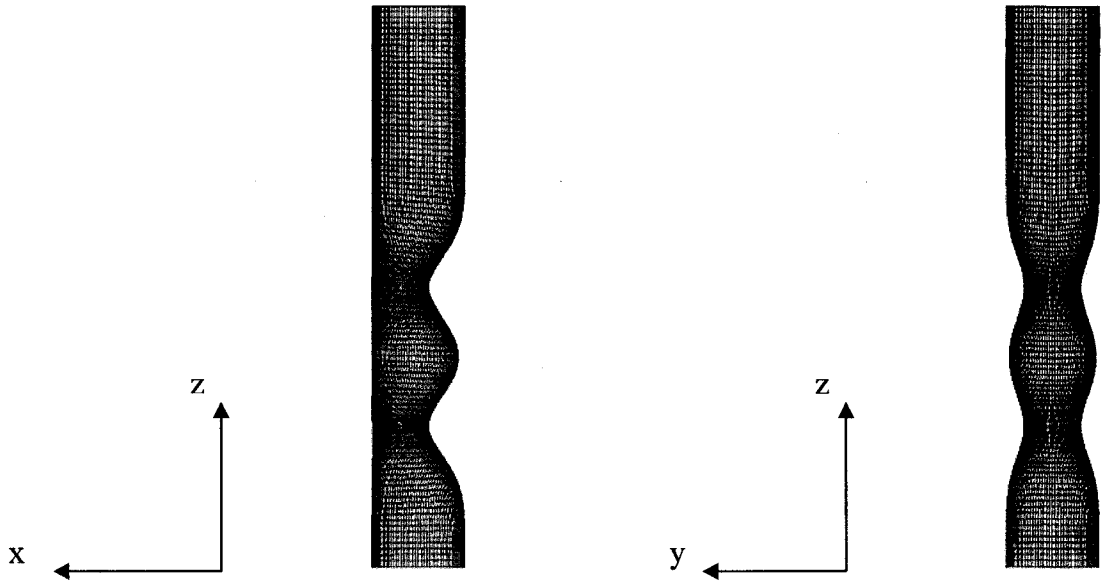

Figure 2.2 Case 1; distance between stenoses: 25% of tube length L (1.667 x D), angular offset between stenoses: 0°.

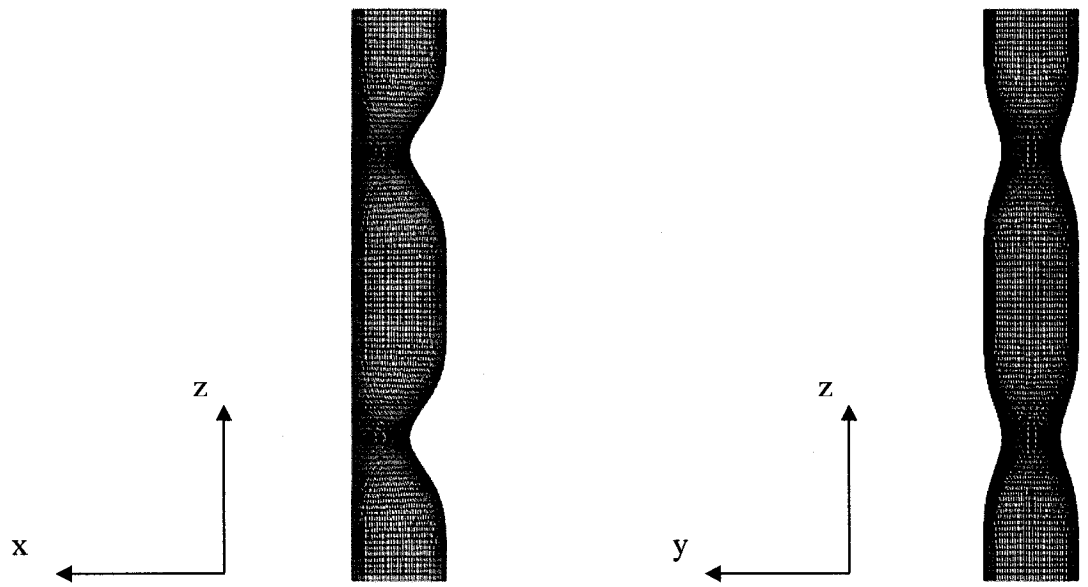

Figure 2.3 Case 2; distance between stenoses: 50% of tube length L (3.333 x D), angular offset between stenoses: 0°.

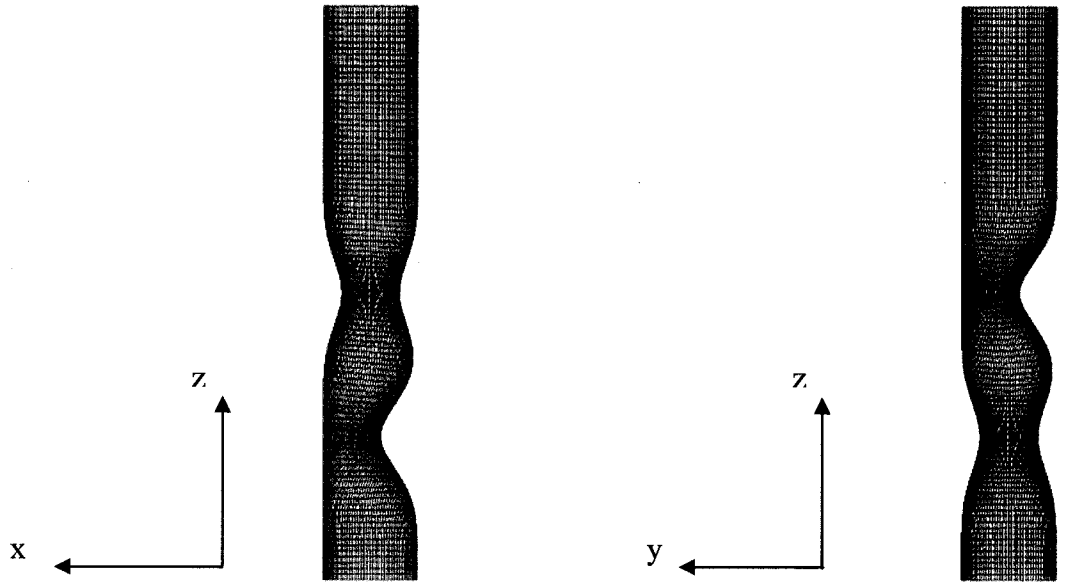

Figure 2.4 Case 3; distance between stenoses: 25% of tube length L (1.667 x D), angular offset between stenoses: 90°.

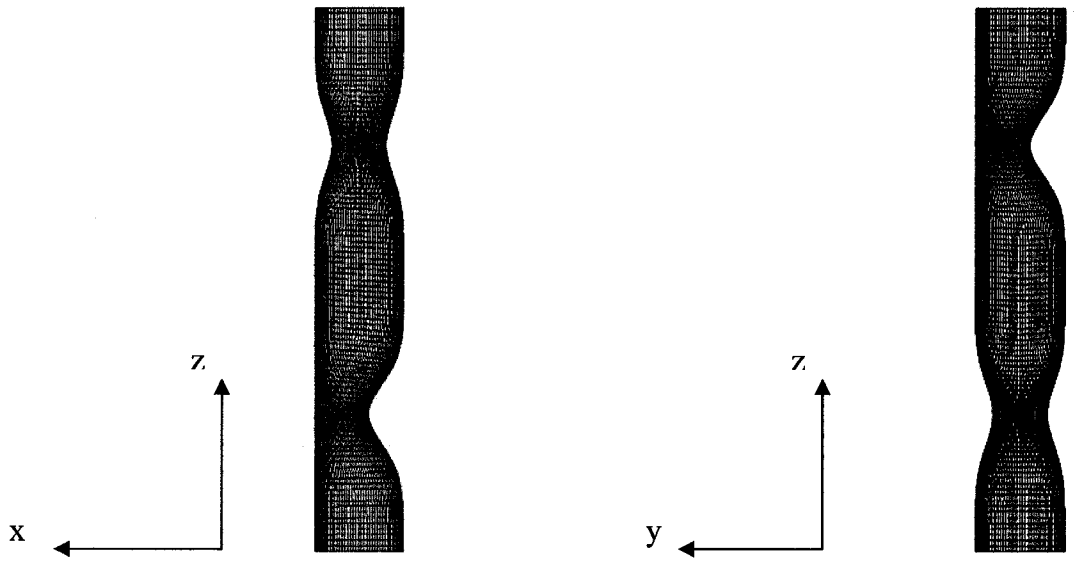

Figure 2.5 Case 4; distance between stenoses: 50% of tube length L (3.333 x D), angular offset between stenoses: 90°.

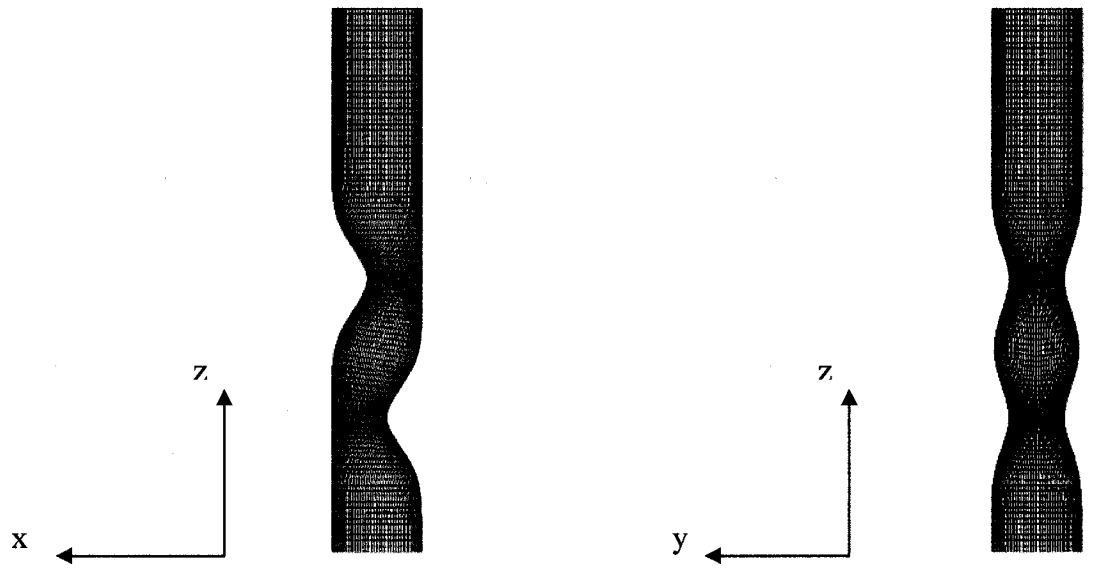

Figure 2.6 Case 5; distance between stenoses: 25% of tube length L (1.667 x D), angular offset between stenoses: 180°.

Cases (1, 3 & 5) will permit us to study the effect of the closeness between the constrictions. This set will also enable us to examine the influence of angular orientation. Conversely, cases (2 & 4) will allow us to determine the impact of positioning the distal stenosis near the outlet.

Since the bulk of the literature on tube collapse considers circular cross-section, we shall assume this undeformed reference state for ease of comparison. In the context of a pediatric pulmonary artery, we are selecting a 6 *mm* nominal diameter, which lies on the lower end of the published angiocardiographic diameter data, for infants ranging from 1 month to 14.5 years [163]. It has been documented that one of the loads bearing layer, the media, may account for up to 10 percent of the external diameter of the vessel [7]. In view of this observation, we select a thickness of 0.3 *mm*. Regarding our choice of cross-section, it should be emphasized that the major pulmonary artery are actually elliptical in cross-section rather than circular [9]. An opening angle experiment is a convenient way to demonstrate that the arterial wall is not axisymmetric since the zero-stress state of an artery is not a tube [164]. The implication of an elliptical cross-section or any non-circular cross-section is that it produces a less efficient flow [165, 166]. Flow inefficiency in a tube of non-circular cross-section manifests itself in terms of lower flow rate for a

given pressure gradient (or equivalently, higher pressure gradient for a given flow rate) [113]. For the same pressure gradient and perimeter, the flow rate for an elliptical cross-section tube for a major to minor axis ratio of 2 is lower by a factor of 64/125 when compared with the circular cross-section tube. Although the above remarks strictly apply to a steady flow, the reduction in efficiency for a pulsatile flow will be compounded by the effect of frequency [167].

With the above in mind, the spatial coordinates of the geometry are generated using the commercial package Matlab® (MathWorks, Inc.). Adopting the methodology developed by Tang et al. [143], we move the cross-sections to one side such that all remain circular, with a resulting straight side for each stenotic section. The surfaces are lofted with the use of the modeling software Rhinoceros® (McNeel). Meshing is performed with the pre-processor module of ANSYS® (Ansys). The simplified *ALE* formulation is implemented using the commercial package LS-DYNA® (Livermore Software Technology Corporation). The reference coordinate system is Cartesian *(x,y,z)*, with the z coordinate aligned in the direction of the tube axis, while x and y are the transverse coordinates. The origin is located at the centre of the tube inlet (*Figure 2.7*).

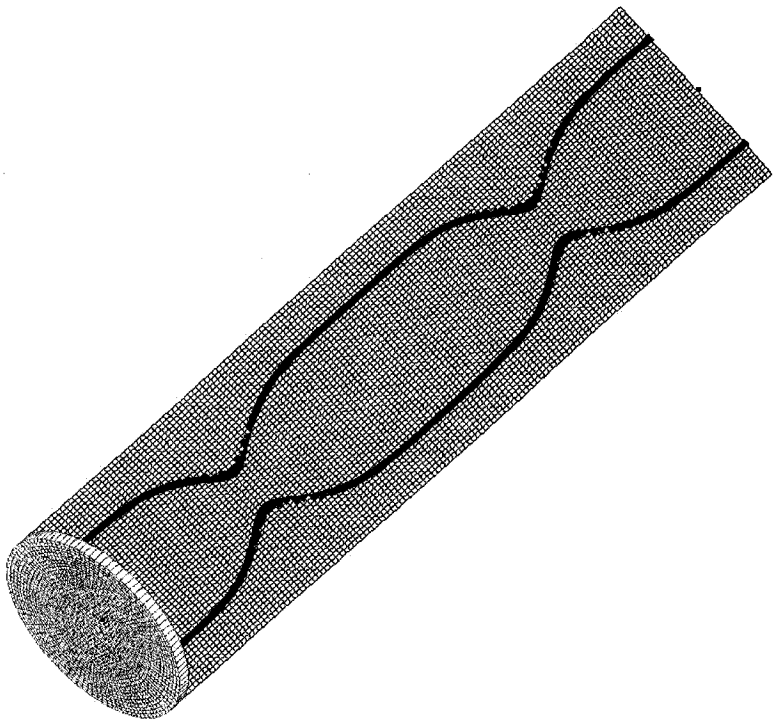

Figure 2.7 Example geometry of a serial pulmonary artery stenosis.

2.2.2 Vessel Model

The vessel's wall is modeled with Lagrangian brick elements with a constant stress solid element formulation. Most hydrocodes use one-point integration, resulting in all quantities except for the velocities being constant over an element [151]. In addition, the choice of one-point integration over fully integrated elements is justified because the latter tends to lock up in the constant volume bending modes for near incompressibility cases [155]. The tube wall is assumed to be elastic, homogeneous, isotropic and nearly incompressible. For this elastic material, the co-rotational rate of the deviatoric Cauchy stress tensor [155] is computed as:

$$S_{ij}^{\ n+1/2} = 2G\dot{\varepsilon}'^{\,n+1/2}_{ij} \tag{2.66}$$

and the pressure as:

$$p^{n+1} = -K \ln V^{n+1} \tag{2.67}$$

where G and K are the elastic shear and bulk moduli respectively, and V is the relative volume (i.e. the ratio of the current volume to the initial volume).

A Young's modulus of 10 *KPa* is selected, in agreement with values used in [168-170]. Near incompressibility is enforced with a Poisson's ratio of 0.45. The density of the structure is set to 1000 kg/m^3, matching in vitro experimental set-up data [132, 134, 143]. For boundary conditions, the inlet and outlet of the tube are restrained in the longitudinal direction. The external pressure is set to zero. Conceding that an elastic, homogeneous and isotropic vessel model is a very crude first approximation, it is nevertheless adopted for robustness of the solution. Given the numerical difficulties of coupling the non-linear Navier-Stokes equations for fluid behavior with a non-linear geometry of the vessel wall in the context of a moving interface, computational stability becomes a key concern. Additional simulations using Invariant-based hyperelastic models (e.g. Mooney-Rivlin, Odgen) and principal-stretch-ratio based strain-energy functions (e.g. Fung's exponential form [171]) were performed, but numerical instabilities were encountered at the onset for our considered three-dimensional geometries.

2.2.3 Fluid Model

The flow is assumed to be laminar, Newtonian, viscous and incompressible. A no-slip boundary condition is imposed, that is, the fluid in contact with the wall has zero velocity relative to the wall. Furthermore, no penetration of the fluid through the tube wall is allowed. A flow-reservoir attached to the inlet supplies the physiologically relevant flow rate boundary condition to the fluid domain. A fully developed flow with a paraboloidal Poiseuille distribution is assumed at the inlet. A magnetic-resonance-imaging velocity-mapping based curve for the main pulmonary artery is adapted from [172] (*Figure 2.8*). However, in our analysis, we will refer to its normalized (i.e. by maximum value applicable to both axes) counterpart for simplicity (*Figure 2.9*). The rational for this

approach is better control of the flow distribution and flow rate for consistent comparison between differing morphological configurations. An alternative is to drive the simulation with a pressure-reservoir based approach. However, this entails a cumbersome recalibration of the upstream and downstream pressure fields to maintain a given flow rate for each configuration. The fluid control volume surrounding the Lagrangian structure is assembled with Eulerian brick elements with the following element formulation: one-point integration with single material and void. For computational efficiency, one-point integration is preferred over a fully integrated element formulation. The computational time savings show up in the volume integration via Gaussian quadrature (i.e. numerical integration based on the Gauss rule, see e.g. [173]), and extends to strain, stress and element nodal force calculations [155]. The major drawback of one-point integration is the possibility of oscillatory hourglass (zero-energy) modes with much shorter periods than the structure response. However, these modes may be stabilized with the use of hourglass viscosity (i.e. viscous damping capable of stopping the formation of anomalous modes but having a negligible effect on the stable global modes) [151]. In addition, the Eulerian fluid elements are linked to the Gruneisen equation of state [155], which defines pressure for compressed material as:

$$p = \frac{\rho_0 C^2 \mu \left[1 + \left(1 - \frac{\gamma_0}{2} \right) \mu - \frac{\alpha_0}{2} \mu^2 \right]}{\left[1 - (S_1 - 1)\mu - S_2 \frac{\mu^2}{\mu + 1} - S_3 \frac{\mu^3}{(\mu + 1)^2} \right]} + (\gamma_0 + \alpha_0 \mu) E \quad (2.68)$$

where E is the internal energy per initial volume, C is the intercept of the shock velocity (see e.g. [155, 174]) vs particle velocity curve, S_1, S_2, S_3 are the coefficients of the slope of this curve, γ_0 is the Gruneisen gamma, and α_0 is the first-order volume correction to γ_0. The compression is defined in terms of the relative volume, V, as:

$$\mu = \frac{1}{V} - 1 \quad (2.69)$$

For expanded materials, the pressure is defined by:

$$p = \rho_0 C^2 \mu + (\gamma_0 + \alpha_0 \mu) E \tag{2.70}$$

For practical reasons, most in vitro experimental set-ups use water or a water based mixture as the working fluid. The Gruneisen parameters for water are provided by [174]. The density of the fluid is set to 1000 kg/m^3. Water is chosen in this simulation in view of facilitating possible future experimental validation of our results. This is done so despite the fact that blood is approximately four times more viscous than water, under the Newtonian approximation [84]. However, the lowered viscosity effect of water is somewhat compensated by the reduced opposition to flow from the steady resistive term in the pulmonary circulation, at about one-sixth of the systemic vascular resistance [3].

After disclosing the merits and drawbacks of the inherent assumptions of our model, we are now ready to proceed to the next chapter, the discussion of our numerical results.

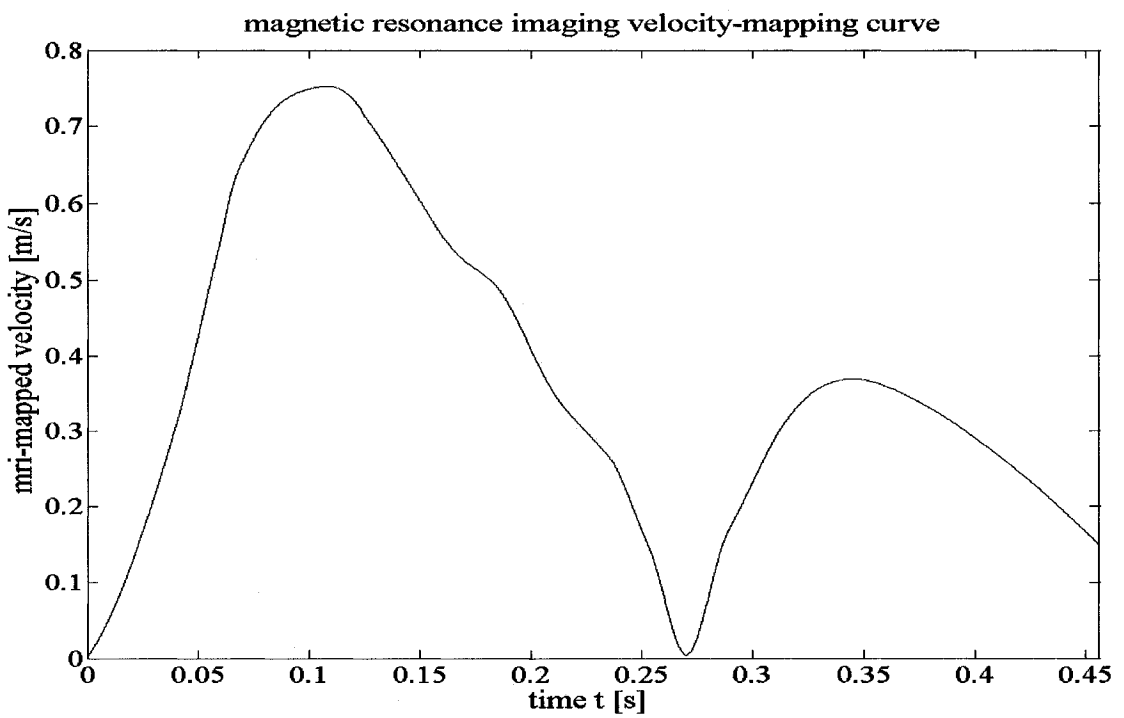

Figure 2.8 Magnetic resonance imaging velocity mapping curve, adapted from [172].

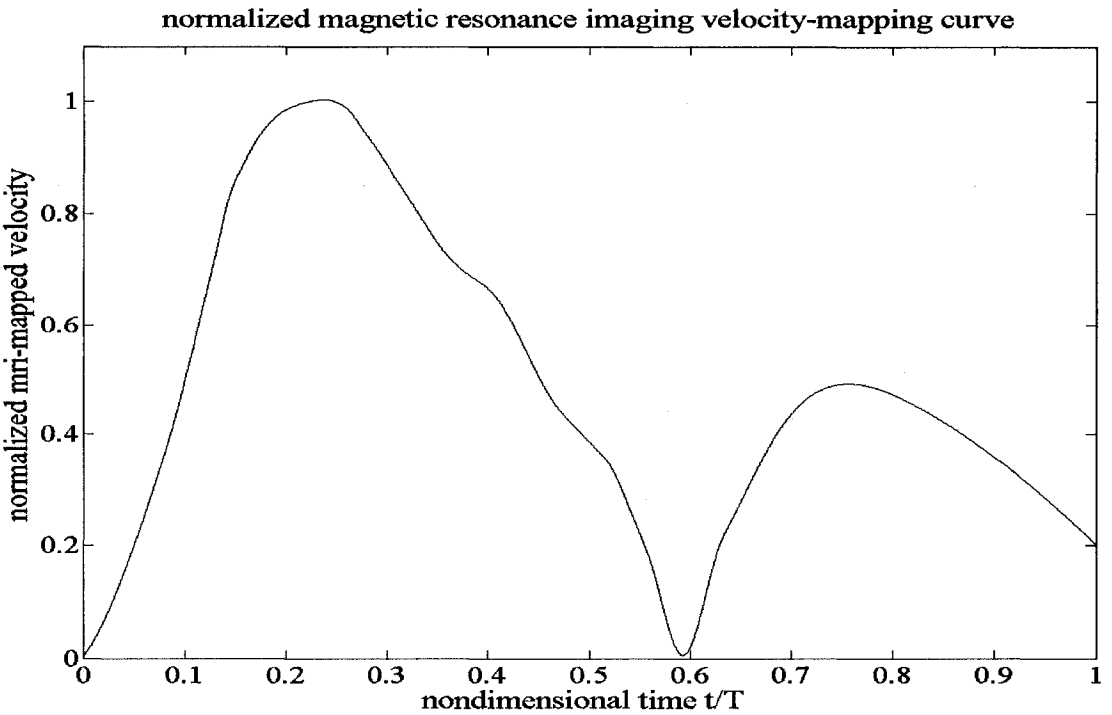

Figure 2.9 Normalized magnetic resonance imaging velocity mapping curve, adapted from [172].

Chapter 3.

Numerical Results

This chapter presents the main findings of our work in two main sections: three-dimensional wall deformation and three-dimensional velocity field. The former focuses on the temporal evolution of wall displacement, on quantifying wall collapse, and on some observations of wall displacement. The latter begins with a brief review on three-dimensional flow field in stenotic vessels, and is followed by a discussion on the effect of length and of angular orientation on the flow field.

3.1 Three-Dimensional Wall Deformation

3.1.1 Temporal Evolution of Wall Displacement

The mechanisms causing collapse at the downstream side of a straight compliant tube has been previously described in detail. Succinctly, a non-zero volume flux creates a viscous pressure drop in the fluid and thereby increases the compressive loads on the tube wall in the flow direction [124]. In other words, compressive loads and deformation on the tube wall increase with the axial distance from the upstream end. For a straight tube, the corresponding deformation reduces the tube's cross-sectional area, which increases the pressure drop even further. There exists a threshold of volume flux at which the critical value of compressive load is exceeded. Then, the tube's deformation becomes unstable. Buckling would be initiated at the downstream end, where the compressive loads possess the largest values. The increase in pressure drop, induced by the buckling, will then increase the compressive loads on the downstream end and accelerate the collapse [175]. Once the tube buckles, its resistance increases so rapidly that any further increase in the pressure drop may potentially reduce the volume flux through the tube, leading to flow limitation. The asymmetry of the fluid traction increases with the tube's collapse, driving the point of strongest collapse more downstream [122]. The distended upstream part of

the tube merely acts as a support for the downstream part which is under compression [124].

In addition to the viscous dissipation, flow through a stenotic vessel involves flow separation downstream of the throat. The extra dissipation may be the necessary ingredients to allow for the development of self-excited oscillations in collapsible tubes, a mechanism proposed by [176]. A three-dimensional study of a steady flow in collapsible tubes shows that fluid dissipation is greatest near the wall in the region of strongest collapse [177]. Moreover, eccentric stenosis may lead to asymmetric flow where the high velocity jets impinge on the sidewall. The location near the point of jet impingement on the sidewall would induce significant dissipation, particularly if it has buckled inwards. The aforementioned locations of additional dissipation result in a higher pressure drop for a flow through a stenotic vessel, than in a straight compliant tube. Thus, the presence of each additional stenosis may enhance the hazards of buckling to a differing degree, depending on their relative spatial locations and orientations. The above evidence suggests that flow through a stenotic vessel may lower the critical volume flux compared with a straight compliant tube, for the onset of the flow-induced buckling. As a check, we conducted additional simulation with straight tube of similar dimensions, which revealed that collapse does not materialize for the prescribed physiological volume flux used in our computations (*Figure 3.1*). The small-amplitude axisymmetric deformation validates a known fact for a straight tube: fluid pressure distribution have a weak effect on the wall motion, which is dominated by the spatially constant external pressures [122]. This gives us confidence that wall motion in our simulations is driven by the ongoing strong coupling and interaction between the non-linear vessel geometries, and their corresponding asymmetric flow. It leads us to assert that under these conditions, fluid pressure distribution have substantial implication for wall motion. This statement brings us to a closer qualitative visual inspection of the effect of spatial configuration on wall motion for the five cases considered in our study. For each case, we show the initial vessel geometry, along with a few selected time steps taken from the diastole phase, and finally, the last time step (see e.g. case 1 (*Figures 3.2-3.6*), case 2 (*Figures 3.7-3.11*), case 3 (*Figures 3.12-3.16*), case 4 (*Figures 3.17-3.21*), case 5 (*Figures 3.22-3.26*)).

The examination of these figures leads us to believe that there exists a close relationship between the angular orientation of the distal stenosis (i.e. the constriction direction) and the direction of wall motion at the downstream end (e.g. see *Figures 3.6, 3.11, 3.16, 3.21 & 3.26*).

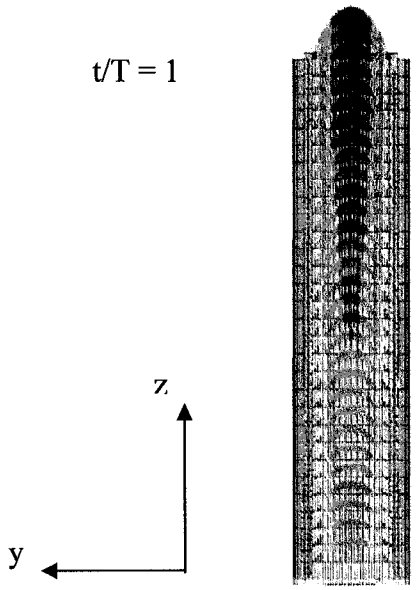

Figure 3.1 Fluid structure interaction simulation for a straight tube.

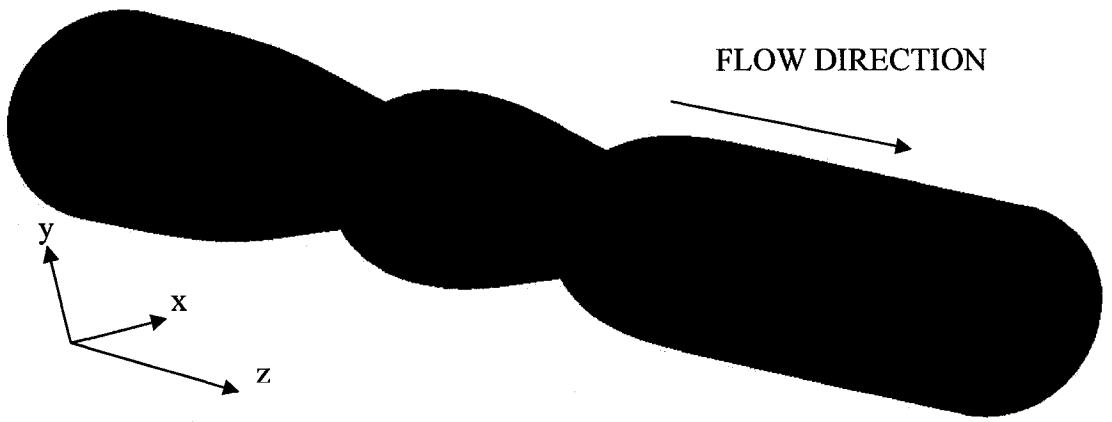

Figure 3.2 Case 1: wall deformation at t/T = 0.

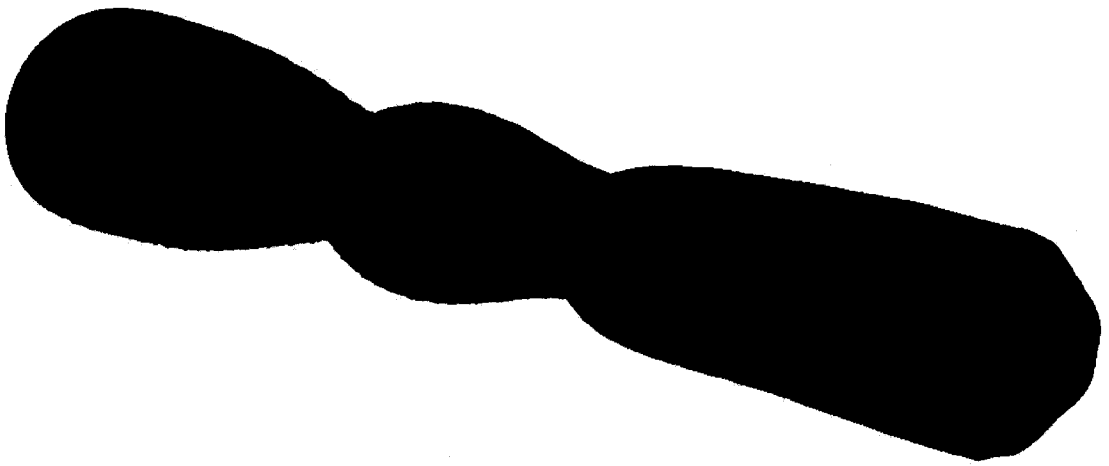

Figure 3.3 Case 1: wall deformation at t/T = 0.70.

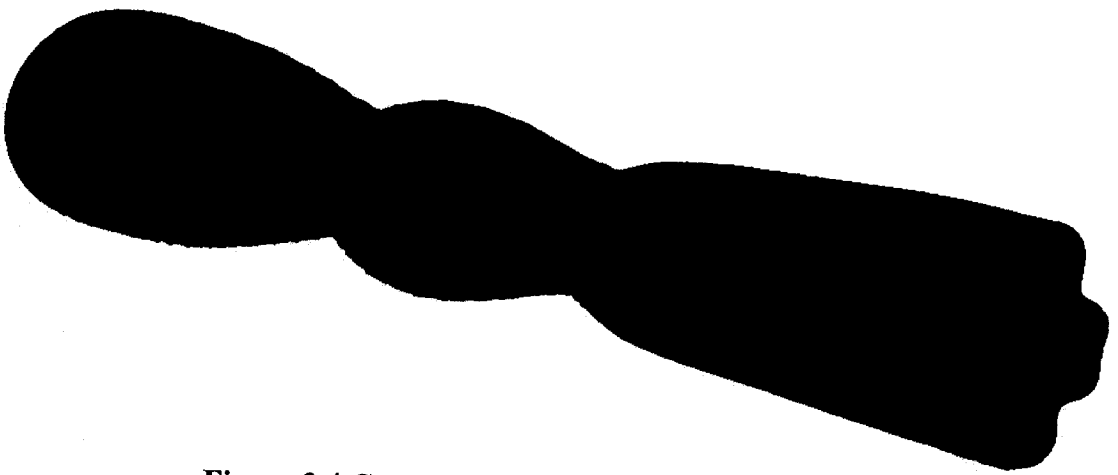

Figure 3.4 Case 1: wall deformation at t/T = 0.81.

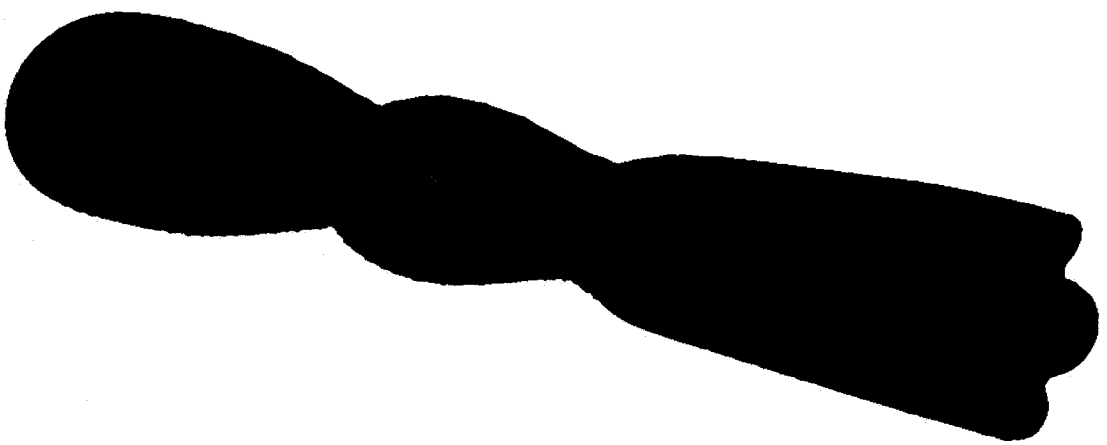

Figure 3.5 Case 1: wall deformation at t/T = 0.92.

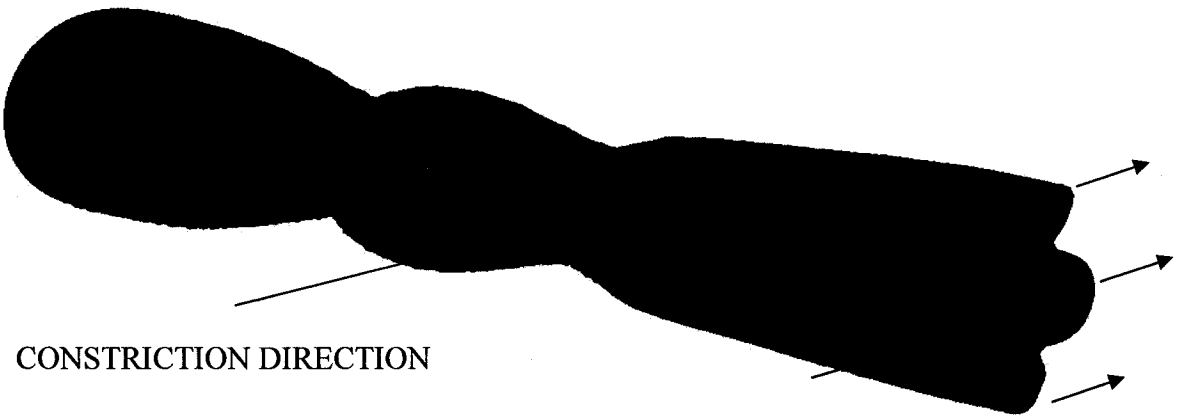

Figure 3.6 Case 1: wall deformation at t/T = 1.

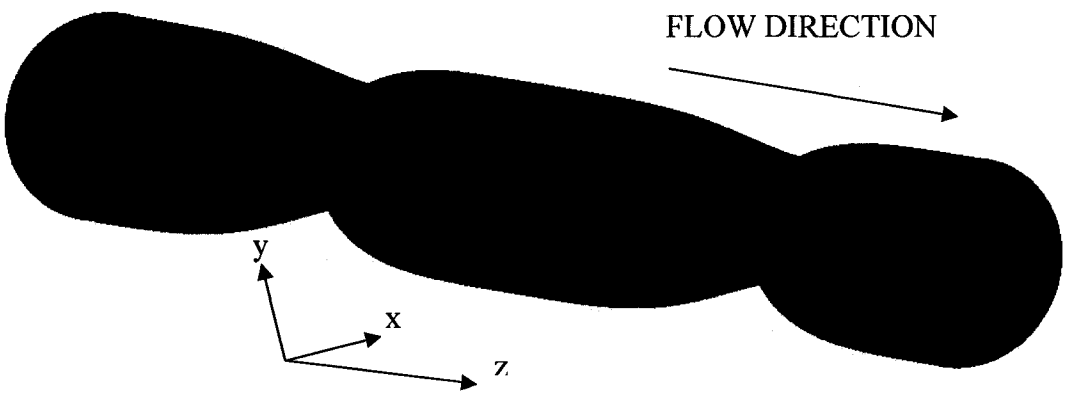

Figure 3.7 Case 2: wall deformation at t/T = 0.

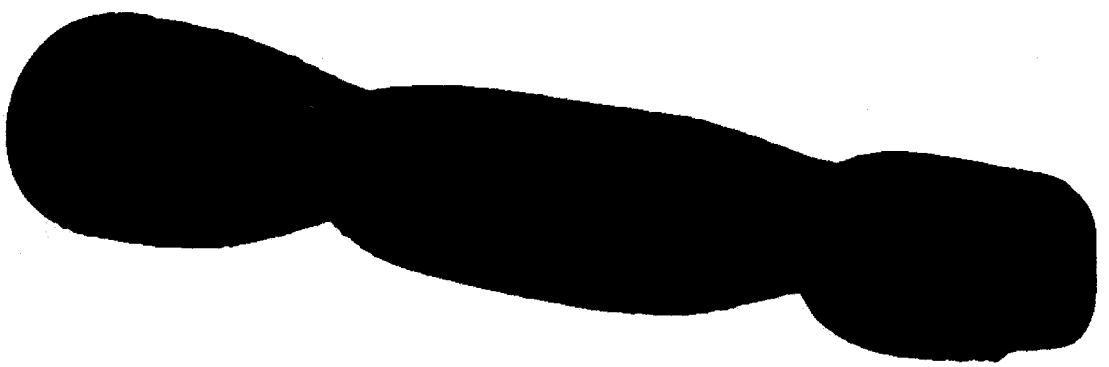

Figure 3.8 Case 2: wall deformation at t/T = 0.71.

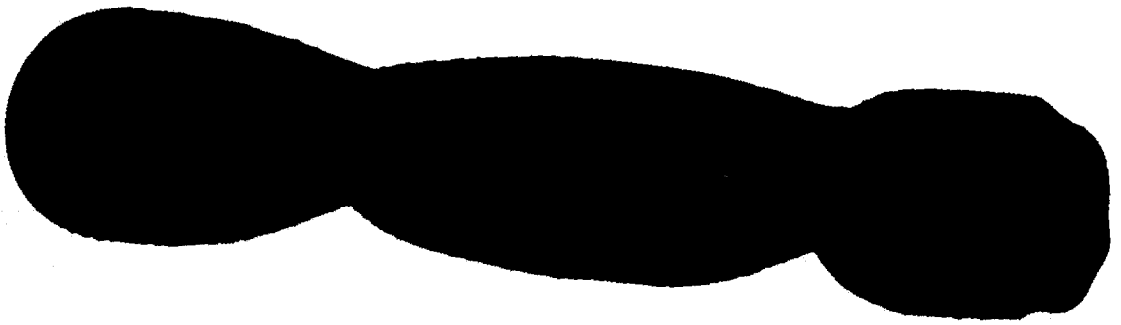

Figure 3.9 Case 2: wall deformation at t/T = 0.80.

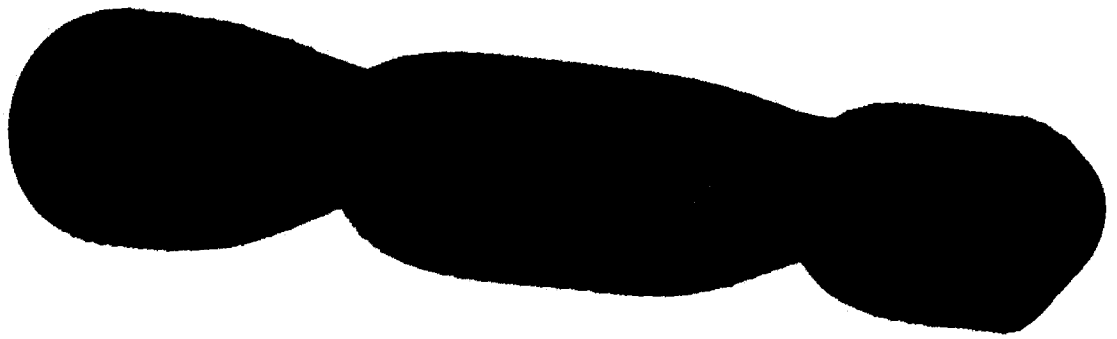

Figure 3.10 Case 2: wall deformation at t/T = 0.91.

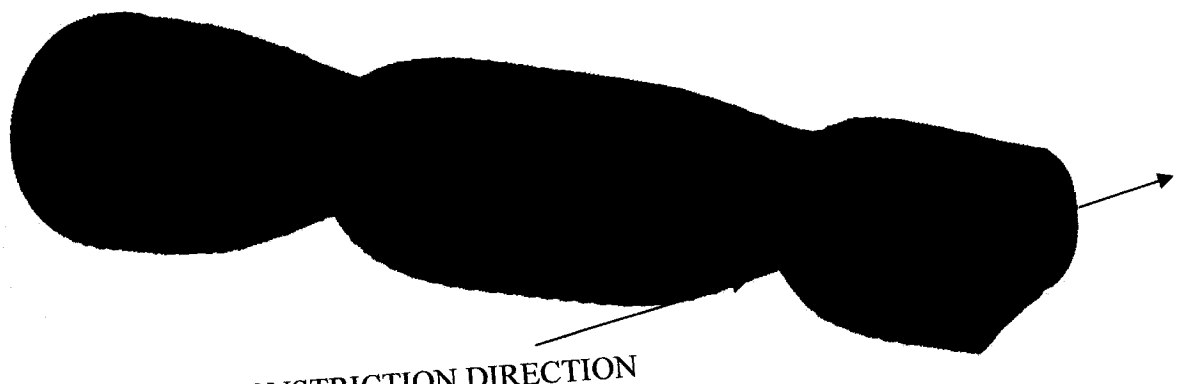

Figure 3.11 Case 2: wall deformation at t/T = 1.

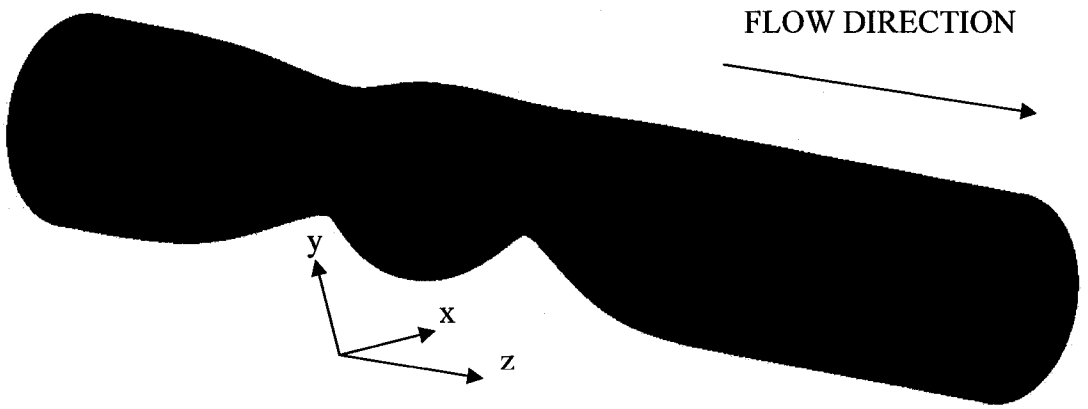

Figure 3.12 Case 3: wall deformation at t/T = 0.

Figure 3.13 Case 3: wall deformation at t/T = 0.70.

Figure 3.14 Case 3: wall deformation at t/T = 0.79.

Figure 3.15 Case 3: wall deformation at t/T = 0.91.

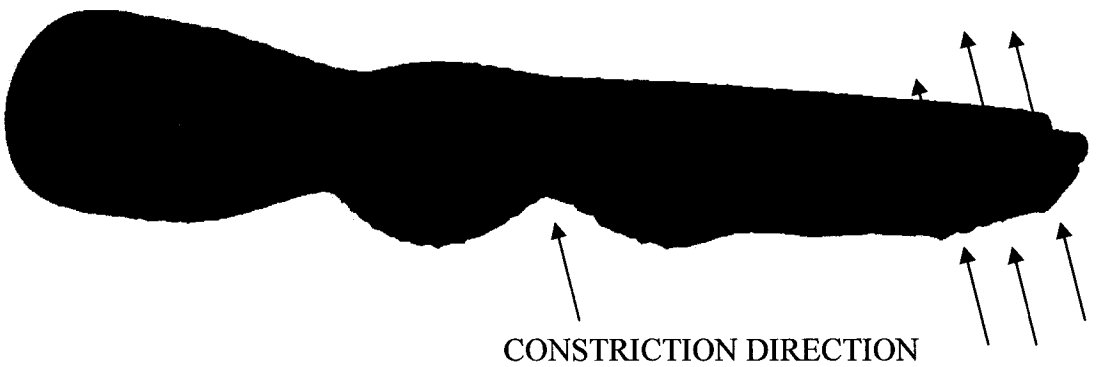

Figure 3.16 Case 3: wall deformation at t/T = 1.

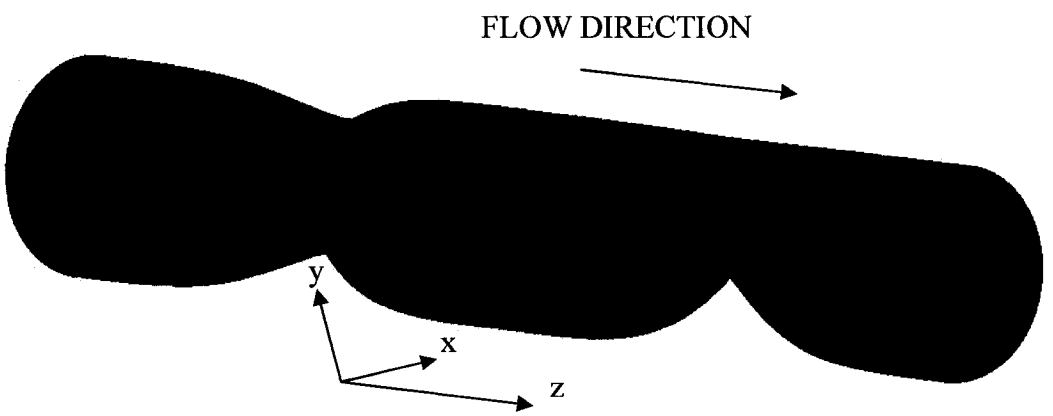

Figure 3.17 Case 4: wall deformation at t/T = 0.

Figure 3.18 Case 4: wall deformation at t/T = 0.71.

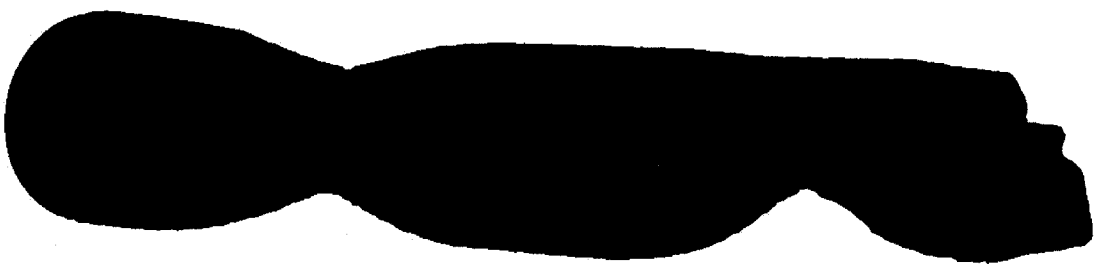

Figure 3.19 Case 4: wall deformation at t/T = 0.80.

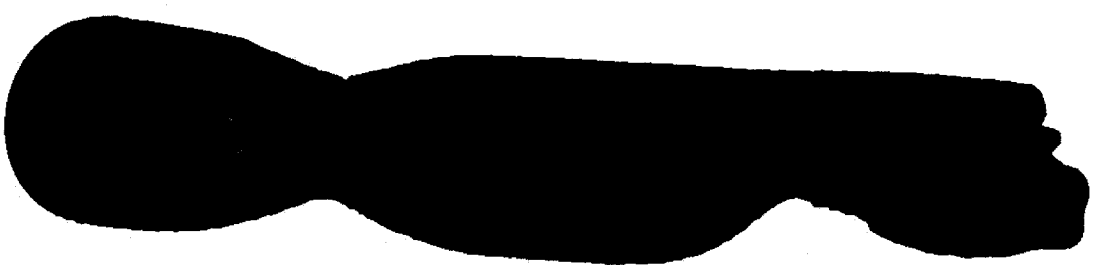

Figure 3.20 Case 4: wall deformation at t/T = 0.91.

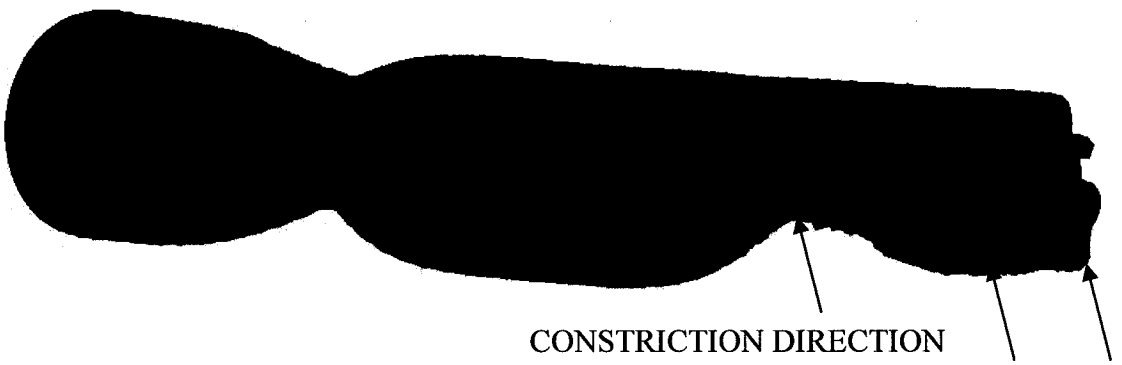

Figure 3.21 Case 4: wall deformation at t/T = 1.

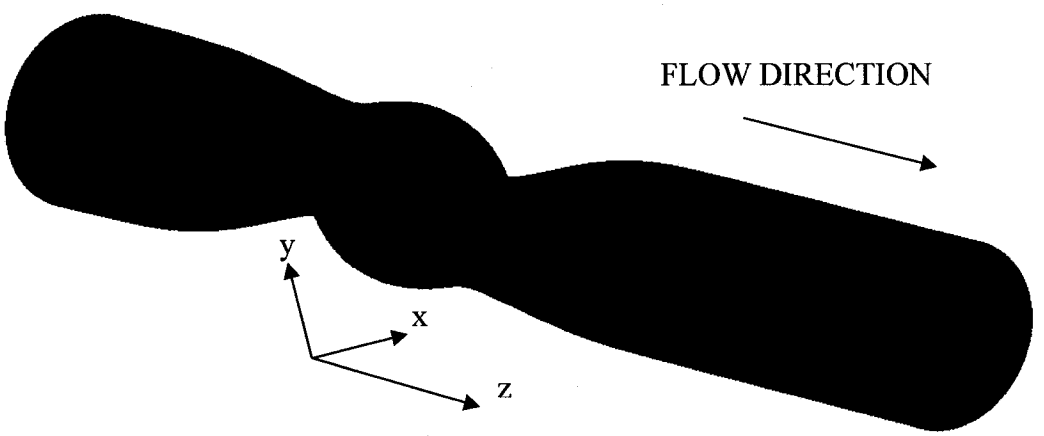

Figure 3.22 Case 5: wall deformation at t/T = 0.

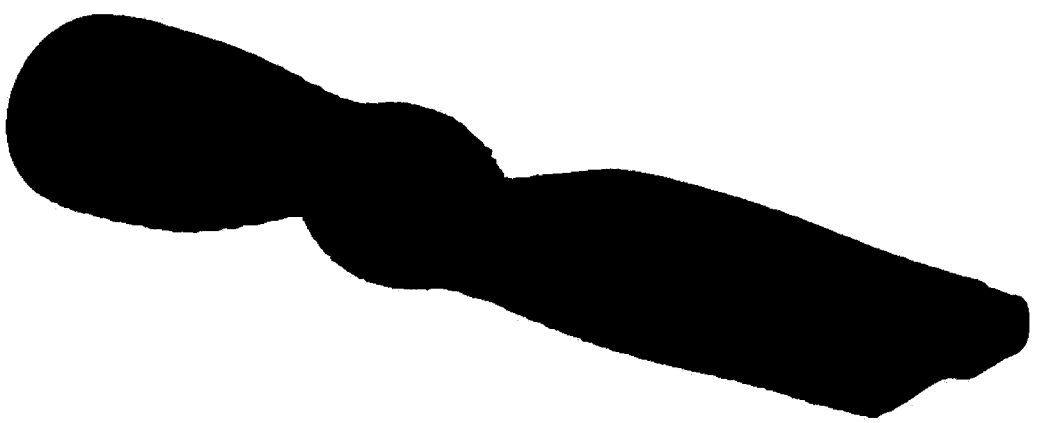

Figure 3.23 Case 5: wall deformation at t/T = 0.71.

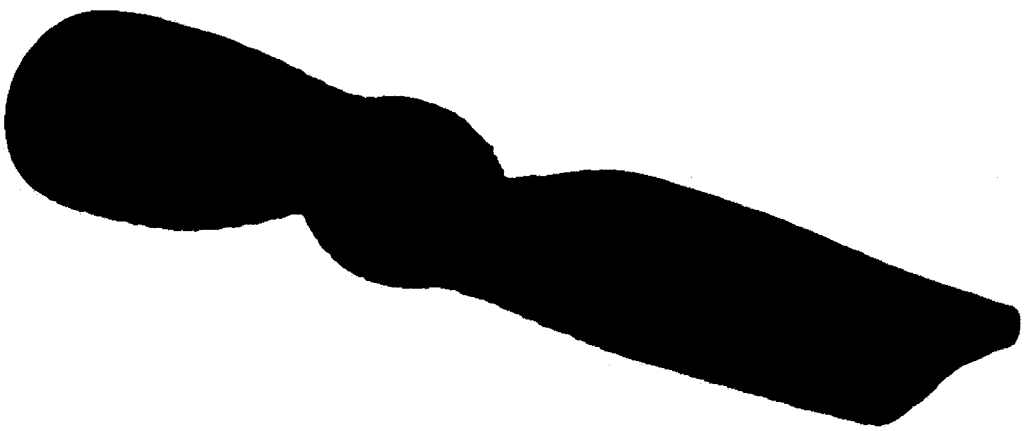

Figure 3.24 Case 5: wall deformation at t/T = 0.80.

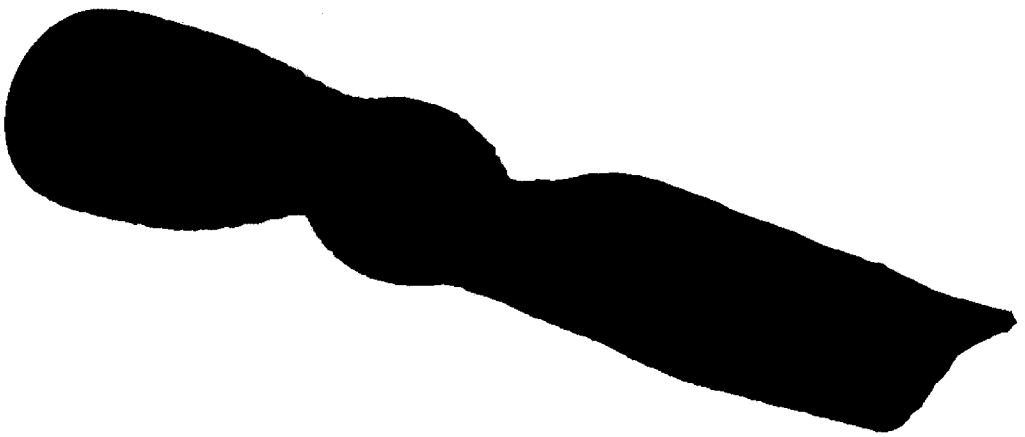

Figure 3.25 Case 5: wall deformation at t/T = 0.92.

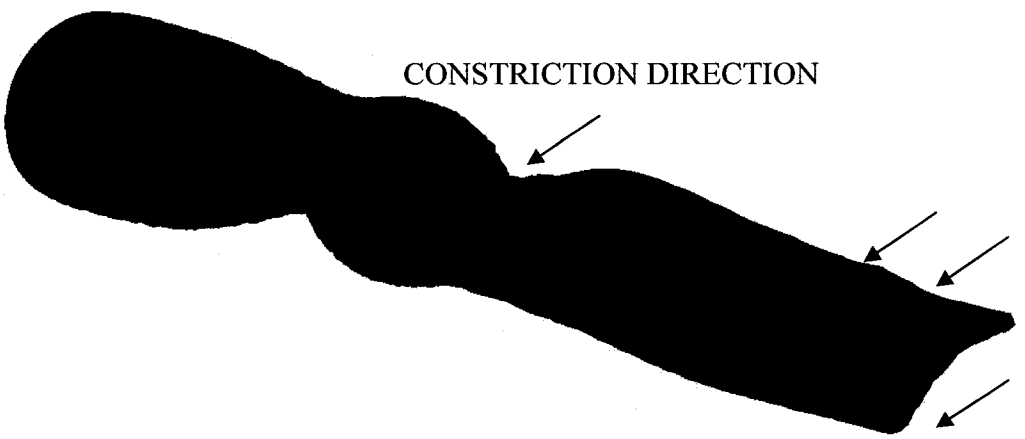

Figure 3.26 Case 5: wall deformation at t/T = 1.

3.1.2 Quantifying Wall Collapse

Our qualitative visual observations seem to suggest that there exists a close link between the angular orientation of the distal stenosis and the direction of wall motion at the downstream end. We shall utilize this apparent relationship to devise a simple metric for consistent comparison across all the cases. Our metric will serve as a proxy to measure wall collapse. We argue that the angular orientation of the distal stenosis is likely to have significant influence on the downstream wall behavior because its throat offers the path of least fluid resistance. Therefore, the flow will tend to evolve towards the Poiseuille flow in the direction set by the angular orientation of the distal stenosis. The large wall slope past the throat creates large adverse pressure gradient, causing the viscous layer to expand on the constricted side. This has the effect of drawing the core flow closer to the straight side. The strong coupling and interaction between fluid and structure lead us to believe that the predominant wall motion may be correlated with the direction in which the core flow evolves towards the ideal Poiseuille flow.

In view of this, our metric will measure the change in length from the initial vessel's geometries in each of the two principal directions of constriction of the distal stenosis (*Figure 3.27*). The concept behind our methodology is to filter out the disturbances or fluctuation signals. We seek the extreme and median values of change in length throughout the cycle (the median is a more robust estimate of the center than an average, since outliers have little effect on it). We then plot the results as error bars; assuming that the median value is the center of the sample, we treat the maximum and minimum values as the respective upper and lower deviations. As such, we construe any significant asymmetry in the distance between the median and the extreme values as a strong indication of wall collapse in a preferential direction. To investigate the effect of length on wall collapse, we will sample the cross-sectional planes shown in *Figures 3.28 & 3.29*. We shall employ the same approach to assess the impact of angular orientation on wall collapse.

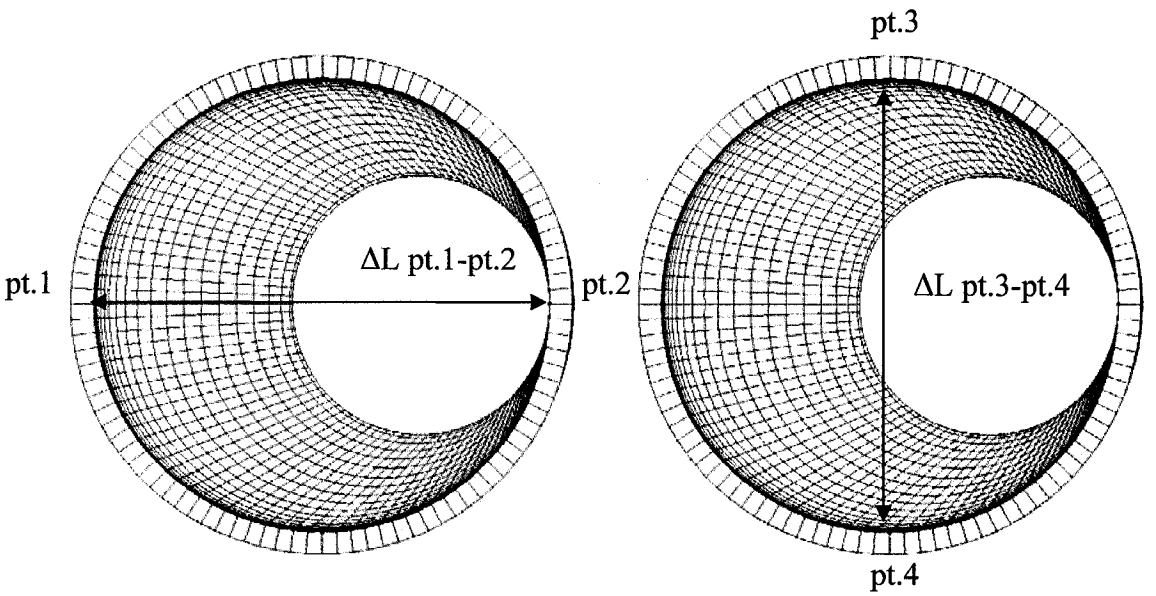

Figure 3.27 Metrics: change in length (ΔL): pt.1-pt.2 (left), pt.3-pt.4 (right).

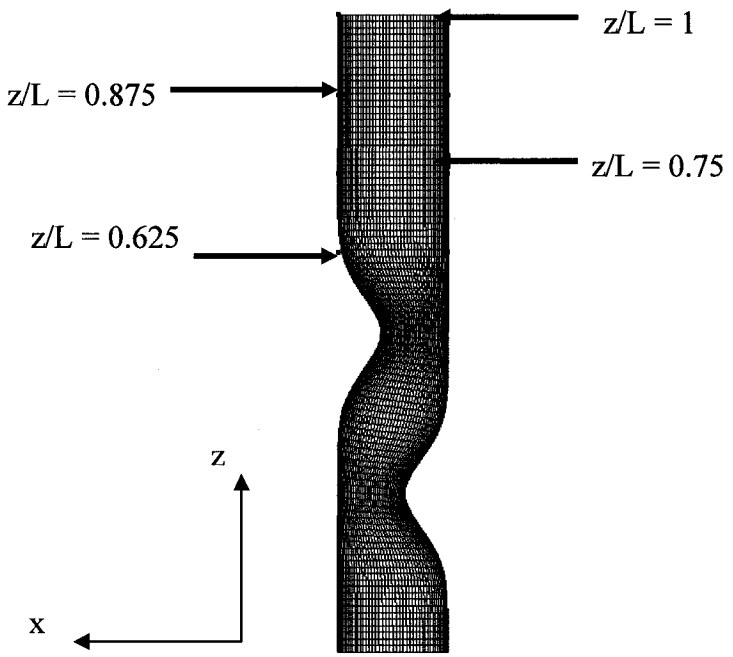

Figure 3.28 Sample cross-sectional planes: for cases (1, 3 & 5) where the distance between stenoses is 25% of tube length L (1.667 x D).

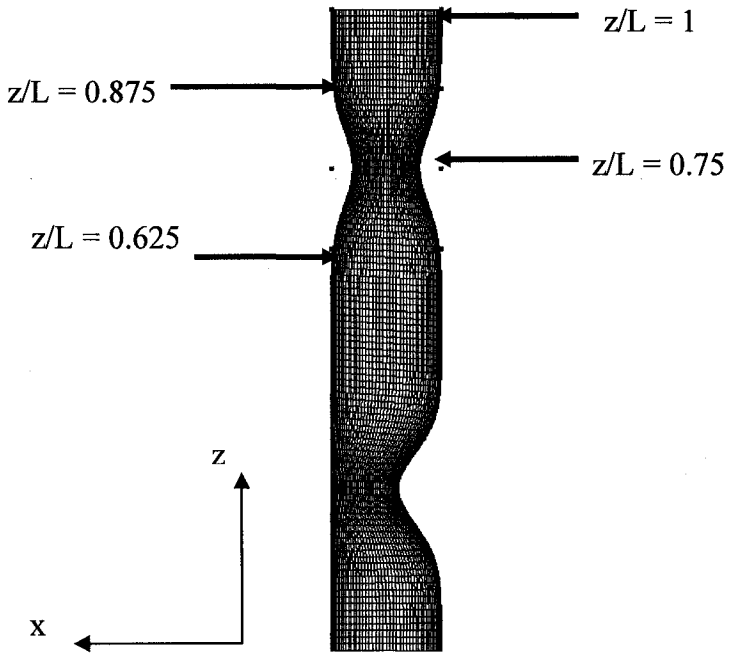

Figure 3.29 Sample cross-sectional planes: for cases (2 & 4) where the distance between stenoses is 50% of tube length L (3.333 x D).

3.1.2.1 Effect of Length on Wall Collapse

The results for all the cases according to the methodology as proposed in the previous section are displayed in the following figures (see e.g. case 1 (*Figures 3.30 & 3.31*), case 2 (*Figures 3.32 & 3.33*), case 3 (*Figures 3.34 & 3.35*), case 4 (*Figures 3.36 & 3.37*), case 5 (*Figures 3.38 & 3.39*)).

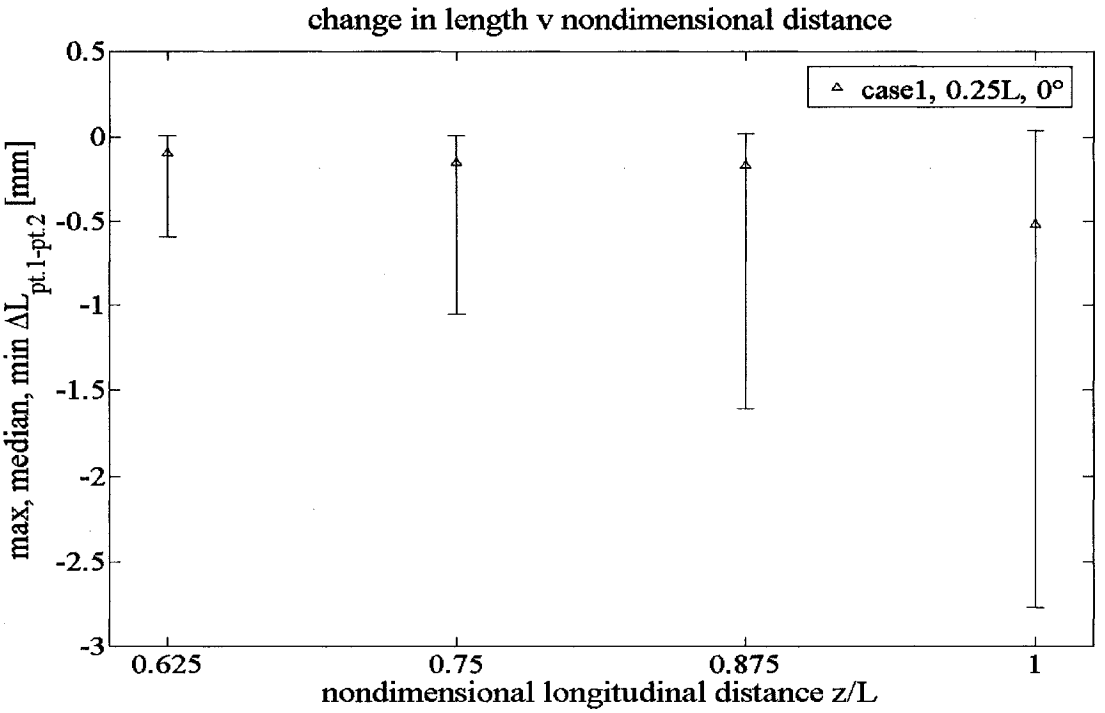

Figure 3.30 Case 1: effect of length on wall collapse, ΔL pt.1-pt.2.

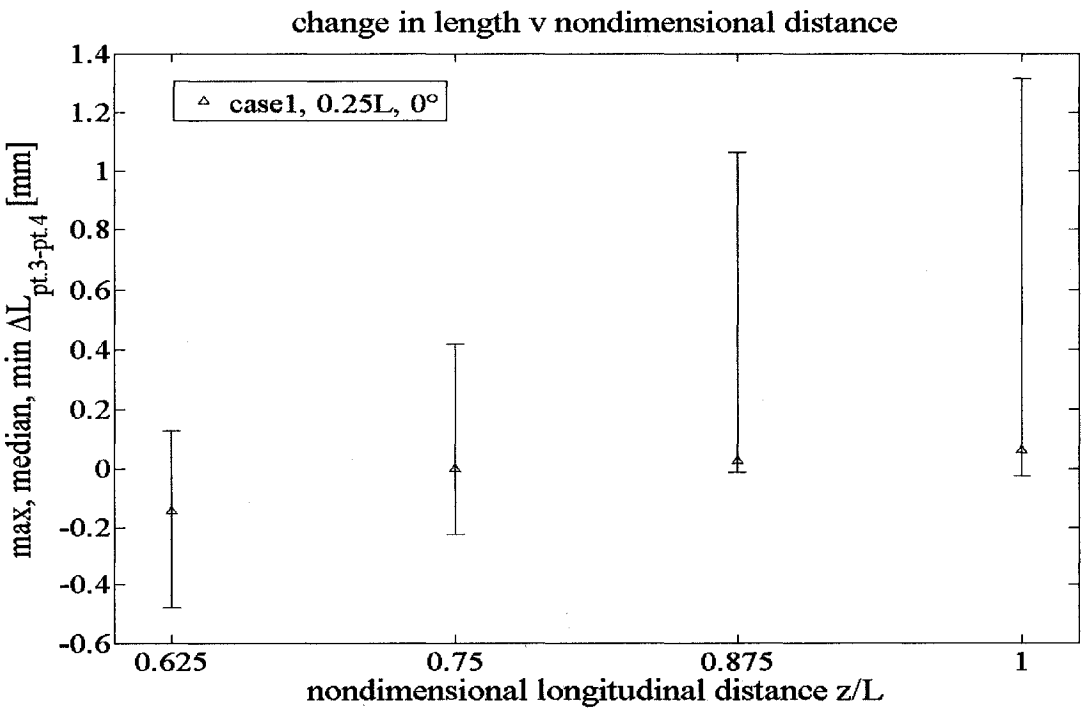

Figure 3.31 Case 1: effect of length on wall collapse, ΔL pt.3-pt.4.

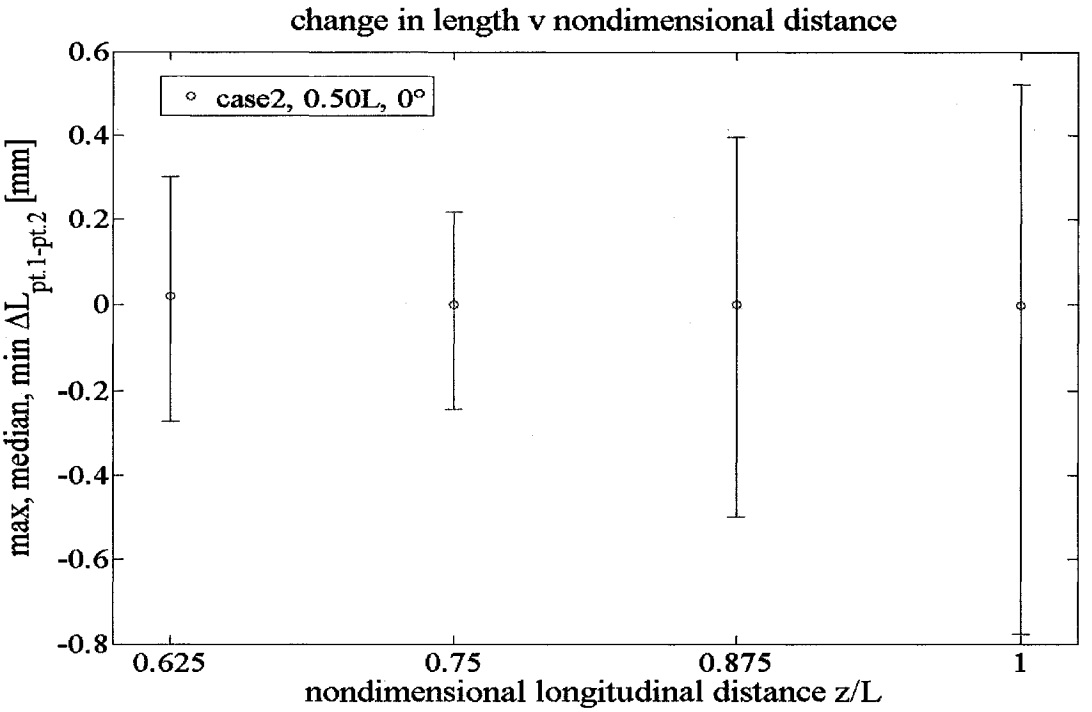

Figure 3.32 Case 2: effect of length on wall collapse, ΔL pt.1-pt.2.

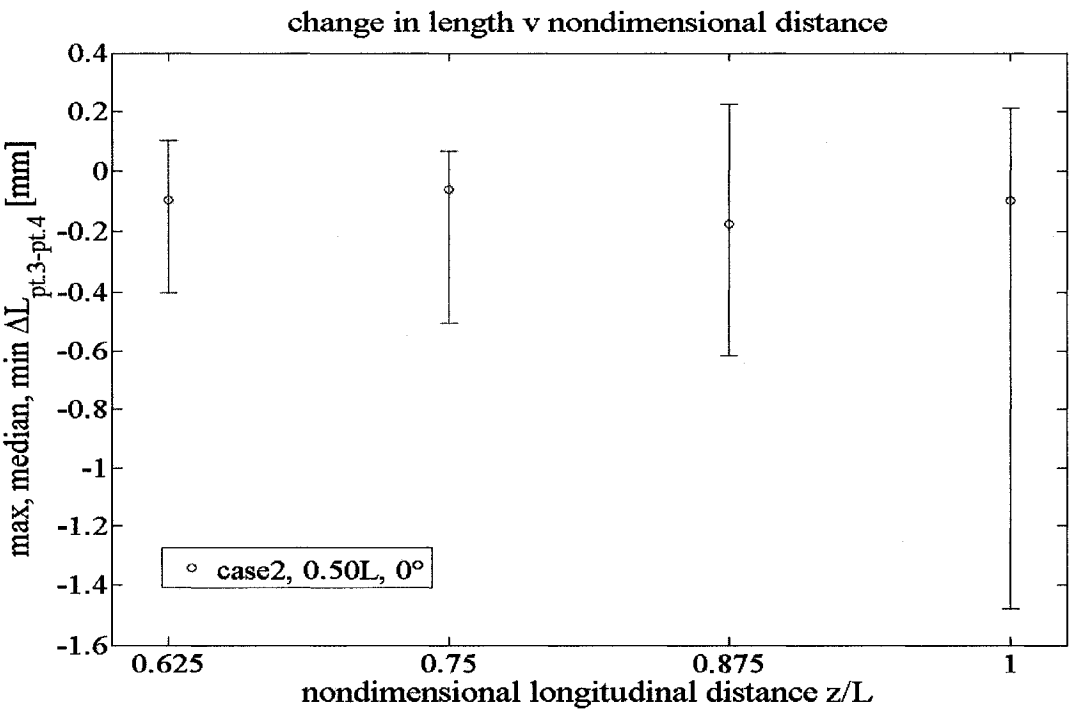

Figure 3.33 Case 2: effect of length on wall collapse, ΔL pt.3-pt.4.

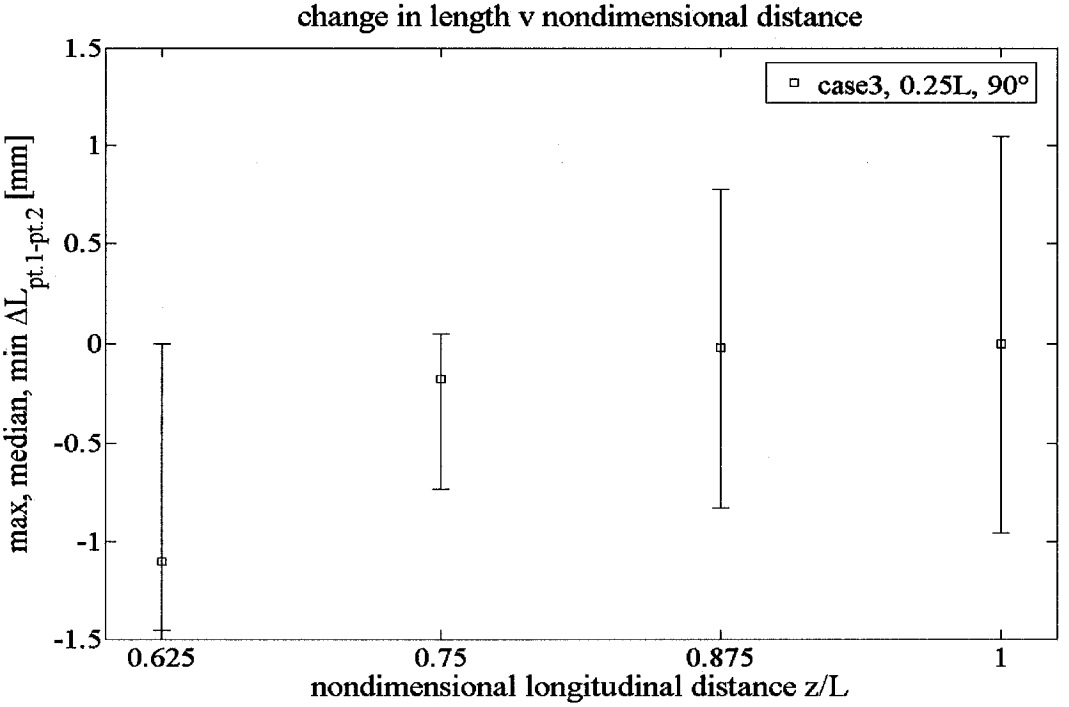

Figure 3.34 Case 3: effect of length on wall collapse, ΔL pt.1-pt.2.

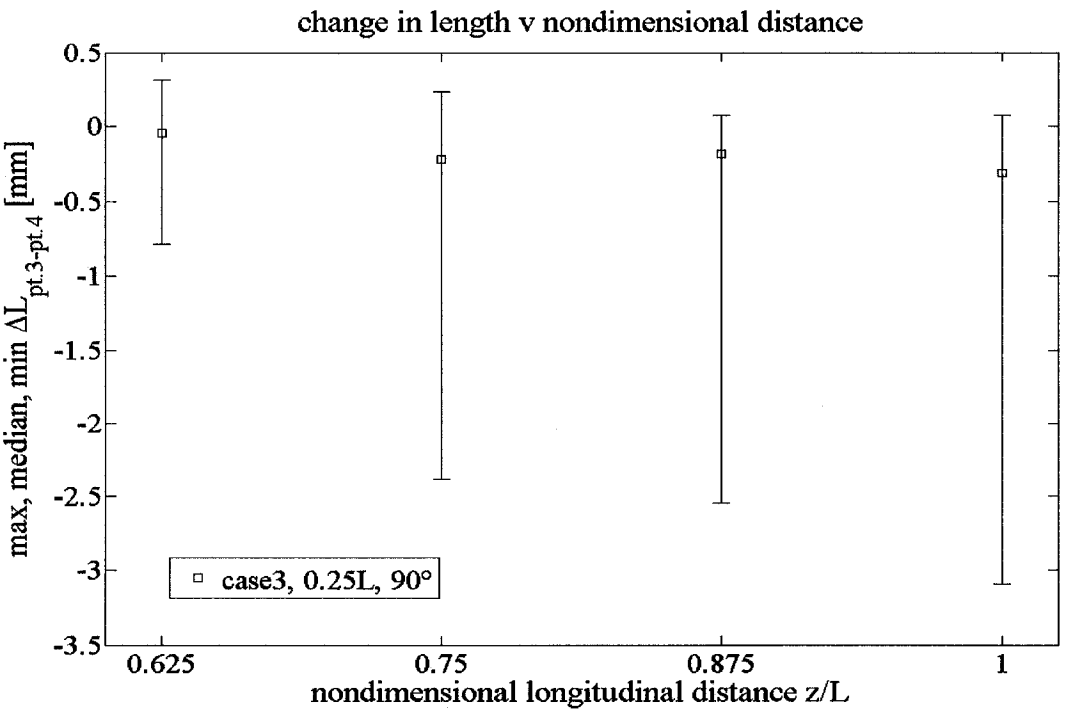

Figure 3.35 Case 3: effect of length on wall collapse, ΔL pt.3-pt.4.

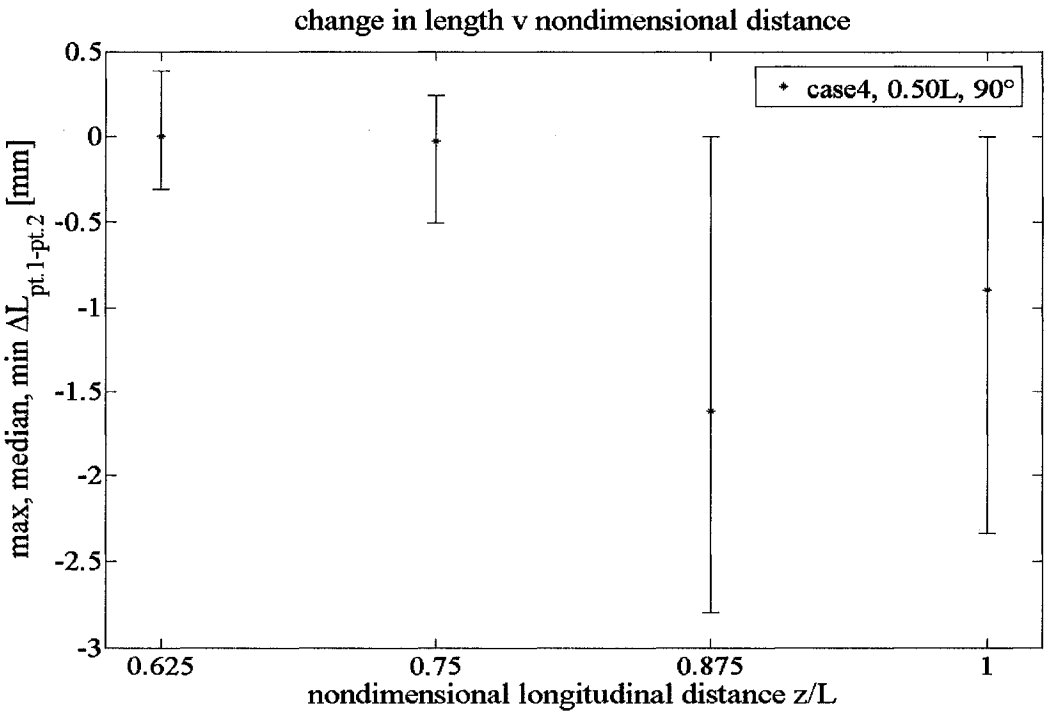

Figure 3.36 Case 4: effect of length on wall collapse, ΔL pt.1-pt.2.

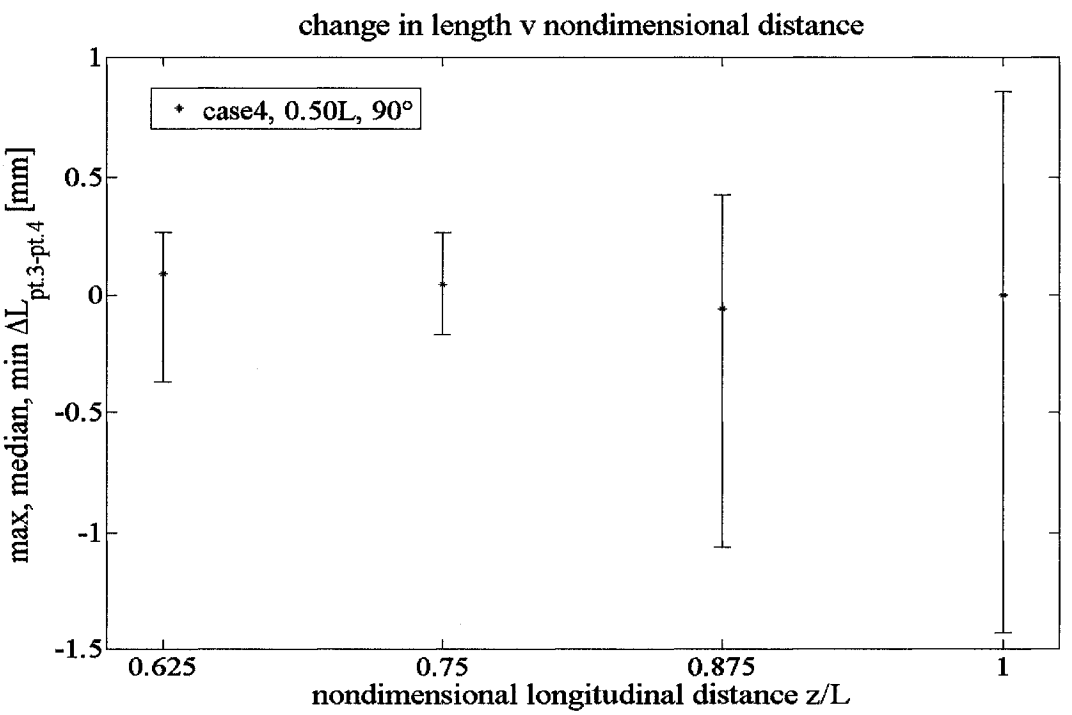

Figure 3.37 Case 4: effect of length on wall collapse, ΔL pt.3-pt.4.

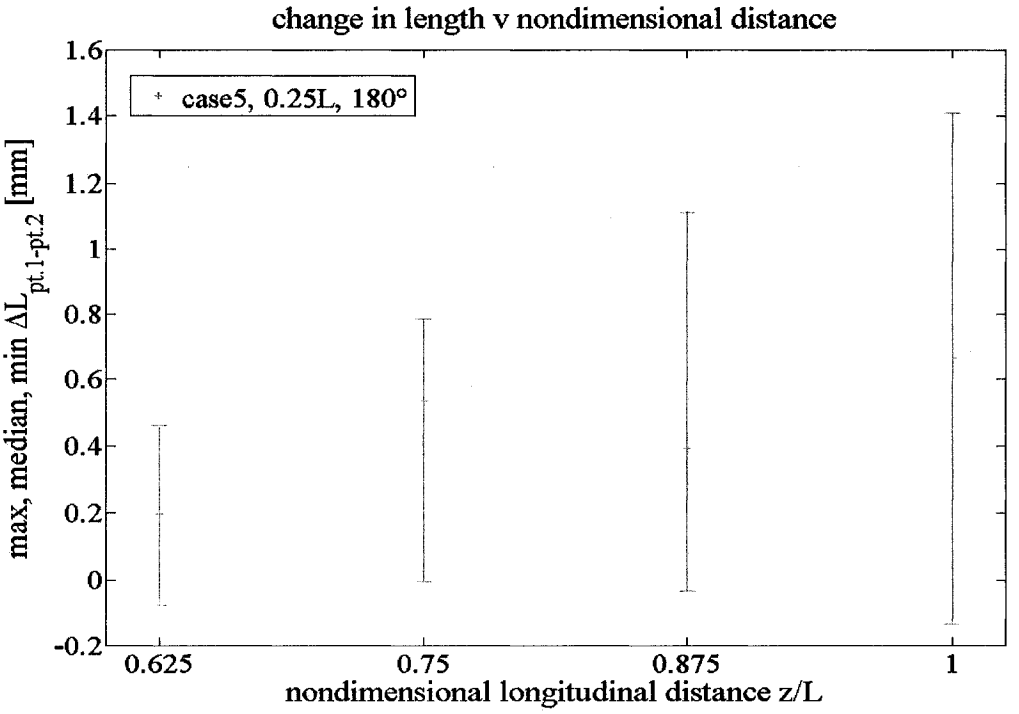

Figure 3.38 Case 5: effect of length on wall collapse, ΔL pt.1-pt.2.

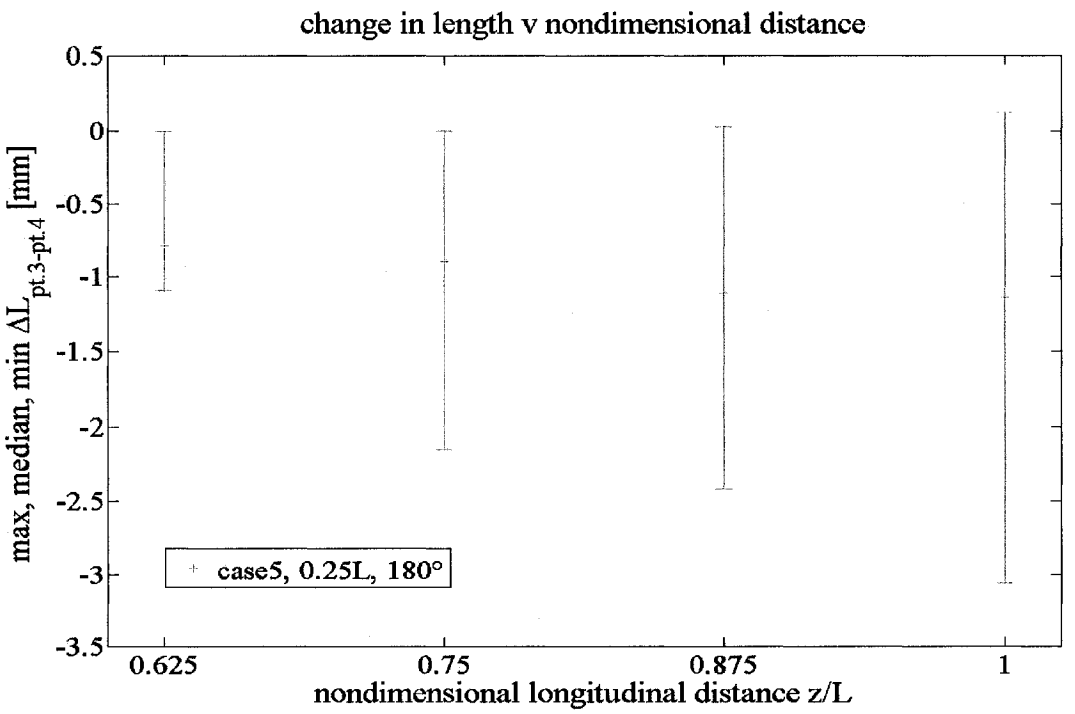

Figure 3.39 Case 5: effect of length on wall collapse, ΔL pt.3-pt.4.

We have previously stressed in *section 3.1.1* that for a compliant tube, the compressive loads and deformation on the wall increase with the axial distance from the upstream end, in the flow direction. The increase in wall deformation (i.e. contraction or extension) manifests itself in our results for all cases, as shown by the lengthening of the bars (i.e. distance between the extreme values) as we progress towards the outlet. We have also underlined that the throat of the stenosis does not collapse easily because of its thicker wall and smaller diameter than elsewhere in the tube. For cases (2 & 4), this is revealed by the fact that the bars are narrowest at the location of the throat (i.e. $z/L = 0.75$ tick). Since these two physical requirements are reflected in the results, this increases our confidence level in both the fluid structure interaction model and our conceived methodology to quantify the degree of wall collapse.

One trend we notice in these plots is the strong influence of the closeness between the stenoses on wall motion at the downstream end. For all cases, this is illustrated by the increasing width of the bars as we move closer to the outlet. Furthermore, a noteworthy observation is that significant contraction in one direction may lead to extension in the perpendicular direction. In case 1 for example, the change in length between pt.1 & pt.2 decreases and that between pt.3 & pt.4 increases, while the opposite is true for case 3. The fact that the contraction seems to be predominantly aligned in the direction of the constriction suggests an important role of the initial angular orientation of the distal stenosis on the subsequent wall motion at the downstream end. We shall explore this idea in greater detail in the next section. For now, we highlight the strong asymmetry, with the median skewed towards an extreme value, for cases (1 & 3). We interpret a significant distance of departure of an extreme value from the median as a strong indication of preferential direction of wall collapse. By this measure, case 1 is most susceptible to wall contraction in the pt.1 & pt.2 direction, while case 3 is most vulnerable in the pt.3 & pt.4 direction. This yardstick also reveals that case 1 is most likely to undergo to wall extension in the pt.3 & pt.4 direction. These are consistent with our visual inspection from *section 3.1.1*. For cases (2 & 4), the fact that the median lies at approximately midway between the extreme values suggest that these configurations are not likely to experience wall motion in any preferential direction. This suggests that positioning the

distal stenosis closer to the outlet tends to diminish the influence of its initial angular orientation. This physically makes sense since wall motion in the proximity of the throat will somehow be dampened by its stiffness.

Case 5 is particular in the sense that wall osculation has occurred, as shown in *Figures 3.25 & 3.26*. It also brings to light a limitation of our primitive comparison tool, which is highly sensitive to the choice of sampling points. For case 5, our metrics would have revealed an alternative scenario had we selected different sampling points, for instance, at the location where the opposite-wall contact occurs. The most we can say is that our metric is unsuited to assess the behavior for cases where wall contact has occurred, or involving highly distorted shapes. Nevertheless, it is surprisingly predictive and satisfactory for cases where there exists a predominant direction or pattern of wall motion, as shown by cases (1 & 3). Despite its simplicity, it is also relatively successful for revealing cases where the wall motion lacks any preferential direction, such as in cases (2 & 4).

3.1.2.2 Effect of Angular Orientation on Wall Collapse

We shall be succinct for this section, since we are relying on the same methodology as in the previous section. The key difference is that we will present the results in terms of the angular offset between the stenoses instead of the length. Note that the angular offset is equivalent to the absolute angular orientation of the distal stenosis, as measured from the reference x-axis. This exercise of displaying the data from an alternative viewpoint will serve to reinforce our previous observations. The results may be found in the following figures, see e.g. (*Figures 3.40-3.47*).

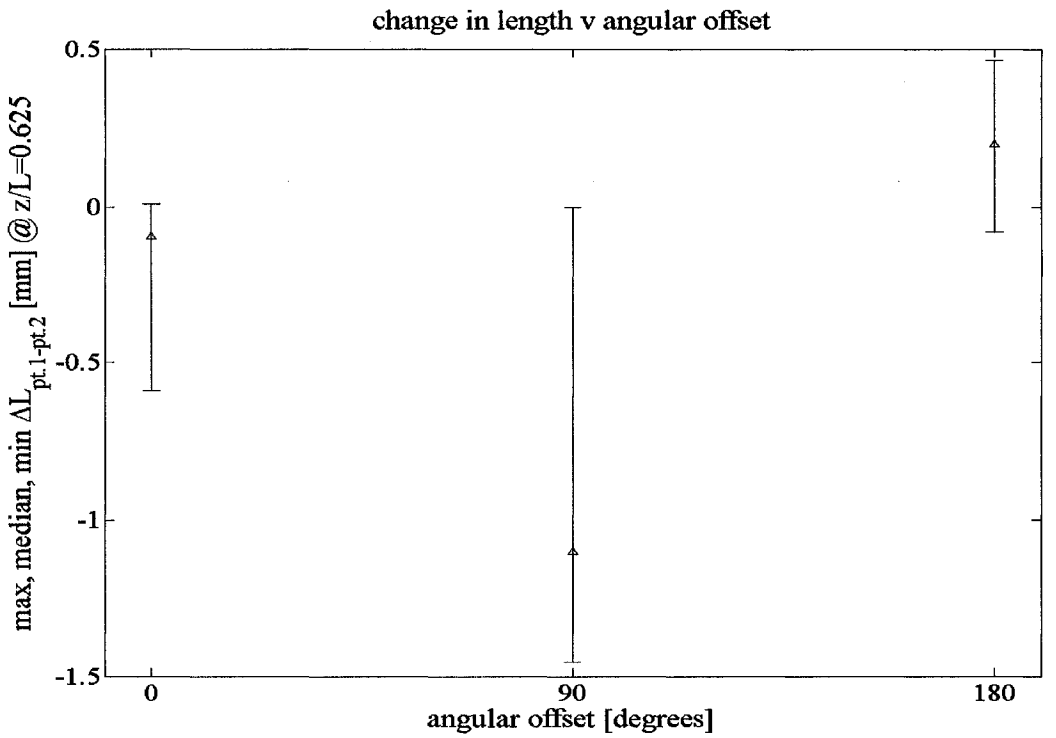

Figure 3.40 Effect of angular offset on wall collapse, ΔL pt.1-pt.2, z/L = 0.625.

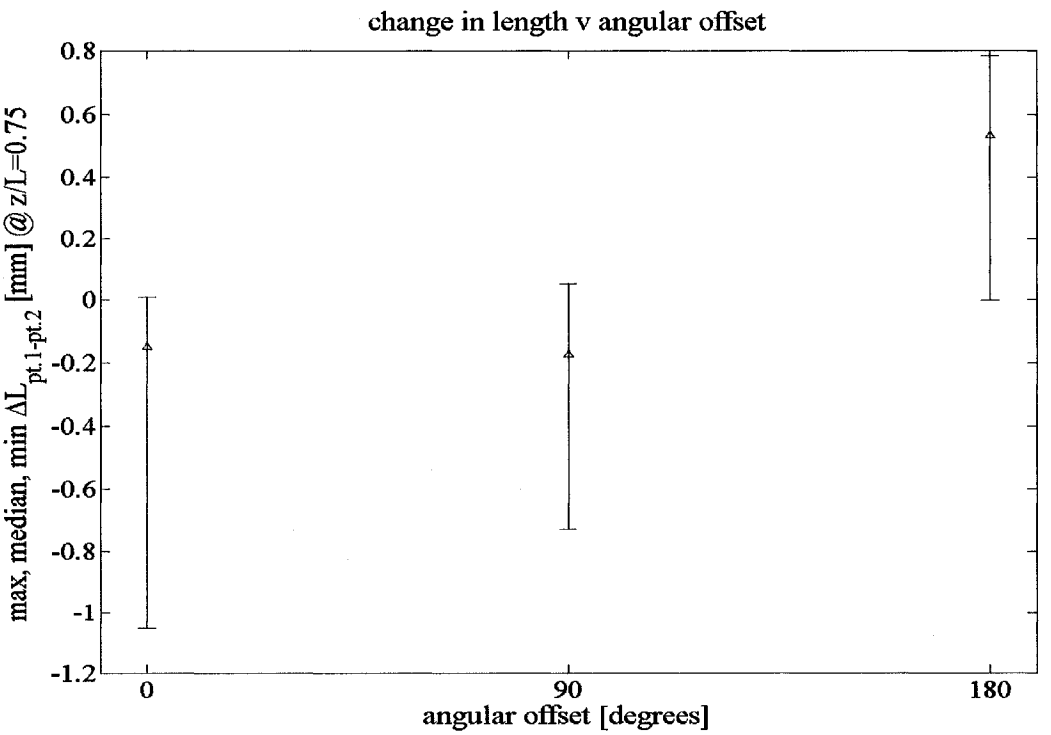

Figure 3.41 Effect of angular offset on wall collapse, ΔL pt.1-pt.2, z/L = 0.75.

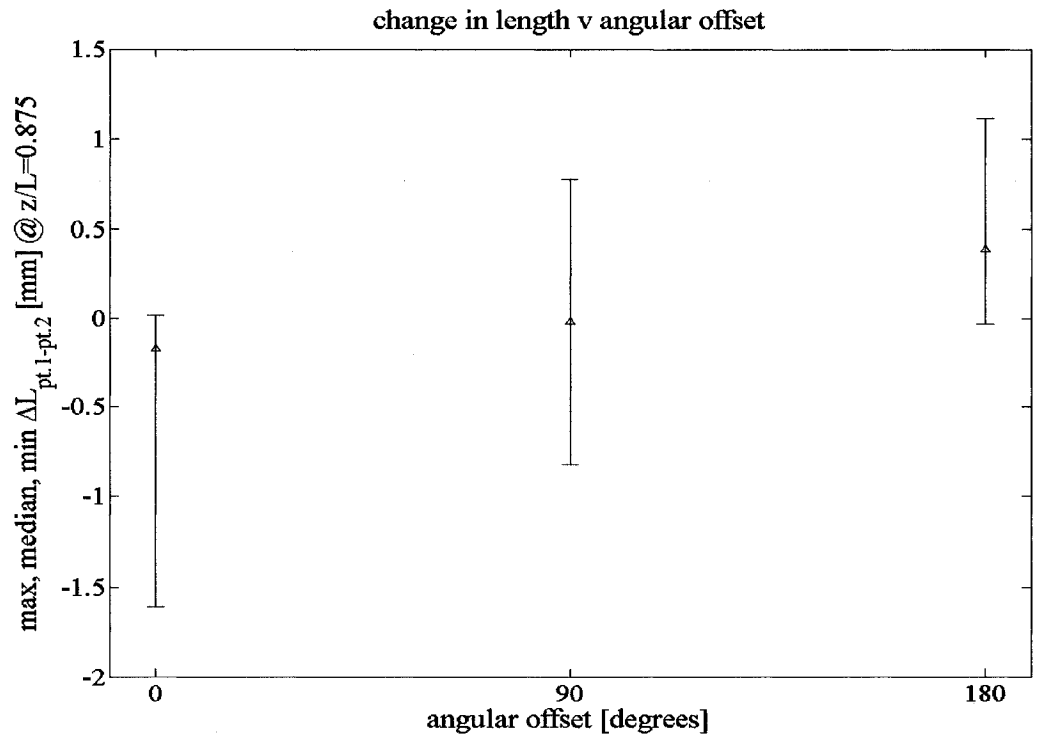

Figure 3.42 Effect of angular offset on wall collapse, ΔL pt.1-pt.2, z/L = 0.875.

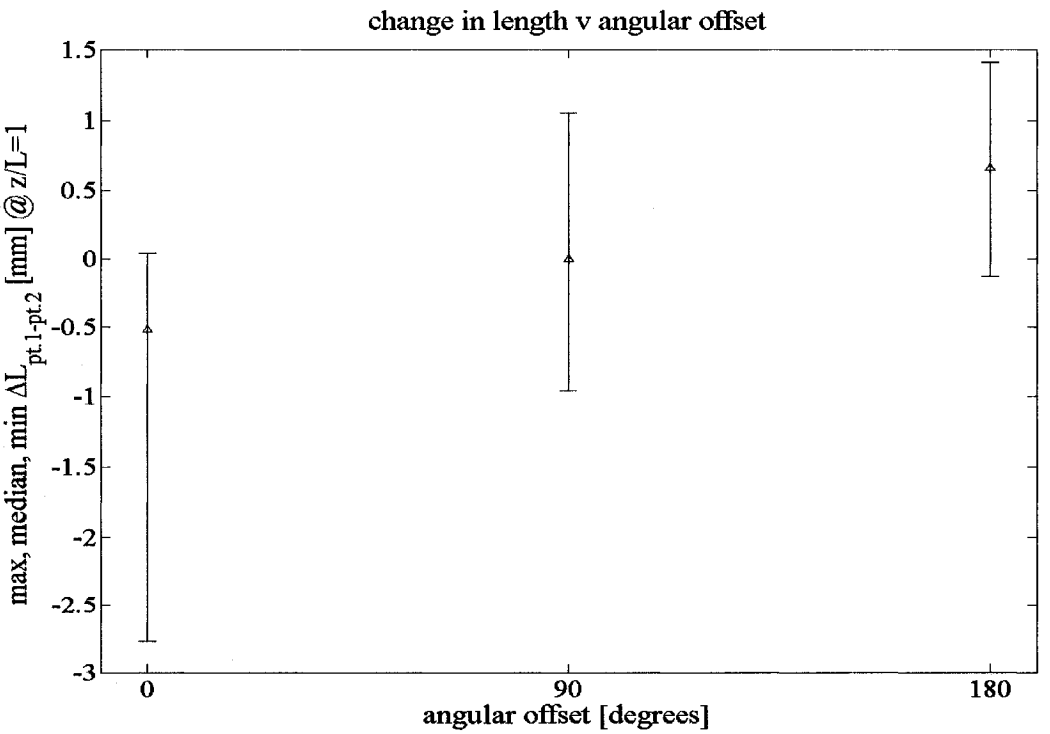

Figure 3.43 Effect of angular offset on wall collapse, ΔL pt.1-pt.2, z/L = 1.

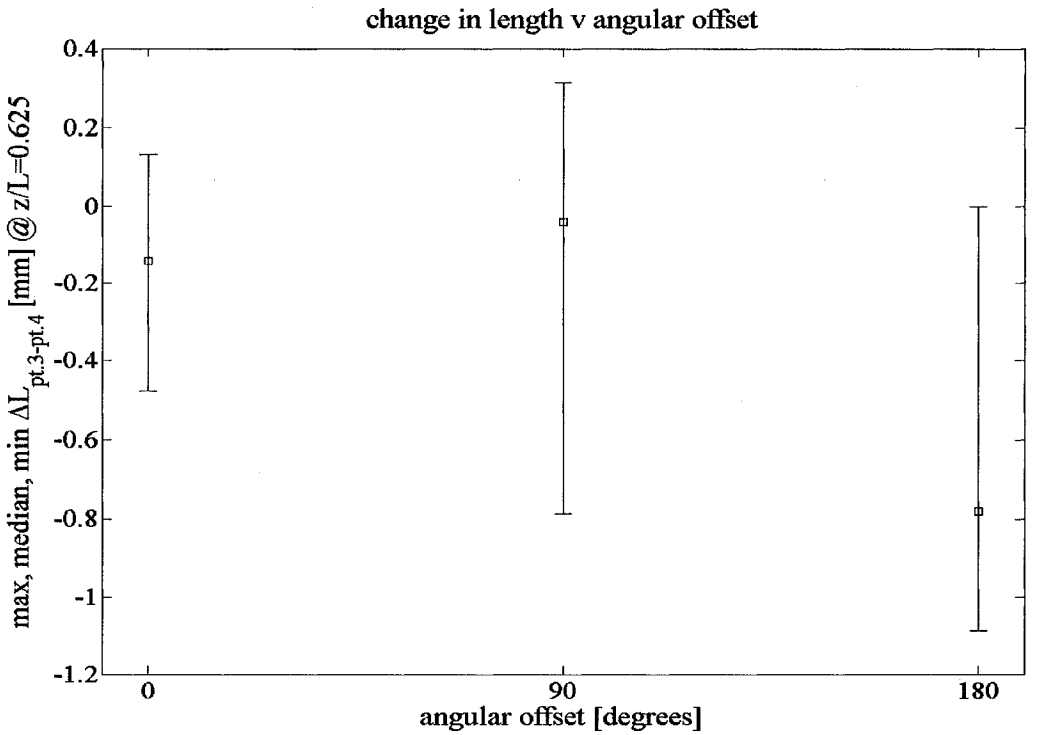

Figure 3.44 Effect of angular offset on wall collapse, ΔL pt.3-pt.4, z/L = 0.625.

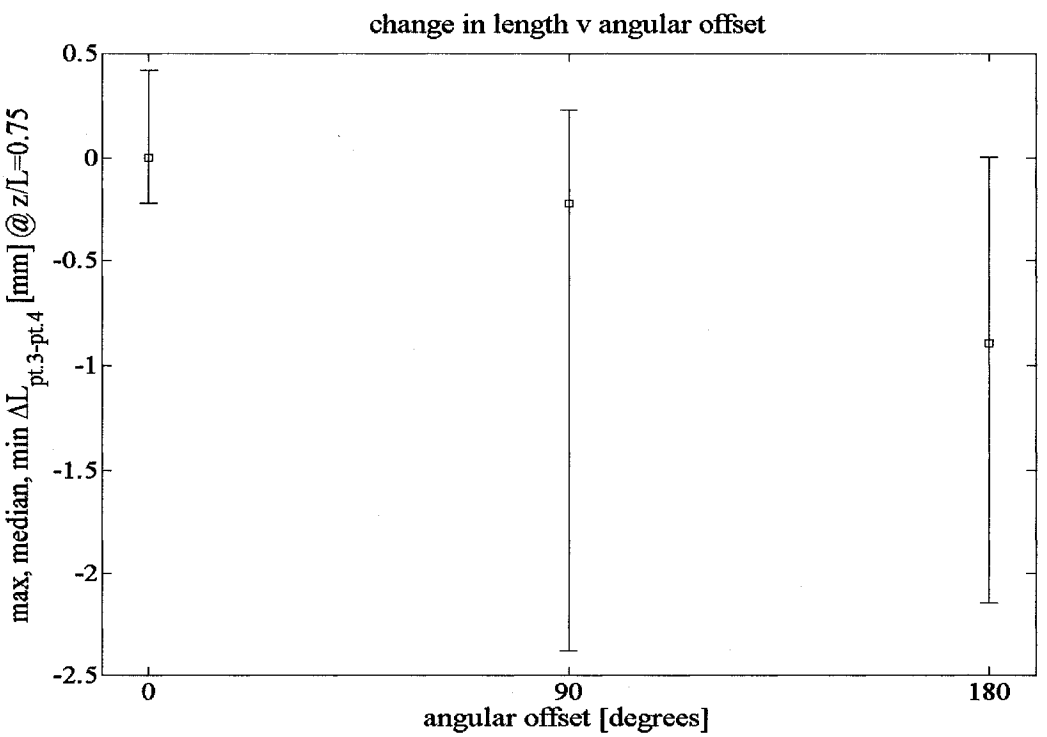

Figure 3.45 Effect of angular offset on wall collapse, ΔL pt.3-pt.4, z/L = 0.75.

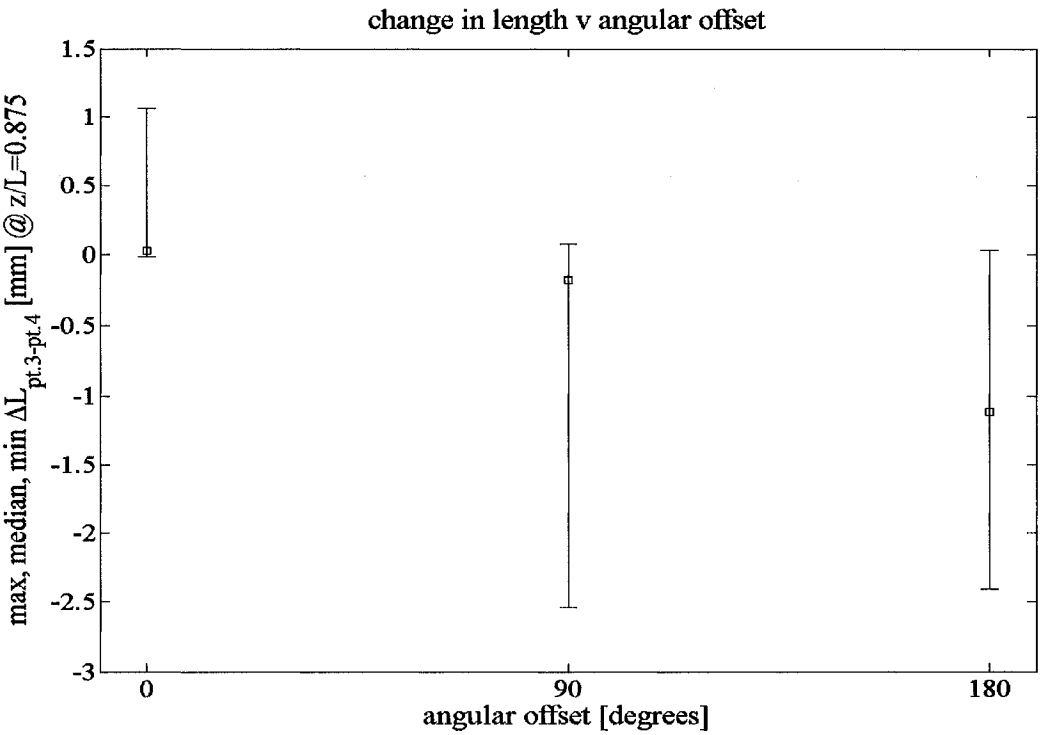

Figure 3.46 Effect of angular offset on wall collapse, ΔL pt.3-pt.4, z/L = 0.875.

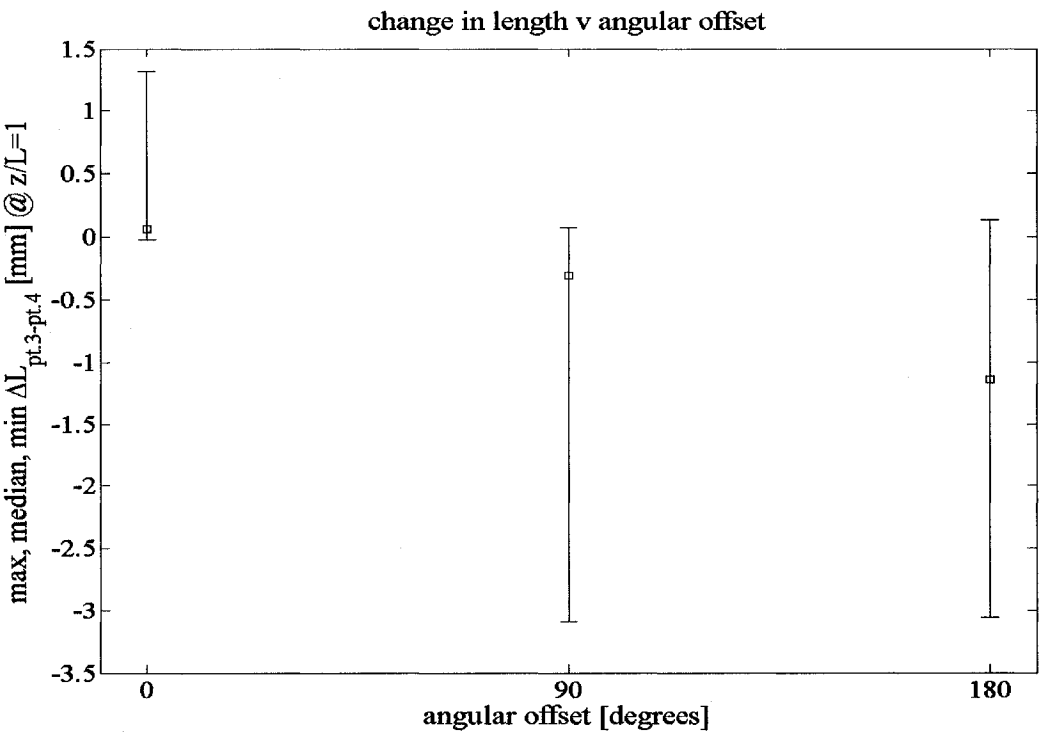

Figure 3.47 Effect of angular offset on wall collapse, ΔL pt.3-pt.4, z/L = 1.

Our previous observation on the strong influence of the closeness between the stenoses on the wall motion at the downstream end reveals itself from the increase in the ordinate scale of our plots as we progress towards the outlet. For cases where a clear contraction may be observed, it seems to be predominantly aligned in the direction of the constriction. This is a key indication of the influence of the initial angular orientation of the distal stenosis on the subsequent wall motion at the downstream end. For instance, the *0 degree case* is most susceptible to wall contraction in the pt.1 & pt.2 direction. It also has a strong tendency to extend in the pt.3 & pt.4 direction, supporting our earlier comment that significant contraction in one direction may lead to extension in its perpendicular one. The *90 degree* case adds weight to the validity of a close link between initial angular orientation of the distal stenosis and the direction of predominant wall motion at the downstream end. As shown by (*Figures 3.45-3.47*), it is at most risk for wall collapse in the pt.3 & pt.4 direction. These trends are firmly established slightly past the throat (i.e. at $z/L = 0.75$). In the cases (1, 3 & 5) involving close constrictions, it was observed that once collapse is initiated at the outlet, the information propagates upstream. It is most visible for case 5, as shown in (*Figures 3.48 & 3.49*). Whether this holds for cases (2 & 4) will require further investigations.

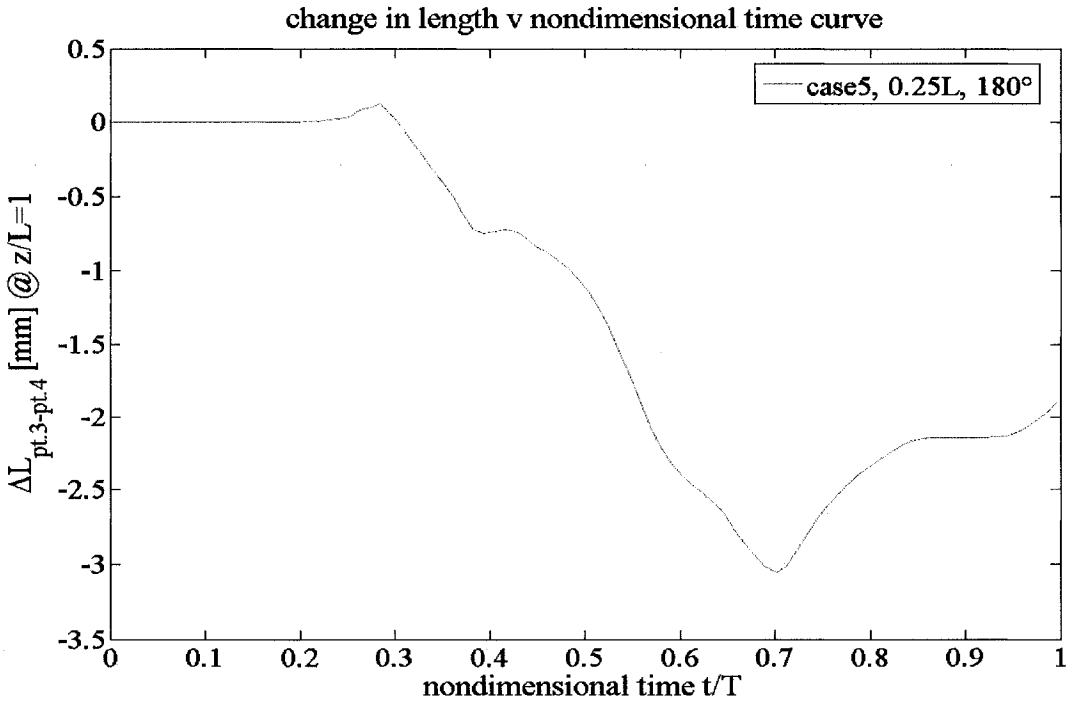

Figure 3.48 Case 5: illustrating upstream propagation, ΔL pt.3-pt.4, z/L = 1.

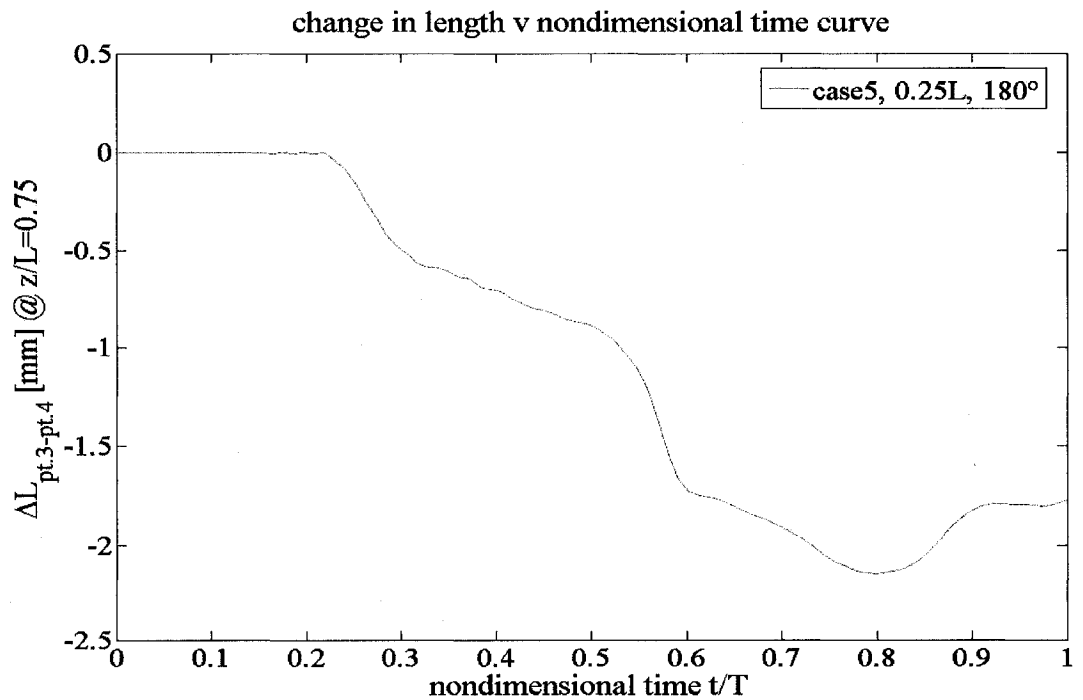

Figure 3.49 Case 5: illustrating upstream propagation, ΔL pt.3-pt.4, z/L = 0.75.

We notice in (*Figure 3.48*) that maximum wall contraction occurs at the outlet (i.e. $z/L = 1$) near $t/T = 0.7$. This information is propagated upstream to $z/L = 0.75$ (*Figure 3.49*) near $t/T = 0.8$. Thus, in this case, transmission involves a phase lag of approximately $t/T = 0.1$.

3.1.3 Observations of Wall Displacement

The previous section has demonstrated that preferential direction for wall motion occurs for cases (1 & 3). In this section, we shall examine in detail which side experiences greater displacement. The approach taken in this section is to sample a few points on the straight side and on the constricted side. We then plot the nodal displacement in the predominant direction of wall collapse as a function of time (normalized). This will provide evidence about which side experiences greater wall motion, as assessed by the amplitude of nodal displacement. The sampling locations and associated results for case 1 may be found in (*Figures 3.50 & 3.51*) for the straight side, and in (*Figures 3.52 & 3.53*) for the constricted side. Similarly, for case 5, we may look at (*Figures 3.54 & 3.55*) for the straight side, and at (*Figures 3.56 & 3.57*) for the constricted side.

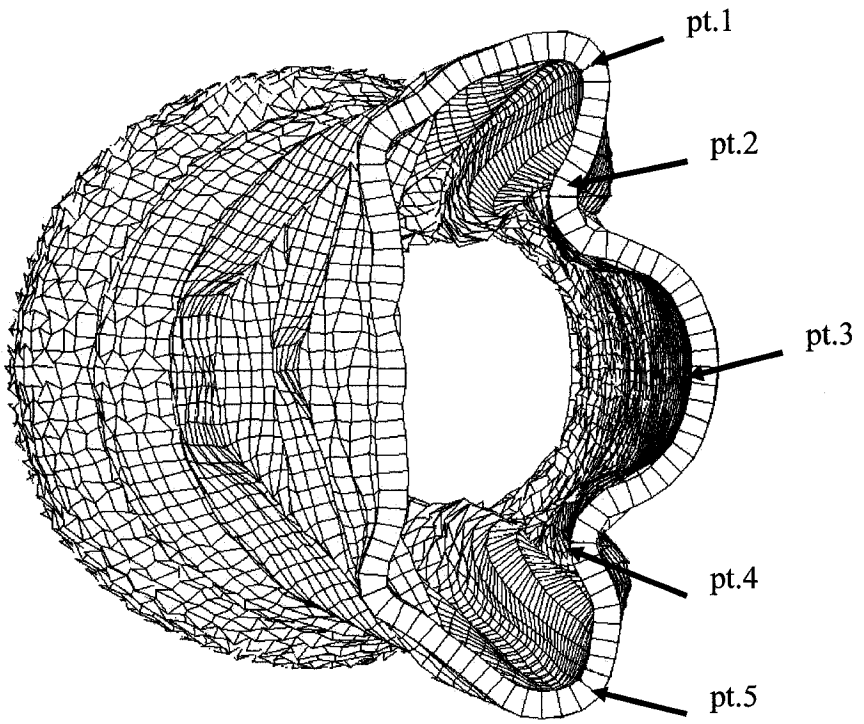

Figure 3.50 Case 1: sampling locations on the straight side, z/L = 1, t/T = 0.92.

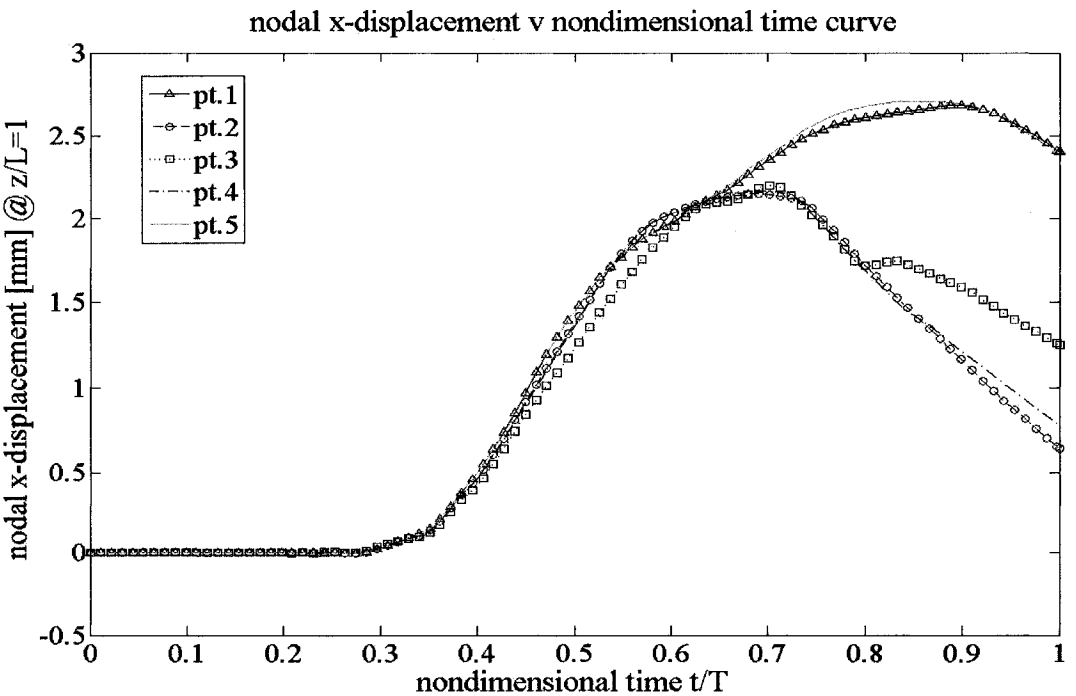

Figure 3.51 Case 1: nodal x-displacement v nondimensional time, straight side.

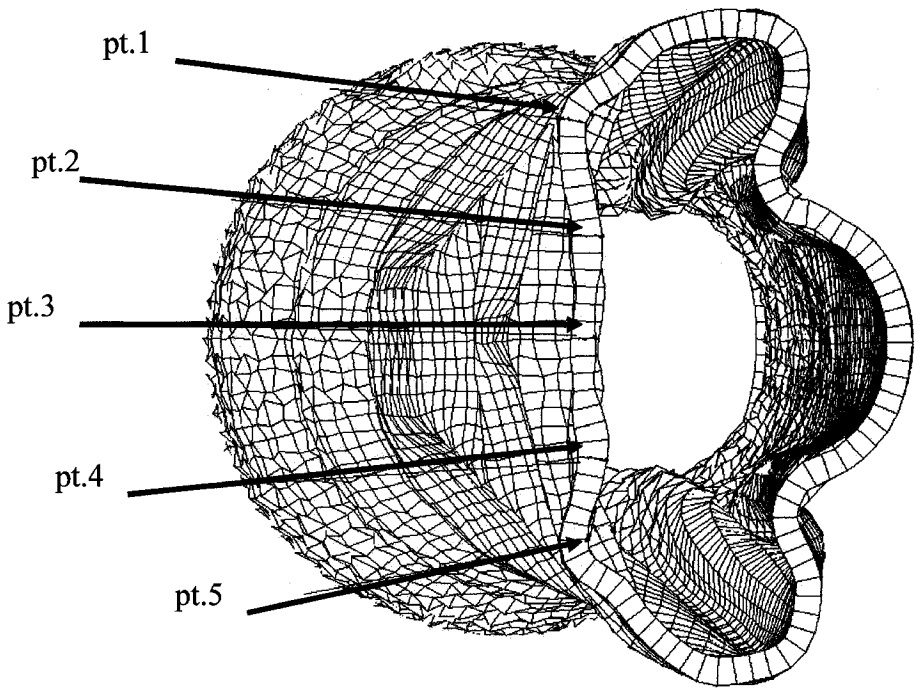

Figure 3.52 Case 1: sampling locations on the constricted side, z/L = 1, t/T = 0.92.

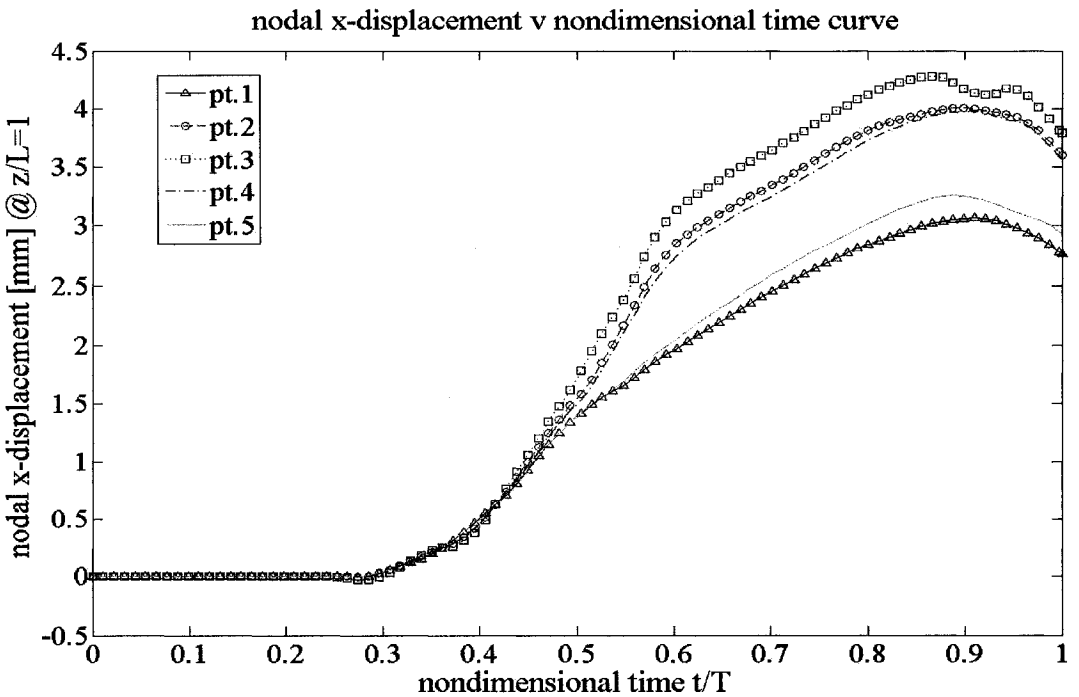

Figure 3.53 Case 1: nodal x-displacement v nondimensional time, constricted side.

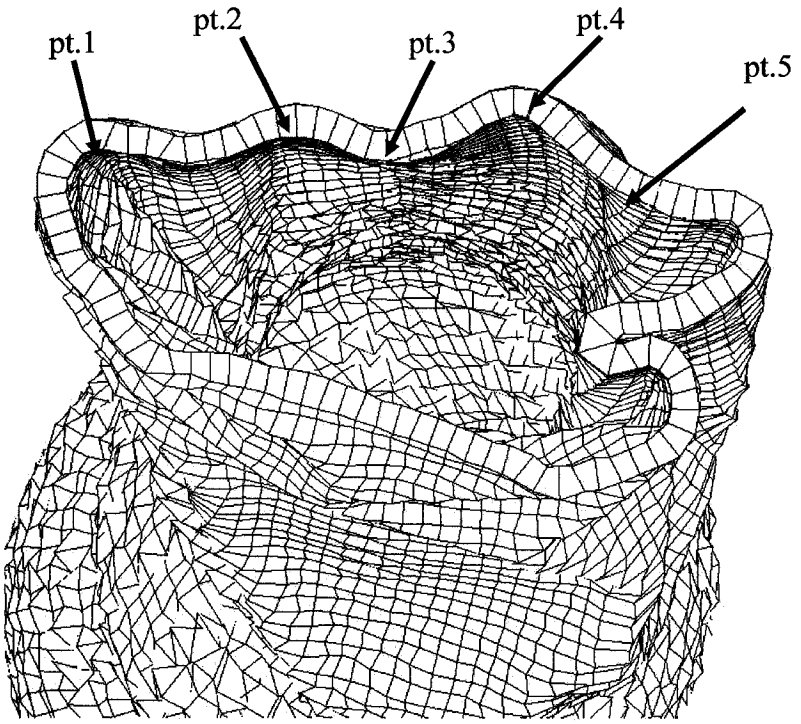

Figure 3.54 Case 3: sampling locations on the straight side, z/L = 1, t/T = 0.86.

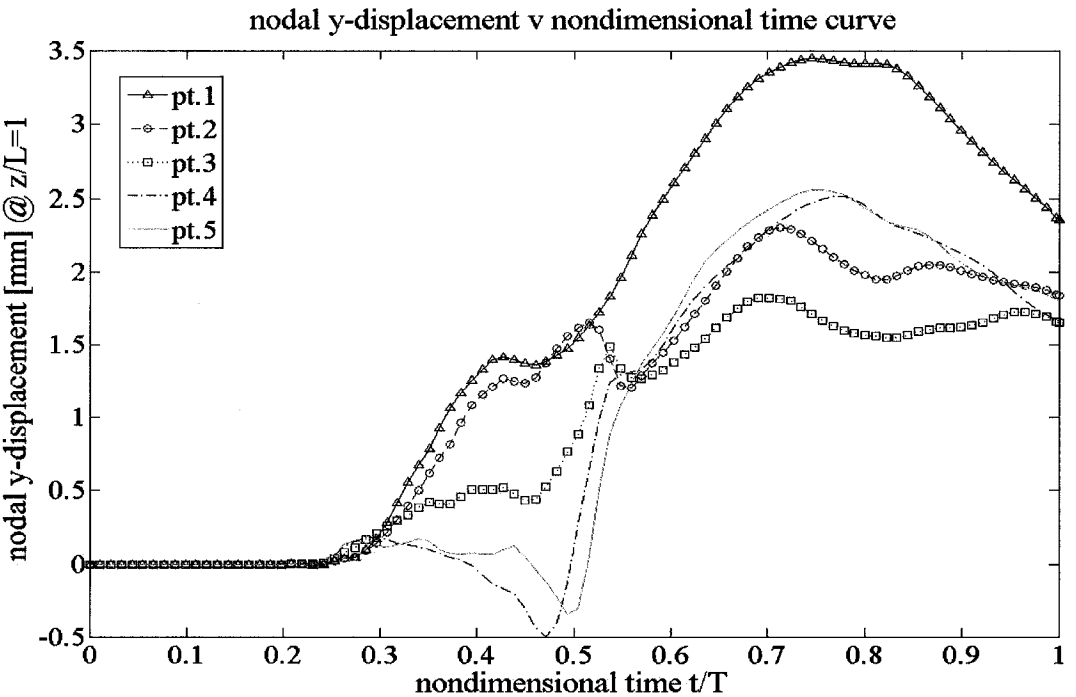

Figure 3.55 Case 3: nodal y-displacement v nondimensional time, straight side.

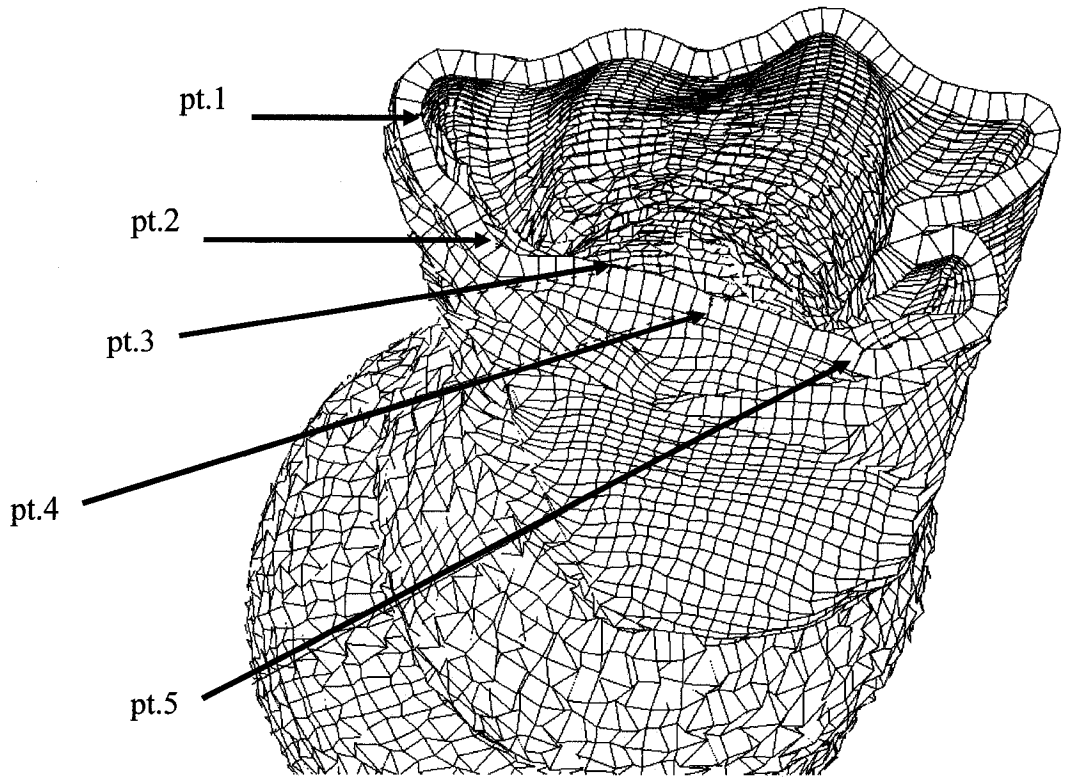

Figure 3.56 Case 3: sampling locations on the constricted side, z/L = 1, t/T = 0.86.

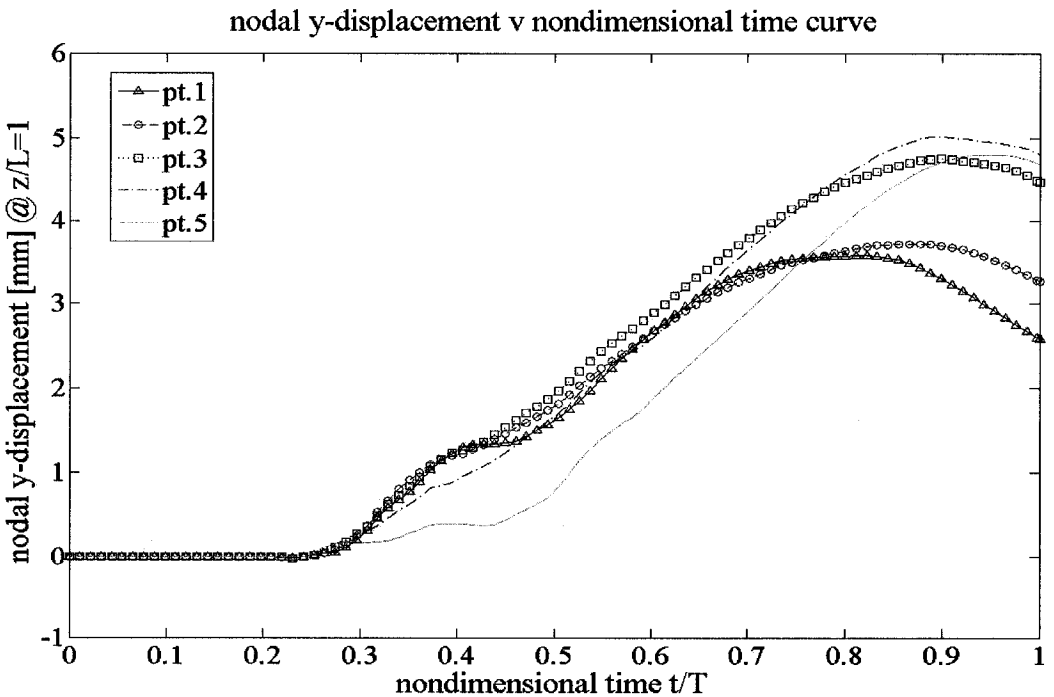

Figure 3.57 Case 3: nodal y-displacement v nondimensional time, constricted side.

As suggested by the plots, the total amplitudes of nodal displacement on the constricted side are higher than the ones on the straight side. This asymmetry in the cumulative nodal displacement in the preferential direction is a strong indication of wall collapse. At this point, we argue that wall motion at the downstream end of cases involving close constrictions are greatly influenced by the flow evolution and behavior. Thus, it may be instructive to carefully examine the flow field, which is the topic of the next section.

3.2 Three-Dimensional Velocity Field

In this section, we present a brief review of three-dimensional flow field in stenotic vessels. We emphasize the three-dimensional nature of the flow field, and as such we will reexamine some of the assumptions from the fluid dynamic diffuser flow viewpoint. This leads to a discussion on the effect of length on the flow field, as well as the influence of the angular orientation from the initial geometries.

3.2.1 Brief Review on Three-Dimensional Flow Field in Stenotic Vessels

Recent models of three-dimensional flow in stenotic vessels remain bound by a view of a collapsible tube as a two-dimensional channel. As argued by [111], this perspective treats the separation as it would occur in a fluid dynamic diffuser. The cross-section narrows then widens, leading to flow separation at one or both side wall. Recent reviews [178] on flow in stenotic vessels still subscribe to this simplification (*Figure 3.58*). To make matters worse, some experiments have been deliberately setup as quasi two-dimensional channels in which to investigate unsteady separation [179, 180].

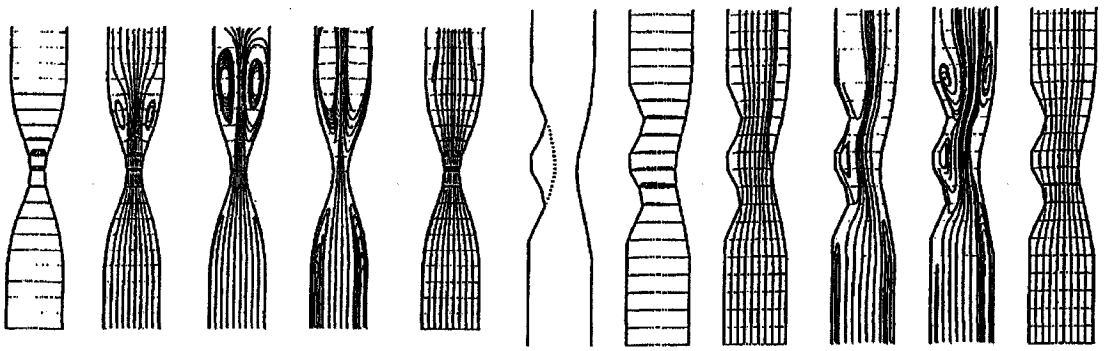

Figure 3.58 Fluid dynamic diffuser flow separation, from [178].

In view of this, it might be useful to review some of the concepts from the fluid dynamic diffuser flow viewpoint. The first point is that there is an inherent difficulty in defining flow separation unambiguously for unsteady three-dimensional flow. It was contended by [111] that a genuinely "separated" region of recirculating flow with closed streamlines does not usually exist in a three-dimensional flow; there may be retrograde flow behind an obstruction, but fluid elements may spiral through the region. In other words, the idea of separation loses some of its relevance since the fluid in the 'separated' eddies is no longer isolated from the rest [112]. Moreover, in unsteady flow, the locations where recirculating flow deflects the oncoming flow away from the wall may differ substantially from the locations where the wall shear itself changes sign. Thus, it may be more conservative to think of regions of forward and retrograde flow, when our results are interpreted.

Hazel mentions that for moderately collapsed tubes, the flow field are not dissimilar to those found in two-dimensional collapsible channel flow in the sense that fluid may locally recirculate inside a 'separation bubble' [177]. However, this semblance breaks down once the tube collapses yet further, causing the height of the separation bubble to fill the entire tube. This phenomenon is not possible in two-dimensional channel flow since the reversed flow region is closed; occupying the entire tube would imply violating conservation of mass. The important difference for a three-dimensional flow is that the reversed flow region is open and can extend to fill the entire plane, without violating conservation of mass. This brief review brings awareness of some of the intricacies of the three-dimensional nature of the flow field through a stenotic vessel. We may now

proceed to the examination of the effect of length and angular orientation on the downstream flow field. We stress that the original contribution of this work lies in accounting for the fluid structure interaction of a pulsatile flow through a serial pulmonary artery stenosis. We will carefully reexamine some of the assumptions from the fluid dynamic diffuser flow viewpoint, and expose any departure whenever possible.

3.2.2 Effect of Length on the Flow Field

Prior to the discussion, it will be helpful to introduce the figures showing the evolution of the flow field (i.e. vectors of velocities). For simplicity, we omit the fringe scale, where it is understood that red corresponds to a high level while blue represents a low level. We show case 5 because the noticeable wall osculation best illustrates the ongoing fluid structure interaction taking place. *Figure 3.59* shows a cross-section in the xz plane, while *Figure 3.60* gives a cross-section in the yz plane.

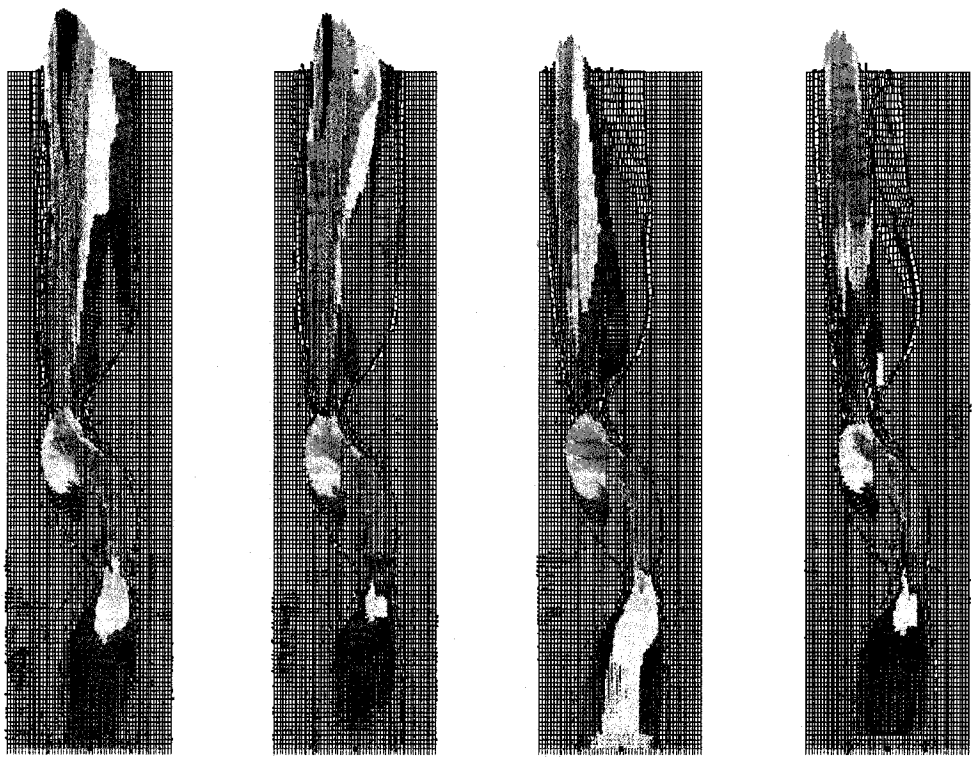

Figure 3.59 Case 5: flow field xz plane viewpoint at t/T = 0.52, 0.59, 0.80, 1 (left to right).

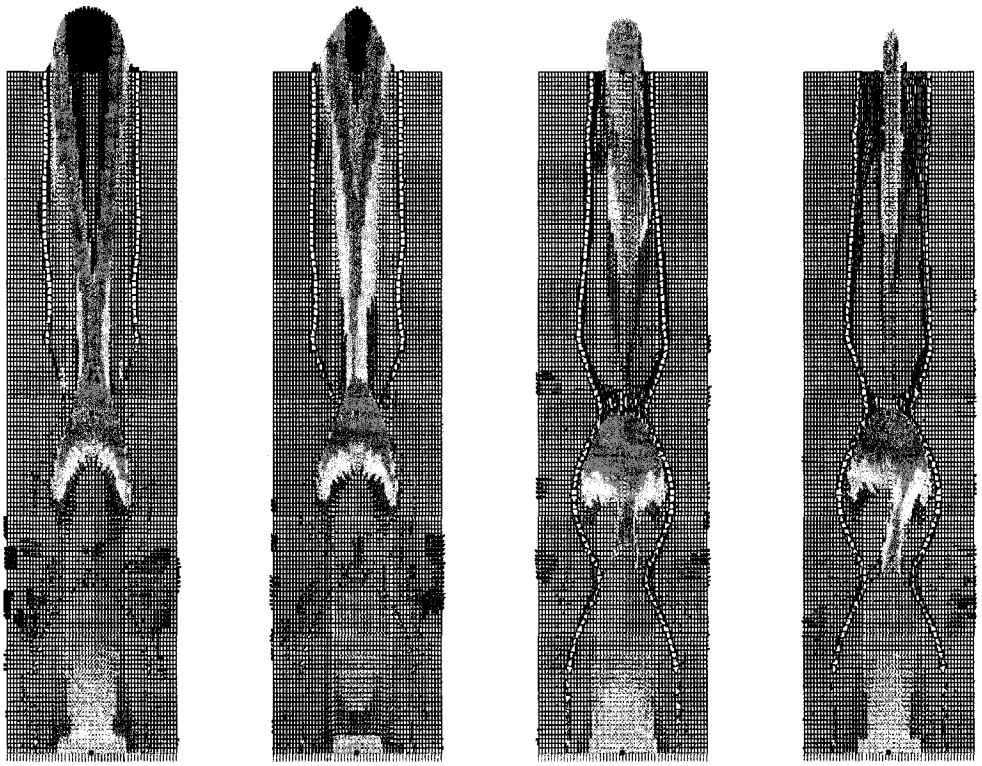

Figure 3.60 Case 5: flow field yz viewpoint at t/T = 0.46, 0.50, 0.73, 0.91 (left to right).

The effect of closely spaced constrictions on the flow field is most visible past the distal stenosis. The bulk of the flow is drawn closer to the straight side since the throat offers the path of least flow resistance. On the constricted side, the large wall slope from the widening section past the throat creates a strong adverse pressure gradient, which introduces significant flow resistance. This repels the bulk flow away, and at the same time it provides a favorable environment for viscous dissipation layer expansion on the constricted side. As the axial momentum from the upstream flow builds up on the straight side, next to the enlargement of the viscous layer on the constricted side, a flow induced instability sets in. This precipitates the visible wall collapse on the constricted side at the outlet. For cases involving close constrictions, we have previously observed that this information propagates upstream (see e.g. *section 3.1.2.2*). This has the effect of pushing the viscous layer upstream, thereby choking the core flow as seen in (*Figure 3.60*).

3.2.3 Effect of Angular Orientation on the Flow Field

In this section, we select case 3 to illustrate the influence of angular orientation on the flow field. The three-dimensional nature of the flow field is best demonstrated in *Figure 3.61*. The most striking feature is the appearance of a "half ring" jet, impinging on the wall, enclosing a "core" of insignificant or zero flow. This marks a significant departure from the fluid dynamic diffuser flow model (i.e. it would be impossible to capture this flow phenomenon from any lower order model). This flow configuration turns out to be unstable. It may be argued that, initially, the spreading of the jets into a ring shape is supported by fluid inertia, away from the strong adverse pressure gradient caused by the large wall slope on the constricted side. The accumulation of both volume flux and growth of viscous layer, at the wall where impingement occurs, compel the half ring to coalesce into a core flow closer to the centerline, as it attempts to transition towards a Poiseuille profile. Recall that significant dissipation occur near the point of jet impingement on the wall, especially if it has buckled inwards. Hazel argues that, since the fluid pressure in the region of impingement is approximately uniform across the tube, this is evidence that the spreading of the jets is driven by a balance between fluid inertia and viscous dissipation, rather than by transverse pressure gradient [177].

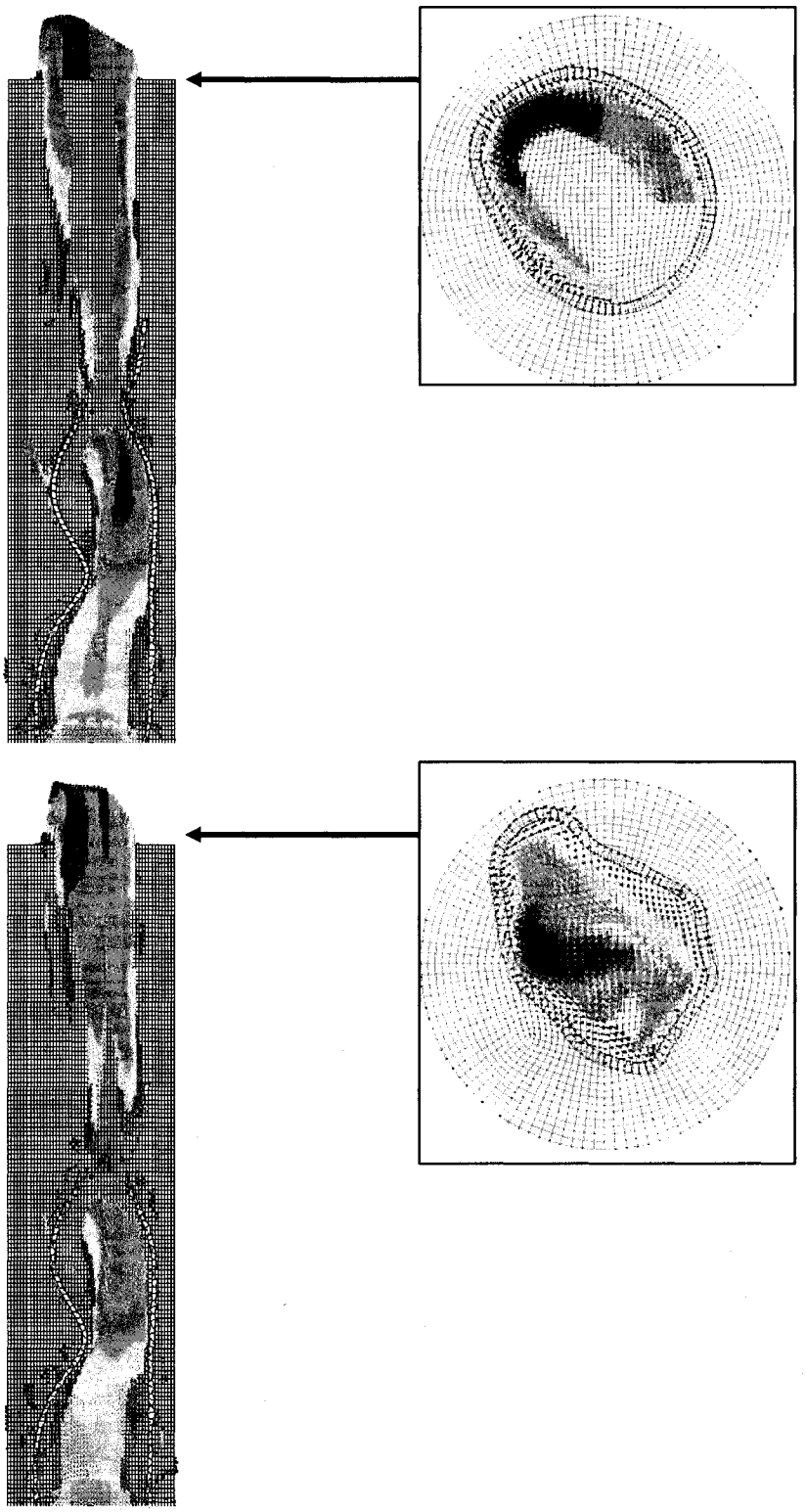

Figure 3.61 Case 3: flow field xz (left), xy (right) viewpoints at t/T = 0.33 (top), 0.39 (bottom).

The flow evolution described above suggests that the angular orientation of the distal stenosis has great influence on the direction in which the Poiseuille flow develops, i.e. it is skewed towards the wall where impingement initially happens. We finish this section by mentioning that in all cases we observed the "half ring" jet profile. However, this phenomenon is most visible in the 90 degrees cases (3 & 4).

Chapter 4.

Conclusion

4.1 Concluding Remarks

Motivated by the physiological phenomena of collapse and flow limitation for a serial pulmonary artery stenosis, we investigated the three-dimensional influence of spatial configuration on the wall motion and hemodynamic. Our numerical study focused on the effect of two geometrical parameters: the relative distance and the angular orientation between the two stenoses. Observation of the macroscopic behavior at the downstream end revealed an apparent relationship between the angular orientation of the distal stenosis and the preferential direction of wall motion. This insight led us to devise a simple metric, serving as a proxy for quantifying the degree of wall collapse. Our method consisted of measuring the change in length from the initial vessel's geometries in each of the two principal directions of constriction of the distal stenosis. Using error bars, we plotted the extreme and median values, construing any large distance above or below the median (i.e. an important asymmetry), as a strong indication of wall collapse in a preferential direction. The findings of this investigation reveal that the closeness between stenoses is a substantial indication of wall collapse at the downstream end. Moreover, the results suggest a close link between the initial angular orientation of the distal stenosis (i.e. the constriction direction) and the subsequent wall motion at the downstream end. For cases showing evidence of preferential direction of wall motion, it was found that the constricted side underwent greater cumulative displacement than the straight side, suggestive of significant wall collapse.

The summary from the fluid perspective is as follows: the effect of a close spacing between the stenoses is to increases the vulnerability of the downstream end to buckling (divergence). The manner in which the flow evolves is intimately linked to the initial geometry of the vessel. The bulk flow past a stenosis is drawn closer to the straight side, since the throat offers the path of least fluid resistance. On the constricted side, the large

wall slope from the widening section past the throat creates strong adverse pressure gradient, thus introducing significant flow resistance. This repulses the bulk flow, and creates a favorable environment for viscous dissipation layer expansion on the constricted side. The abovementioned flow behavior is manifestations of the influence of initial angular orientation on the flow field. The interplay between vessel geometry and flow field leads to an axial momentum accumulation from the upstream flow, alongside of the growth of viscous layer on the adjacent constricted side. This excessive differential proves to be unstable, as flow instability sets in. This hastens the noticeable strong wall motion at the outlet, and possibly, as we have seen in some cases, serves as an impetus to wall osculation. For cases involving close constrictions, the results suggest that the wall motion propagate upstream, once they are initiated at the outlet. This induces the migration of the viscous layer upstream, thereby choking the core flow.

Furthermore, we must stress that the angular orientation of the distal stenosis renders possible the "half ring" jets, impinging on the sidewall and enclosing a "core" of insignificant or zero flow. This marks a significant departure from the fluid dynamic diffuser flow model. This brings us to conclude that the angular orientation of the distal stenosis has great influence on the direction in which the Poiseuille flow develops, i.e. it is skewed towards the wall where impingement initially happens. This in turn has important implication for the wall motion at the outlet, owing to the tight coupling between fluid and structure.

4.2 Future Work

As previously stated, there is currently no experimentally validated data for three-dimensional artery under compression. Such experimentally validated data would increase the predictive value of our numerical simulation. However, Labrosse makes the case that data obtained from uniaxial and biaxial testing is not directly usable for the purpose of three-dimensional modeling [8]. However, he acknowledges that uniaxial tensile test on arterial strips provide important information for studying the mechanical response of excised tissues and for obtaining the stress-stain curves. Those yield interesting data about the required level of mechanical stimulus for permanent damage to occur. Nevertheless, he argues that since uniaxial test only probe one direction at a time, this limits their effectiveness. In other words, the potentially very significant interaction between different directions (i.e. circumferential, longitudinal, and radial) is not revealed by such test. This shortcoming renders uniaxial test data unusable in establishing constitutive equations for three-dimensional finite element analysis, i.e. the three-dimensional response of the model will probably be wrong, since the necessary positive definiteness of the stiffness matrix is not guaranteed.

On the other hand, biaxial testing allow for the stretching of a small piece of arterial tissue in two perpendicular directions at the same time, possibly with different values of stretch on each side. However, given that the natural curvature present in the arterial wall is not accounted in biaxial testing (i.e. the sample is stretched in a plane), data obtained from this method is unsuitable for three-dimensional analysis. Labrosse stresses that merely curve fitting experimental results would not produce a model of sufficient predictive quality. He emphasizes the need for a theoretical framework underlying the description of the material properties, with specific information provided by experiments. Constitutive equations are typically not designed to represent the mechanical interaction between the components of the arterial wall at the cellular level. Irrespective of the choice of constitutive equations, modeling improvements for the problem of concern in this thesis will rest on validated experimental data for a three-dimensional artery under compression.

An alternative area of exploration and progression for this work may lie in the three-dimensional simulations of flow induced tube oscillations. This numerical task is at the edge of what is currently possible, in terms of both obtaining fluid structure interaction convergence, and the magnitude of the three-dimensional unsteady computation. Model validation could use data from the pioneering experimental work of Bertram et al. In study [114], experiments were mounted to investigate the onset in a 'Starling resistor' of flow rate limitation and flow induced oscillations, at the lowest possible Reynolds number. It was found that oscillations did not break out below a Reynolds number of about 300. In [112], a laser Doppler anemometer was used to determine the velocity of aqueous flow downstream of a collapsible tube while the tube was executing vigorous repetitive flow induced oscillations for a time averaged Reynolds number of 10,750. Numerical simulations could reveal a more intricate level of flow details and shed new light on the mechanisms which underlie collapsible tube oscillations, in particular their onset.

4.3 Acknowledgements

The author is indebted to Professor Rosaire Mongrain for providing constructive suggestions, discussions and advice during the course of this study. His extensive experience, knowledge and fervor for the field of cardiovascular biomechanics were instrumental in providing the needed depth and broad perspective for this research. This work was supported by a research grant from the National Research Council of Canada, and Baylis Medical Company Inc. (Montreal, QC, Canada), whose assistance is gratefully acknowledged. The author would also like to thank Professor Robert Funnel for his patient and thorough review of this work, and Professor Michel Labrosse for his guidance on meshing techniques of anisotropic models. Lastly, the author is also thankful to colleagues for offering their supports, ideas and encouragement. In particular, Mr. Ian Campbell for brainstorming on various modeling approaches, and Mr. Ramses Galaz for sharing his geometrical modeling techniques.

References

[1] Yen, M. R., and Huang, W., 2001, "Pulsatile Blood Flow in the Lung Studied as an Engineering System," Introduction to Bioengineering, Y. Fung, ed., World Scientific Publishing, pp. 265-274.

[2] Kussmaul, W. G., Noordergraaf, A., and Laskey, W. K., 1992, "Right Ventricular-Pulmonary Arterial Interactions," Annals of Biomedical Engineering, 20, pp. 63-80.

[3] Nichols, W. W., and O'Rourke, M. F., 2005, "The Pulmonary Circulation," McDonald's Blood Flow in Arteries, Theoretical, Experimental and Clinical Principles, Hodder Arnold, London, pp. 309-320.

[4] Kandzari, D. E., Warner, J., O'Laughlin, M., and Harrison, K. J., 2000, "Percutaneous Stenting of Right Pulmonary Artery Stenosis in Fibrosing Mediastinitis," Catheterization and Cardiovascular Interventions, 49, pp. 321-324.

[5] Pass, R. H., Hsu, D. T., Garabedian, C. P., Schiller, M. S., Jayakumar, K. A., and Hellenbrand, W. E., 2002,"Endovascular Stent Implantation in the Pulmonary Arteries of Infants and Children without the Use of a Long Vascular Sheath," Catheterization and Cardiovascular Interventions, 55, pp. 505-509.

[6] Humphrey, J., 2002, Cardiovascular Solid Mechanics: Cells, Tissues and Organs, Springer Verlag, New York.

[7] Heath, D., and Edwards, J. E., 1958, "The Pathology of Hypertensive Pulmonary Vascular Disease: A Description of Six Grades of Structural Changes in the Pulmonary Arteries with Special Reference to Congenital Cardiac Septal Defects," Circulation, 18, pp. 533-547.

[8] Labrosse, M. R., 2007, "Structure and Mechanics of the Artery," Vascular Mechanics and Pathology, M. J. Thubrikar, ed., Springer, pp. 45-81.

[9] McDonald, D., 1974, Blood Flow in Arteries, 2nd ed., Williams & Wilkins, Baltimore.

[10] http://cancerweb.ncl.ac.uk.

[11] http://clevelandclinic.org/health/health-info.

[12] Calder, A., Chan, N., Clarkson, P., Kerr, A., and Neutze, J., 1991, "Progress of Patients with Pulmonary Atresia after Systemic to Pulmonary Arterial Shunts," Annals of Thoracic Surgery, 51, pp. 401-407.

[13] Nakanishi, T., Matsumoto, Y., Seguchi, M., Nakazawa, M., Imai, Y., and Momma, K., 1993, "Balloon Angioplasty for Post-operative Pulmonary Artery Stenosis in Transposition of the Great Arteries," Journal of the American College of Cardiology, 22, pp. 859-866.

[14] Paillole, C., Sidi, D., Kachaner, J., Planche, C., Belot, J., Villain, E., Bidois, J., Piechaud, J., and Pedroni, E., 1988, "Fate of Pulmonary Artery after Anatomic Correction of Simple Transposition of Great Arteries in Newborn Infants," Circulation, 78, pp. 870-876.

[15] Garson, A. J., Nihill, M., McNamara, D., and Cooley, D., 1979, "Status of the Adult and Adolescent after Repair of Tetralogy of Fallot," Circulation, 59, pp. 1232-1240.

[16] Kirklin, J., Blackstone, E., Pacifico, A., Kirklin, J., and Bargeron, L. J., 1984, "Risk Factors for Early and Late Failure after Repair of Tetralogy of Fallot, and their Neutralization," Journal of Thoracic and Cardiovascular Surgery, 32, pp. 208-214.

[17] Shaffer, K., Mullins, C., Grifka, R., O'Laughlin, M., McMahon, W., Ing, F., and Nihill, M., 1998, "Intravascular Stents in Congenital Heart Disease: Short- and Long-Term Results from a Large Single-Center Experience," Journal of the American College of Cardiology, 31, pp. 661-667.

[18] Driscoll, D., Offord, K., Feldt, R., Schaff, H., Puga, F., and Danielson, G., 1992, "Five-to Fifteen-Year Follow-up after Fontan Operation," Circulation, 85, pp. 469-496.

[19] http://webster.com/about/ack.htm.

[20] Nguyen, K. T., Su, S.-H., Zilberman, M., Bohluli, P., Frenkel, P., Tang, L., Eberhart, R., and Timmons, R., 2004, "Biomaterials and Stent Technology," Tissue Engineering and Novel Delivery Systems, M. J. Yaszemski, D. J. Trantolo, K.-U. Lewandrowski, V. Hasirci, D. E. Altobelli, and D. L. Wise, eds., Marcel Dekker, pp. 107-130.

[21] Fogelman, R., Nykanen, D., Smallhorn, J., McCrindle, B., Freedom, R., and Benson, L., 1995, "Endovascular Stents in the Pulmonary Circulation: Clinical Impact on Management and Medium-Term Follow-up," Circulation, 92, pp. 881-885.

[22] Mullins, C., O'Laughlin, M., and Vick, G., 1988, "Implantation of Balloon-Expandable Intravascular Grafts by Catheterization in Pulmonary Arteries and Systemic Veins," Circulation, 77, pp. 188-199.

[23] O'Laughlin, M., 1995, "Balloon-Expandable Stenting in Pediatric Cardiology," Journal of Interventional Cardiology, 8, pp. 463-475.

[24] O'Laughlin, M., Perry, S., Lock, J., and Mullins, C., 1991, "Use of Endovascular Stents in Congenital Heart Disease," Circulation, 83, pp. 1923-1939.

[25] O'Laughlin, M., Slack, M., Grifka, R., Perry, S., Lock, J., and Mullins, C., 1993, "Implantation and Intermediate-Term Follow-up of Stents in Congenital Heart Disease," Circulation, 88, pp. 605-614.

[26] Moore, J. W., Spicer, R. L., Perry, J. C., Mathewson, J. W., Kirkpatrick, S. E., George, L., Uzark, K., Mainwaring, R. L., and Lamberti, J. J., 1995, "Percutaneous use of Stents to Correct Pulmonary Artery Stenosis in Young Children after Cavopulmonary Anastomosis," American Heart Journal, 130, pp. 1245-1249.

[27] Hijazi, Z. M., Al-Fadley, F., Geggel, R. L., Marx, G. R., Galal, O., Al-Halees, Z., Abbag, F., and Fulton, D. R., 1996, "Stent Implantation for Relief of Pulmonary Artery Stenosis: Immediate and Short-Term Results," Catheterization and Cardiovascular Diagnosis, 38, pp. 16-23.

[28] Hosking, M., Benson, L., Nakanishi, T., Burrows, P., Williams, W., and Freedom, R., 1992, "Intravascular Stent Prosthesis for Right Ventricular Outflow Obstruction," Journal of the American College of Cardiology, 20, pp. 373-380.

[29] Hosking, M., Thomaidis, C., Hamilton, R., Burrows, P., Freedom, R., and Benson, L., 1992, "Clinical Impact of Balloon Angioplasty for Branch Pulmonary Arterial Stenosis," American Journal of Cardiology, 69, pp. 1467-1470.

[30] Mendelson, A., Bove, E., Lupinetti, F., Crowley, D., Lloyd, T., Federly, R., and Beekman, R., 1993, "Intra-operative and Percutaneous Stenting of Congenital Pulmonary Artery and Vein Stenosis," Circulation, 88, pp. 210-217.

[31] Casado, J., Bermudez, R., and Mullins, C., 1994, "Balloon Dilation vs Stent Implantation in Peripheral Pulmonary Branch Stenosis in Congenital Heart Defects," Journal of the American College of Cardiology, 358A, pp. 942-946.

[32] Formigari, R., Casado, J., Santoro, G., and Ballerini, L., 1998, "Treatment of Peripheral Pulmonary Stenosis," Journal of Interventional Cardiology, 11, pp. 331-336.

[33] Benson, L., Nykanen, D., and Freedom, R., 1995, "Endovascular Stents in Pediatric Cardiovascular Medicine," Journal of Interventional Cardiology, 8, pp. 767-775.

[34] Palmaz, J., 1993, "Tissue-Stent Interactions and Design Considerations," American Journal of Roentgenology, 160, pp. 613-618.

[35] Komatsu, R., Ueda, M., Naruko, T., Kojima, A., and Becker, A., 1998, "Neointimal Tissue Response at Sites of Coronary Stenting in Humans: Macroscopic, Histological and Immunohistochemical Analyses," Circulation, 98, pp. 224-233.

[36] Kastrati, A., Mehilli, J., Dirschinger, J., Pache, J., Ulm, K., Schulen, H., Seyfarth, M., Schmitt, C., Blasini, R., Neumann, F., and Schomig, A., 2001, "Restenosis after

Coronary Placement of Various Stent Types," American Journal of Cardiology, 87, pp. 34-39.

[37] Bénard, N., Perrault, R., and Coisne, D., 2006, "Computational Approach to Estimating the Effects of Blood Properties on Changes in Intra-Stent Flow," Annals of Biomedical Engineering, 34, pp. 1259-1271.

[38] Anand, M., Rajagopal, K., and Rajagopal, K., 2006, "A Viscoelastic Fluid Model for Describing the Mechanics of a Coarse Ligated Plasma Clot," Theoretical and Computational Fluid Dynamics, 20, pp. 239-250.

[39] Badimon, L., Chesebro, J., and Badimon, J., 1992, "Thrombus Formation on Ruptured Atherosclerotic Plaques and Re-thrombosis on Evolving Thrombi," Circulation, 86, pp. 74-85.

[40] Bluestein, D., Niu, L., Schoephoerster, R., and Dewanjee, M., 1997, "Fluid Mechanics of Arterial Stenosis: Relationship to the Development of Mural Thrombus," Annals of Biomedical Engineering, 25, pp. 344-356.

[41] Jacobs, M., Pourmoghadam, K., Geary, E., Reyes, A., Madan, N., McGrath, L., and Moore, J., 2002, "Fontan's Operation: Is Aspirin Enough? Is Coumadin too much?," Annals of Thoracic Surgery, 73, pp. 64-68.

[42] Morris, R., and Woodcock, J., 2004, "Evidence-Based Compression: Prevention of Stasis and Deep Vein Thrombosis," Annals of Surgery, 239, pp. 162-171.

[43] Pifarre, R., 1998, "Thrombosis and Cardiovascular Disease," Medical Clinics of North America, 82, pp. 511-522.

[44] Shortland, A., Jarvis, J., and Salmons, S., 2003, "Hemodynamic Considerations in the Design of a Skeletal Muscle Ventricle," Medical and Biological Engineering and Computing, 41, pp. 529-535.

[45] Strony, J., Beaudoin, A., Brands, D., and Adelman, B., 1993, "Analysis of Shear Stress and Hemodynamic Factors in a Model of Coronary Artery Stenosis and Thrombosis," American Journal of Physiology, 265, pp. H1787-H1796.

[46] Fischman, D., 1994, "A Randomized Comparison of Coronary-Stent Placement and Balloon Angioplasty in the Treatment of Coronary Artery Disease. Stent Restenosis Study Investigators," New England Journal of Medicine, 331, pp. 496-501.

[47] Serruys, P., 1994, "A Comparison of Balloon-Expandable Stent Implantation with Balloon Angioplasty in Patients with Coronary Artery Disease. Benestent Study Group," New England Journal of Medicine, 331, pp. 489-495.

[48] Topol, E., 1994, "Caveats About Elective Coronary Stenting," New England Journal of Medicine, 331, pp. 539-541.

[49] Boo, Y., Hwang, J., Sykes, M., Michell, B., Kemp, B., Lum, H., and Jo, H., 2002, "Shear Stress Stimulates Phosphorylation of eNOS at Ser^{635} by a Protein Kinase A-Dependent Mechanism," American Journal of Physiology Heart and Circulatory Physiology 283, pp. H1819-H1828.

[50] Corson, M., James, N., Latta, S., Nerem, R., Berk, B., and Harrison, D., 1996, "Phosphorylation of Endothelial Nitric Oxide Synthase in Response to Fluid Shear Stress," Circulation Research, 79, pp. 984-991.

[51] Dai, G., Kaazempur-Mofrad, M., Natarajan, S., Zhang, Y., Vaughn, S., Blackman, B., Kamm, R., Garcia-Cardena, G., and Gimbrone, M. J., 2004, "Distinct Endothelial Phenotypes Evoked by Arterial Waveforms Derived from Atherosclerosis-Susceptible and -Resistant Regions of Human Vasculature," Proceedings of the National Academy of Sciences of the United States of America, 101, pp. 14871-14876.

[52] Gonzales, R., and Wick, T., 1996, "Hemodynamic Modulation of Monocytic Cell Adherence to Vascular Endothelium," Annals of Biomedical Engineering, 24, pp. 382-393.

[53] Jung, J., Hassanein, A., and Lyczkowski, R. W., 2006, "Hemodynamic Computation using Multiphase Flow Dynamics in a Right Coronary Artery," Annals of Biomedical Engineering, 34, pp. 393-407.

[54] Stone, P., Coskun, A., Yeghiazarians, Y., Kinlay, S., Popma, J., Kuntz, R., and Feldman, C., 2003, "Prediction of Sites of Coronary Atherosclerosis Progression: In Vivo Profiling of Endothelial Shear Stress, Lumen, and Outer Vessel Wall Characteristics to Predict Vascular Behavior," Current Opinion in Cardiology, 18, pp. 458-470.

[55] Walpola, P., Gotlieb, A., Cybulsky, M., and Langille, B., 1995, "Expression of ICAM-1 and VCAM-1 and Monocyte Adherence in Arteries Exposed to Altered Shear Stress," Arteriosclerosis, Thrombosis, and Vascular Biology, 15, pp. 2-10.

[56] Wasserman, S., Mehraban, F., Komuves, L., Yang, R., Tomlinson, J., Zhang, Y., Spriggs, F., and Topper, J., 2002, "Gene Expression Profile of Human Endothelial Cells Exposed to Sustained Fluid Shear Stress," Physiological Genomics, 12, pp. 13-23.

[57] Carlier, S., Van Damme, L., Blommerde, C., and Wentzel, J., 2003, "Augmentation of Wall Shear Stress Inhibits Neointimal Hyperplasia after Stent Implantation: Inhibition through Reduction of Inflammation?," Circulation, 107, pp. 2741-2746.

[58] Ku, D., Giddens, D., Zarins, C., and Glagov, S., 1985, "Pulsatile Flow and Atherosclerosis in the Human Carotid Bifurcation. Positive Correlation between Plaque Location and Low Oscillating Shear Stress," Arteriosclerosis, 5, pp. 293-302.

[59] LaDisa, J. F., Jr, Olson, L. E., Guler, I., Hettrick, D. A., Kersten, J. R., and Pagel, P. S., 2005, "Circumferential Vascular Deformation after Stent Implantation Alters Wall Shear Stress Evaluated with Time-Dependent 3D Computational Fluid Dynamics Models," Journal of Applied Physiology, 98, pp. 947-957.

[60] Moore, J. E. J., Xu, C., Glagov, S., Zarins, C., and Ku, D., 1994, "Fluid Wall Shear Stress Measurements in a Model of the Human Abdominal Aorta: Oscillatory Behavior and Relationship to Atherosclerosis," Atherosclerosis, 110, pp. 225-240.

[61] Stone, P., Coskun, A., Kinlay, S., and Clark, M., 2003, "Effect of Endothelial Shear Stress on the Progression of Coronary Artery Disease, Vascular Remodeling, and In-Stent Restenosis in Humans: In Vivo 6-Month Follow-up Study," Circulation, 108, pp. 438-444.

[62] Traub, O., and Berk, B., 1998, "Laminar Shear Stress, Mechanisms by which Endothelial Cells Transducer an Atheroprotective Force," Arteriosclerosis, Thrombosis, and Vascular Biology, 18, pp. 677-685.

[63] Joner, M., Finn, A. V., Farb, A., Mont, E. K., Kolodgie, F. D., Ladich, E., Kutys, R., Skorija, K., Gold, H. K., and Virmani, R., 2006, "Pathology of Drug-Eluting Stents in Humans, Delayed Healing and Late Thrombotic Risk," Journal of the American College of Cardiology, 48, pp. 193-202.

[64] Rogers, C., Parikh, S., Seifert, P., and Edelman, E., 1996, "Endogenous Cell Seeding: Remnant Endothelium after Stenting Enhances Vascular Repair," Circulation, 94, pp. 2909-2914.

[65] Schwartz, R., Holmes, D., and Topol, E., 1992, "The Restenosis Paradigm Revisited: An Alternative Proposal for Cellular Mechanisms," Journal of the American College of Cardiology, 20, pp. 1284-1293.

[66] Schwartz, R., Huber, K., Murphy, J., Edwards, W., Camrud, A., Vlietstra, R., and Holmes, D., 1992, "Restenosis and Proportional Neointimal Response to Coronary Artery Injury: Results in a Porcine Model," Journal of the American College of Cardiology, 19, pp. 267-274.

[67] Fingerle, J., Au, T., Clowes, A., and Reidy, M., 1990, "Intimal Lesion Formation in Rat Carotid Arteries after Endothelial Denudation in the Absence of Metal Injury," Arteriosclerosis, 10, pp. 1082-1087.

[68] Clowes, A., Clowes, M., Fingerle, J., and Reidy, M., 1989, "Kinetics of Cellular Proliferation after Arterial Injury. V. Role of Acute Distension in the Induction of Smooth Muscle Proliferation," Laboratory Investigation, 70, pp. 360-364.

[69] Walker, L., Ramsay, M., and Bowyer, D., 1983, "Endothelial Healing Following Defined Injury to Rabbit Aorta: Depth of Injury and Mode of Repair," Arteriosclerosis, 47, pp. 123-130.

[70] Rogers, C., and Edelman, E., 1995, "Endovascular Stent Design Dictates Experimental Restenosis and Thrombosis," Circulation, 91, pp. 2995-3001.

[71] Colombo, A., Hall, P., Nakamura, S., Almagor, Y., Maiello, L., Martini, G., Gaglione, A., Goldberg, S., and Tobis, J., 1995, "Intracoronary Stenting without Anticoagulation Accomplished with Intravascular Ultrasound Guidance," Circulation, 91, pp. 1676-1688.

[72] Savage, M., Fischman, D., Douglas, J. J., Pepine, C., Werner, J., Bailey, S., Rake, R., and Goldberg, S., 1997, "The Dark Side of High Pressure Stent Deployment," Journal of the American College of Cardiology, 29, p. 368A.

[73] Hirshfeld, J., Schwartz, J., Jugo, R., Macdonald, R., Goldberg, S., Savage, M., Bass, T., Vetrovec, G., Cowley, M., Taussig, A., Whitworth, H., Margolis, J., Hill, J., and Pepine, C., 1991, "Restenosis after Coronary Angioplasty: A Multivariate Statistical Model to Relate Lesion and Procedure Variables to Restenosis," Journal of the American College of Cardiology, 18, pp. 647-656.

[74] Roubin, G., Douglas, J. J., and King, S. I., 1988, "Influence of Balloon Size on Initial Success, Acute Complications, and Restenosis after Percutaneous Trans-Luminal Coronary Angioplasty," Circulation, 78, pp. 557-565.

[75] Sarembock, I., LaVeau, P., Sigal, S., TImms, I., Sussman, J., Haudenchild, C., and Ezekowitz, M., 1989, "Influence of Inflation Pressure and Balloon Size on the Development of Intimal Hyperplasia after Balloon Angioplasty: A Study in the Atherosclerotic Rabbit," Circulation, 80, pp. 1029-1040.

[76] Holzapfel, G., Stadler, M., and Gasser, T. C., 2005, "Changes in the Mechanical Environment of Stenotic Arteries during Interaction with Stents: Computational Assessment of Parametric Stent Designs," ASME Journal of Biomechanical Engineering, 127, pp. 166-180.

[77] Formigari, R., Santoro, G., Guccione, P., Giamberti, A., Pasquini, L., Grigioni, M., and Ballerini, L., 2000, "Treatment of Pulmonary Artery Stenosis after Arterial Switch Operation: Stent Implantation vs. Balloon Angioplasty," Catheterization and Cardiovascular Interventions, 50, pp. 207-211.

[78] Rothman, A., Perry, S., Keane, J., and Lock, J., 1990, "Early results and follow-up of balloon angioplasty for branch pulmonary artery stenosis," Journal of the American College of Cardiology, 15, pp. 1109-1117.

[79] Westerhof, N., Stergiopulos, N., and Noble, M. I., 2005, "Arterial Stenosis," Snapshots of Hemodynamics, Springer, pp. 17-20.

[80] Tang, D., Yang, C., Kobayashi, S., and Ku, D. N., 2001, "Steady Flow and Wall Compression in Stenotic Arteries: A Three-Dimensional Thick-Wall Model with Fluid-Wall Interactions," ASME Journal of Biomechanical Engineering, 123, pp. 548-557.

[81] Kobayashi, S., Tang, D., and Ku, D. N., 2004, "Collapse in High-Grade Stenosis during Pulsatile Flow Experiments," JSME International Journal, 47, pp. 1010-1018.

[82] Cao, J., and Rittgers, S., 1998, "Particle Motion within in Vitro Models of Stenosed Internal Carotid and Left Anterior Descending Coronary Arteries," Annals of Biomedical Engineering, 26, pp. 190-199.

[83] Fogelson, A. L., 1992, "Continuum Models of Platelet Aggregation: Formulation and Mechanical Properties," SIAM Journal on Applied Mathematics, 52, pp. 1089-1110.

[84] Ku, D. N., 1997, "Blood Flow in Arteries," Annual Review of Fluid Mechanics, 29, pp. 399-434.

[85] Ku, D. N., Giddens, D., Phillips, D., and Strandness, J., DE, 1985, "Hemodynamics of the Normal Human Carotid Bifurcation: in Vitro and in Vivo Studies," Ultrasound in Medicine and Biology, 11, pp. 13-26.

[86] Rittgers, S., Yu, Y., and Strony, J., 1998, "Thrombus Formation in Moderate Coronary Stenosis Using 2D-LDA," Proceedings of the Third World Congress of Biomechanics, p. 201.

[87] Derafshi, Z., Pritchard, W., Sankar, L., and Giddens, D., 1993, "Computational Study of Fluid Dynamic Effects on Near-Wall Monocyte Behavior," 1993 Proceedings of the ASME Bioengineering Conference, 24, p. 307.

[88] Gonzales, R., and Wick, T., 1996, "Hemodynamic Modulation of Monocyte Cell Adherence to Vascular Endothelium," American Journal of Pathology, 103, pp. 382-393.

[89] Fung, Y., 1993, Biomechanics, Mechanical Properties of Living Tissues, 2nd ed., Springer-Verlag, New York.

[90] Fung, Y., 1997, Biodynamics, Circulation, 2nd ed., Springer-Verlag, New York.

[91] Fung, Y., Liu, S. Q., and Zhou, J., 1993, "Remodeling of the Constitutive Equation While a Tissue Remodels Itself Under Stress," ASME Journal of Biomechanical Engineering, 115, pp. 453-459.

[92] Liu, S. Q., and Fung, Y., 1996, "Indicial Functions of Arterial Remodeling in Response to Locally Altered Blood Pressure," American Journal of Physiology, 270, pp. H1323-H1333.

[93] Fry, D., 1968, "Acute Vascular Endothelial Changes Associated with Increased Blood Velocity Gradients," Circulation Research, 22, pp. 165-197.

[94] Ramstack, J., Zuckerman, L., and Mockros, L., 1979, "Shear Induced Activation of Platelets," Journal of Biomechanics, 12, pp. 113-125.

[95] Varghese, S. S., and Frankel, S. H., 2003, "Numerical Modeling of Pulsatile Turbulent Flow in Stenotic Vessels," ASME Journal of Biomechanical Engineering, 125, pp. 445-460.

[96] Loree, H., Kamm, R., Atkinson, C., and Lee, R., 1991, "Turbulent Pressure Fluctuation on Surface of Model Vascular Stenosis," American Journal of Physiology, 261, pp. H644-H650.

[97] May, P., Arrouvel, C., Revol, M., Servant, J., and Vicaut, E., 2002, "Detection of Hemodynamic Turbulence in Experimental Stenosis: An In Vivo Study in the Rat Carotid Artery," Journal of Vascular Research, 39, pp. 21-29.

[98] Grotberg, J. B., and Jensen, O. E., 2004, "Biofluid Mechanics in Flexible Tubes," Annual Review of Fluid Mechanics, 36, pp. 121-147.

[99] Bertram, C., 1986, "Unstable Equilibrium Behavior in Collapsible Tubes," Journal of Biomechanics, 19, pp. 61-69.

[100] Brower, R., and Scholten, C., 1975, "Experimental Evidence on the Mechanism for the Instability of Flow in Collapsible Vessels," Medical and Biological Engineering and Computing, 13, pp. 839-845.

[101] Heil, M., and Pedley, T., 1995, "Large Axisymmetric Deformation of a Cylindrical Shell Conveying a Viscous Flow," Journal of Fluids and Structures, 9, pp. 237-256.

[102] Kamm, R., and Shapiro, A., 1979, "Unsteady Flow in a Collapsible Tube Subjected to External Pressure or Body Force," Journal of Fluid Mechanics, 95, pp. 1-78.

[103] Ku, D. N., Zeigler, M., Binns, R., and Stewart, M., 1989, "A Study of Predicted and Experimental Wall Collapse in Models of Highly Stenotic Arteries," Proceedings of the 2nd International Symposium on Biofluid Mechanics and Biorheology, pp. 409-416.

[104] Ku, D. N., Zeigler, M., and Downing, J., 1990, "One-Dimensional Steady Inviscid Flow through a Stenotic Collapsible Tube," ASME Journal of Biomechanical Engineering, 112, pp. 444-450.

[105] Rosar, M., 1995, "A Three-Dimensional Computer Model for Fluid Flow through a Collapsible Tube," Ph.D. Thesis, New York University.

[106] Rosar, M., 1998, "Fluid Flow in Elastic Tubes: A Three-Dimensional, Immersed Boundary Numerical Model," Proceedings of the 3rd World Congress of Biomechanics, p. 35.

[107] Shapiro, A., 1977, "Steady Flow in Collapsible Tubes," ASME Journal of Biomechanical Engineering, 99, pp. 126-147.

[108] Elad, D., Katz, D., Kimmel, E., and Einav, S., 1991, "Numerical Schemes for Unsteady Fluid Flow through Collapsible Tubes," Journal of Biomedical Engineering, 13, pp. 10-18.

[109] Bertram, C., and Castles, R., 1999, "Flow Limitation in Uniform Thick-Walled Collapsible Tubes," Journal of Fluids and Structures, 13, pp. 399-418.

[110] Gavriely, N., Shee, T., Cugell, D., and Grotberg, J. B., 1989, "Flutter in Flow-Limited Collapsible Tubes - a Mechanism for Generation of Wheezes," Journal of Applied Physiology, 66, pp. 2251-2261.

[111] Bertram, C., Diaz de Tuesta, G., and Nugent, A., 2001, "Laser-Doppler Measurements of Velocities Just Downstream of a Collapsible Tube during Flow-Induced Oscillations," ASME Journal of Biomechanical Engineering, 123, pp. 493-499.

[112] Bertram, C., and Nugent, A., 2005, "The Flow Field Downstream of an Oscillating Collapsed Tube," ASME Journal of Biomechanical Engineering, 127, pp. 39-45.

[113] Zamir, M., 2000, The Physics of Pulsatile Flow, Springer-Verlag, New York.

[114] Bertram, C., and Tscherry, J., 2006, "The Onset of Flow-Rate Limitation and Flow-Induced Oscillations in Collapsible Tubes," Journal of Fluids and Structures, 22, pp. 1029-1045.

[115] Oates, G., 1975, "Fluid Flow in Soft-Walled Tubes, I. Steady Flow," Medical and Biological Engineering and Computing, 13, pp. 773-778.

[116] Bertram, C., 1987, "The Effects of Wall Thickness, Axial Strain and End Proximity on the Pressure-Area Relation of Collapsible Tubes," Journal of Biomechanics, 20, pp. 863-876.

[117] Elad, D., Kamm, R., and Shapiro, A., 1989, "Steady Compressible Flow in Collapsible Tubes: Application to Forced Expiration," Journal of Fluid Mechanics, 203, pp. 401-418.

[118] Knowlton, F., and Starling, E., 1912, "The Influence of Variations in Temperature and Blood-Pressure on the Performance of the Isolated Mammalian Heart," Journal of Physiology, 44, pp. 206-219.

[119] Rosar, M., and Peskin, C. S., 2001, "Fluid Flow in Collapsible Elastic Tubes: A Three-Dimensional Numerical Model," New York Journal of Mathematics, 7, pp. 281-302.

[120] Pedley, T., and Luo, X., 1998, "Modeling Flow and Oscillations in Collapsible Tubes," Theoretical and Computational Fluid Dynamics, 10, pp. 277-294.

[121] Flaherty, J., Keller, J., and Rubinow, S., 1972, "Post-Buckling Behavior of Elastic Tubes and Rings with Opposite Sides in Contact," SIAM Journal on Applied Mathematics, 23, pp. 446-455.

[122] Heil, M., 1997, "Stokes Flow in Collapsible Tubes: Computation and Experiment," Journal of Fluid Mechanics, 353, pp. 285-312.

[123] Païdoussis, M. P., and Denise, J.-P., 1972, "Flutter of Thin Cylindrical Shells Conveying Fluid," Journal of Sound and Vibration, 20, pp. 9-26.

[124] Heil, M., 1996, "The Stability of Cylindrical Shells Conveying Viscous Flow," Journal of Fluids and Structures, 10, pp. 173-196.

[125] Tang, D., Yang, C., Walker, H., Kobayashi, S., and Ku, D. N., 2002, "Simulating Cyclic Artery Compression Using a 3D Unsteady Model with Fluid-Structure Interactions," Computers and Structures, 80, pp. 1651-1665.

[126] Simon, B., Kaufmann, M., McAfee, M., and Baldwin, A., 1993, "Finite Element Models for Arterial Wall Mechanics," ASME Journal of Biomechanical Engineering, 115, pp. 489-496.

[127] Aoki, T., and Ku, D. N., 1993, "Collapse of Diseased Arteries with Eccentric Cross Section," Journal of Biomechanics, 26, pp. 133-142.

[128] Binns, R., and Ku, D. N., 1989, "Effect of Stenosis on Wall Motion: A Possible Mechanism of Stroke and Transient Ischemic Attack," Arteriosclerosis, 9, pp. 842-847.

[129] Biz, S., 1993, "Flow in Collapsible Stenoses: An Experimental Study," M.S. Thesis, Georgia Institute of Technology.

[130] Judd, R., and Mates, M., 1989, "Flow through a Stenosis in a Compliant Tube," Proceedings of the 2nd International Symposium on Biofluid Mechanics and Biorheology, pp. 417-423.

[131] Kobayashi, S., Tang, D., and Ku, D. N., 1998, "Pulsatile Flow through a Stenotic Collapsible Tube," Proceedings of the 76th JSME Fall Annual Meeting, pp. 265-266.

[132] Ku, D. N., Kobayashi, S., Wootton, D., and Tang, D., 1997, "Compression from Dynamic Pressure Conditions in Models of Arterial Disease," Annals of Biomedical Engineering, 25, pp. S-22.

[133] Stergiopulos, N., Moore, J. J., Strassle, A., Ku, D. N., and Meister, J., 1993, "Steady Flow Test and Demonstration of Collapse on Models of Compliant Axisymmetric Stenoses," Advances in Bioengineering, ASME BED, 26, pp. 455-458.

[134] Tang, D., Yang, C., Kobayashi, S., and Ku, D. N., 2001, "Experiment-Based Numerical Simulation of Unsteady Viscous Flow in Stenotic Collapsible Tubes," Applied Numerical Mathematics, 36, pp. 299-320.

[135] Conrad, W., 1969, "Pressure-Flow Relationships in Collapsible Tubes," IEEE Transactions on Biomedical Engineering, 16, pp. 284-295.

[136] Pedley, T., 1992, "Longitudinal Tension Variation in Collapsible Channels: A New Mechanism for the Break Down of Steady Flow," ASME Journal of Biomechanical Engineering, 114, pp. 60-67.

[137] Tang, D., 1995, "Numerical Solutions of Viscous Flow in Elastic Tubes with Stenoses of Various Stiffness," 1995 Proceedings of the ASME Bioengineering Conference, pp. 521-522.

[138] Tang, D., Anderson, D., Biz, S., and Ku, D. N., 1998, "Steady Viscous Flow in Constricted Elastic Tubes Subjected to a Uniform External Pressure," International Journal for Numerical Methods in Engineering, 41, pp. 1391-1415.

[139] Tang, D., Yang, C., and Ku, D. N., 1999, "A 3-D Thin-Wall Model with Fluid-Structure Interactions for Blood Flow in Carotid Arteries with Symmetric and Asymmetric Stenoses," Computers and Structures, 72, pp. 357-377.

[140] Yamaguchi, T., Furuta, N., Nakayama, T., and Kobayashi, T., 1995, "Computations of the Fluid and Wall Mechanical Interactions in Arterial Diseases," Advances in Bioengineering, ASME BED, 31, pp. 197-198.

[141] Yamaguchi, T., Nakayama, T., and Kobayashi, T., 1996, "Computations of the Wall Mechanical Response under Unsteady Flows in Arterial Diseases," Advances in Bioengineering, ASME BED, 33, pp. 369-370.

[142] Liu, B., and Tang, D., 2000, "A Numerical Simulation of Viscous Flows in Collapsible Tubes with Stenoses," Applied Numerical Mathematics, 32, pp. 87-101.

[143] Tang, D., Yang, C., Huang, Y., and Ku, D. N., 1999, "Wall Stress and Strain Analysis using a Three-Dimensional Thick-Wall Model with Fluid-Structure Interactions for Blood Flow in Carotid Arteries with Stenoses," Computers and Structures, 72, pp. 341-356.

[144] Downing, J., and Ku, D. N., 1997, "Effects of Frictional Losses and Pulsatile Flow on the Collapse of Stenotic Arteries," ASME Journal of Biomechanical Engineering, 119, pp. 317-324.

[145] Powell, B., 1991, "Experimental Measurements of Flow through Stenotic Collapsible Tubes," Master's Thesis, Georgia Institute of Technology.

[146] Kobayashi, S., Kulbaski, M., Tang, D., and Ku, D. N., 1997, "Hemodynamics and Wall Compression in High Grade Arterial Stenosis," International Journal of Cardiovascular Medicine and Science, 1, p. 32.

[147] Ku, D. N., Kobayashi, S., and Mijovic, B., 1997, "Compression from Pressure Conditions in Models of Arterial Disease," Annals of Biomedical Engineering, 25, p. 127.

[148] Hirt, C., Amsden, A., and Cook, H., 1974, "An Arbitrary Lagrangian Eulerian Computing Method for all Flow Speed," Journal of Computational Physics, 14, pp. 227-253.

[149] Hughes, T., Liu, W., and Zimmerman, T., 1981, "Lagrangian Eulerian Finite Element Formulation for Incompressible Viscous Flows," Computer Methods in Applied Mechanics and Engineering, 29, pp. 329-349.

[150] Belytschko, T., Liu, W. K., and Moran, B., 2000, "Arbitrary Lagrangian Eulerian Formulations," Nonlinear Finite Elements for Continua and Structures, Wiley, pp. 393-404.

[151] Benson, D., 1989, "An Efficient, Accurate, Simple ALE Method for Nonlinear Finite Element Programs," Computer Methods in Applied Mechanics and Engineering, 72, pp. 305-350.

[152] Ramaswamy, B., and Kawahara, M., 1987, "Arbitrary Lagrangian Eulerian Finite Element Method for Unsteady, Convective, Incompressible Viscous Free Surface Fluid Flow," International Journal for Numerical Methods in Fluids, 7, pp. 1053-1075.

[153] Souli, M., Ouahsine, A., and Lewin, L., 2000, "ALE Formulation for Fluid-Structure Interaction Problems," Computer Methods in Applied Mechanics and Engineering, 190, pp. 659-675.

[154] Nomura, T., and Hughes, T., 1992, "An Arbitrary Lagrangian Eulerian Finite Element Method for Interaction of Fluid and a Rigid Body," Computer Methods in Applied Mechanics and Engineering, 95, pp. 115-138.

[155] 1988, "LS-DYNA Theoretical Manual."

[156] Chorin, A., Hughes, T., McCracken, M., and Marsden, J., 1978, "Product Formulas and Numerical Algorithms," Communications on Pure and Applied Mathematics, 31, pp. 205-256.

[157] Winslow, A., 1963, "Equipotential Zoning of Two-Dimensional Meshes," UCRL-7312, Lawrence Radiation Laboratory.

[158] Winslow, A., and Barton, R., 1982, "Rescaling of Equipotential Smoothing," UCID-19486, Lawrence Livermore National Laboratory, Livermore, CA.

[159] Brackbill, J., and Saltzman, J., 1982, "Adaptive Zoning for Singular Problems in Two Dimensions," Journal of Computational Physics, 46, pp. 342-368.

[160] Bach, G. G., 2006, "Applied Mathematics, Course Notes," McGill University

[161] Goudreau, G., and Hallquist, J., 1982, "Recent Developments in Large-Scale Finite Element Lagrangian Hydrocode Technology," Computer Methods in Applied Mechanics and Engineering, 33, pp. 725-757.

[162] Belytschko, T., Liu, W. K., and Moran, B., 2000, "Solution Methods and Stability," Nonlinear Finite Elements for Continua and Structures, Wiley, pp. 309-392.

[163] Sievers, H.-H., Onnasch, D., GW, Lange, P. E., Bernhard, A., and Heintzen, P. H., 1983, "Dimensions of the Great Arteries, Semilunar Valve Roots, and Right Ventricular Outflow Tract during Growth: Normative Angiocardiographic Data," Pediatric Cardiology, 4, pp. 189-196.

[164] Fung, Y., 2001, "Perspectives of Biomechanics," Introduction to Bioengineering, Y. Fung, ed., World Scientific Publishing, pp. 21-34.

[165] Begum R, and Zamir, M., 1990, "Flow in Tubes of Non-Circular Cross Sections," Ocean Waves Mechanics, Computational Fluid Dynamics and Mathematical Modeling, M. Rahman, ed., Computational Mechanics Publications, Southampton.

[166] Quadir, R., and Zamir, M., 1997, "Entry Length and Flow Development in Tubes of Rectangular and Elliptic Cross Sections," Laminar and Turbulent Boundary Layers, M. Rahman, ed., Computational Mechanics Publications, Southampton.

[167] Haslam, M., and Zamir, M., 1998, "Pulsatile Flow in Tubes of Elliptic Cross Sections," Annals of Biomechanics, 26, pp. 1-8.

[168] Kobayashi, S., Tsunoda, D., Fukuzawa, Y., Morikawa, H., Tang, D., and Ku, D. N., 2003, "Flow and Compression in Arterial Models of Stenosis with Lipid Core," Proceedings of the 2003 Summer Bioengineering Conference, p. 497.

[169] Cheng, G., Loree, H., Kamm, R., Fishbein, M., and Lee, R., 1993, "Distribution of Circumferential Stress in Ruptured and Stable Atherosclerotic Lesions. A Structural Analysis with Histopathological Correlation," Circulation, 87, pp. 1179-1187.

[170] Williamson, S., Lam, Y., Younis, H., Huang, H., Patel, S., Kaazempur-Mofrad, M., and Kamm, R., 2003, "On the Sensitivity of Wall Stresses in Diseased Arteries to Variable Material Properties," ASME Journal of Biomechanical Engineering, 125, pp. 147-155.

[171] Fung, Y., Fronek, K., and Patitucci, P., 1979, "Pseudoelasticity of Arteries and the Choice of its Mathematical Expression," American Journal of Physiology, 237, pp. H620-H631.

[172] Greenberg, S. B., and Eshaghpour, E., 2001, "The Importance of the Maximum Pulmonary Artery Regurgitant Velocity Following Repair of Tetralogy of Fallot: A Pilot Study," The International Journal of Cardiovascular Imaging, 17, pp. 221-226.

[173] Cook, R. D., Malkus, D. S., Plesha, M. E., and Witt, R. J., 2002, Concepts and Applications of Finite Element Analysis, Fourth Edition, John Wiley & Sons, Inc.

[174] Meyers, M., 1994, Dynamic Behavior of Materials, John Wiley & Sons, Inc.

[175] Heil, M., and Pedley, T., 1996, "Large Post-Buckling Deformations of Cylindrical Shells Conveying Viscous Flow," Journal of Fluids and Structures, 10, pp. 565-599.

[176] Cancelli, C., and Pedley, T., 1985, "A Separated-Flow Model for Collapsible-Tube Oscillations," Journal of Fluid Mechanics, 157, pp. 375-404.

[177] Hazel, A. L., and Heil, M., 2003, "Steady Finite-Reynolds-Number Flows in Three-Dimensional Collapsible Tubes," Journal of Fluid Mechanics, 486, pp. 79-103.

[178] Berger, S., and Jou, L., 2000, "Flows in Stenotic Vessels," Annual Review of Fluid Mechanics, 32, pp. 347-382.

[179] Matsuzaki, Y., Ikeda, T., Matsumoto, T., and Kitagawa, T., 1998, "Experiments on Steady and Oscillatory Flows at Moderate Reynolds Numbers in a Quasi-Two-Dimensional Channel with a Throat," ASME Journal of Biomechanical Engineering, 120, pp. 594-601.

[180] Pedley, T., and Stephanoff, K., 1985, "Flow Along a Channel with a Time-Dependent Indentation in One Wall: The Generation of Vorticity Waves," Journal of Fluid Mechanics, 160, pp. 337-367.